EUROPEAN COMMISSION

Community Research

MATISSE

Materials' Innovations for Safe and Sustainable nuclear in Europe

Support to the development of joint research actions between national programmes on advanced nuclear materials

FP7-Fission-2013
Combination of Collaborative project (CP) and Coordination and Support Actions (CSA)

Grant agreement no: 604862
Start date: 01/11/2013 Duration: 48 Months

D.2.31

Microstructural and mechanical characterisation of selected ion and neutron irradiated alloys

MatISSE – Contract Number: 604862

Document title	Microstructural and mechanical characterisation of selected ion and neutron irradiated alloys
Author(s)	C. Pareige (CNRS), C. Heintze (HZDR), M. Hernandez-Mayoral (CIEMAT), F. Bergner (HZDR), B. Gomez-Ferrer (CNRS), E. Onobre (CIEMAT), M. Konstantinovic (SCK-•CEN), E. Meslin (CEA), O. Tissot (CEA), B. Décamps(CNRS), P. Desgardin (CNRS), R. Coppola (ENEA), L. Malerba (SCK•CEN)
Number of pages	80
Document type	Deliverable
Work Package	2
Document number	2.31
Issued by	CNRS
Date of completion	17/11/2017
Dissemination level	Confidential, only for consortium members (including the Commission Services)

Summary

High purity Fe-Cr alloys with 14wt% and 18wt%Cr and 16 alloys with different Cr, Ni, Si and P contents were selected for investigation after neutron, ion and electron irradiation. This deliverable presents the PIE results obtained by standard mechanical characterisation and with advanced characterisation techniques (SANS, TEM, APT, PAS and NI).

Neutron irradiation was performed at 300°C and at 450°C at 0.11dpa. α' particles were found in the Fe14CrNiSiP together with a second family of nano-features which are probably NiSiP enriched clusters or NiSiP decorated loops. α' particles constitute the dominant component. The nature of the nano-features found in the Fe5CrNiSiP is different from α'. The volume fraction of irradiation-induced clusters in Fe-14Cr-NiSiP is one order of magnitude higher than in Fe-5Cr-NiSiP. Vacancy clusters were only observed at 300°C and their size remains very small (<V4). TEM investigation and tensile tests revealed that Ni, Si and P impurities strongly influence the response of the alloys to irradiation. Impurities were shown to decrease the dislocation loop size and increase their number density. Accordingly, a very significant hardening is observed for the alloys which contain impurities.

Thanks to the results obtained under ion irradiation, it was possible to investigate the effect of: temperature, Cr content, impurities, irradiation dose and injected interstitials.

As under neutron irradiation, impurities were shown to play an important role. The higher the impurity content:

- the higher the concentration of vacancy defects
- the lower the size of the dislocation loops (DL)
- the higher the proportion of <111> DL (for the highest content, the majority of loops is <111> whereas it is the inverse for pure Fe, Fe9Cr and Fe9Cr MIRE)
- the highest the number density (3 times higher for 0.34wt% than for 0.17wt%) of SRCs and the lower their size.
- the richer SRCs are in impurity and Cr
- the harder the material, whatever the irradiation temperature.

It has been shown that P has the strongest effect.

The study of the influence of injected interstitials on α' precipitation showed that injected Fe strongly reduce α' precipitation because of the enhancement of recombination between vacancies and interstitials and the creation of a high density of point defect sinks (interstitial clusters, dislocation loops).

Approval

Rev.	Date	First author	WP leader	Project Coordinator
0	10/2017	C. Pareige (CNRS) 20/10/2017	L. Malerba (SCK-CEN) 25/10/2017	P.F. Giroux (CEA) 17/11/2017

Distribution list

Name	Organisation	Comments
All beneficiaries	MatISSE	

Table of contents

1 Introduction

The main objective of the MEFISTO domain is to build knowledge on the effect of the composition on the type of solute clusters that form under irradiation in high-Cr F/M alloys, their kinetics of formation, and their effect on radiation-hardening (generally correlated with embrittlement), as a basis for mechanistic embrittlement correlations, similar to those developed for reactor pressure vessel steels used in LWRs. The work proposed is the logical extension and continuation of the work performed in GETMAT [1–3], where the focus was on FeCr alloys of low purity and, particularly, on the formation of Cr-decorated loops as hardening features and on phase transformation kinetics of the alloys under irradiation. Atom Probe Tomography (APT) investigations of the irradiated alloys revealed the presence of other possible hardening features: solute clusters enriched in Cr and in the impurity elements Si, P and Ni.

In order to understand the role of each impurity on the formation of the nano-features formed under irradiation and the eventual synergies between the different species, FeCr(SiNiP) alloys of different composition will be investigated in the framework of the MEFISTO task.

More specifically, the experimental work of the MEFISTO task addressed the two following issues:

- Design and performance of modelling oriented experiments on model alloys (from high purity up to industrial purity) and, possibly, steels, in order to obtain detailed information on the solute clusters and their effect on radiation-induced hardening, thereby allowing the improvement and validation of the models, as well as setting the basis for the derivation of mechanistic embrittlement correlations.
- Investigate the influence of initial microstructure (ferritic vs ferritic/martensitic) on the response of the alloys.

High purity Fe-Cr alloys with 14wt% and 18wt%Cr and 16 alloys with different Cr, Ni, Si and P contents were selected for investigation after neutron, ion and electron irradiation. This deliverable presents the PIE results obtained with advanced characterisation techniques (Positron Annihilation Spectroscopy (PAS), Transmission Electron Microscopy (TEM), Small Angle Neutron Spectroscopy (SANS), Atom Probe Tomography (APT), Nano-Indentation (NI) and standard mechanical characterisation.

2 Experimental Methodology

2.1 Materials and irradiated conditions

2.1.1 Fe-Cr(C) alloys

Fe-Cr(C) alloys with 14w.% and 18w.%Cr were provided by CEA. They were prepared by induction melting at Ecole des Mines de Saint Etienne under the European Fusion Development Agreement contract EFDA-06-1901 [4]. Their nominal composition is given in Table 1. The alloys were received by CEA in recrystallized state, after a cold work reduction of 70%. They were then heat treated at different temperatures (for 1 hour, under pure argon flow), followed by air-cooling. Fe14Cr and Fe18Cr were heat treated at 1073K and 1123K respectively, to reach high grain sizes (~100 µm) and low dislocation density (≈ 10^8 cm^{-2}).

Table 1: composition of the Fe-Cr(C) alloys (in wt.%)

Fe-Cr alloys	Short name	Cr	C (*Wppm)*	S (*wppm)*	O (*wppm)*	N (w*ppm)*	P (*wppm)*
Fe-14%Cr	Fe14Cr_HR	14.25	5	7	4	5	<10
Fe-18%Cr	Fe-18Cr_HR	17.97	<10	<10	<10	<10	-

2.1.2 Fe-Cr(NiSiP) alloys

2.1.2.1 List of materials and basic characterisation

16 alloys with different Cr, Ni, Si and P contents were selected for investigation in MEFISTO. The 16 compositions were cast by OCAS in an induction vacuum furnace. The pure Fe source which was used contained only 50ppm Co and 70ppm Ni, while all other elements were below 10ppm. No contamination was expected by adding Cr (electrolytically refined). The composition determined by means of SS-OES (all elements except Ni, Si & Al) and ICP-OES (only Ni, Si & Al) are reported in Table 2. All other elements were below the SS-OES detection limits, except for the S content which lies between 10 and 15ppm for all casts.

Table 2: Composition of the selected FeCr(NiSiP) materials (in w.%) determined by SS-OES (all elements except Ni, Si & Al) and ICP-OES (only Ni, Si & Al). *GETMAT material with a martensitic structure.

ID	Short name	Cr	Ni	Si	P	Al
		w.%	w.%	w.%	w.%	w.%
G379	Fe*	0.002	0.007	0.001	0.003	0.023
G380	Fe-5Cr	4.9	0.008	0.002	0.003	0.027
G381	Fe-5Cr-Ni	4.9	0.107	0.002	0.003	0.023
G382	Fe-5Cr-Si	4.8	0.008	0.186	0.003	0.025
G383	Fe-5Cr-P	4.7	0.010	0.002	0.031	0.024
G384	Fe-5Cr-NiSiP	4.9	0.097	0.219	0.033	0.026
G385	Fe-9Cr	9.1	0.009	0.004	0.003	0.027
G386	Fe-9Cr-Ni	9.1	0.114	0.002	0.003	0.024
G387	Fe-9Cr-Si	9.1	0.007	0.219	0.003	0.027
G388	Fe-9Cr-P	9.1	0.007	0.009	0.033	0.027
G389	Fe-9Cr-NiSiP	9.1	0.092	0.212	0.032	0.028
G390	Fe-14Cr	14.5	0.009	0.008	0.003	0.030
G391	Fe-14Cr-Ni	14.4	0.094	0.004	0.003	0.030
G392	Fe-14Cr-Si	14.5	0.007	0.203	0.003	0.023
G393	Fe-14Cr-P	14.4	0.008	0.003	0.032	0.024
G394	Fe-14Cr-NiSiP	14.4	0.087	0.194	0.031	0.025
L252	Fe-9Cr MIRE*	9.1	0.07	0.09	0.012	0.007
L253	Fe-12Cr MIRE*	11.6	0.09	0.11	0.05	0.003

From each lab cast, a piece of 50 mm x 125 mm x 250 mm was cut from the bottom. The pieces were introduced in a pre-heated furnace at 1200°C for 1h30. Afterwards, they were taken out of the furnace and hot rolled about 1 min after leaving the furnace. Hot rolling was performed without interruption to a thickness of 10 mm (in 7 passes of following reductions: 15%, 20%, 22%, 22%, 22%, 22%, 20%). The rolling lasted approximately 1 min. After rolling the temperature was approximately 930°C. The sheets were subsequently air-cooled down to room temperature obtaining a fully ferritic microstruture. The final dimensions of the sheets were approximately 10 mm (height) x 250 mm (width) x 600 mm (length). The length of the sheets is in the rolling direction. The obtained flatness of all sheets was excellent, except for sheet G380 which had an acceptable curvature of < 5 mm over the strip length.

2.1.3 Irradiation conditions

2.1.3.1 Neutron irradiations

MatISSE samples were irradiated in BR2 during cycles 4 and 6 of 2016 at 290°C ± 5°C and 450°C ± 20°C. The irradiation duration was 41.8 days in total. The flux was about 1.5 10^{13} $n.cm^{-2}.s^{-1}$. Fluence obtained from dosimeter is about 7.0-7.5 10^{19} n/cm^2 or 0.11 ± 0.05 dpa with a dose rate of 2.210^{-8} dpa/s. More details are available in the milestone MS.2.3.1. Table 3 presents the list of the materials that were irradiated and the irradiation conditions.

Table 3: Materials and irradiation conditions for irradiation in CALLISTO loop in BR2.

290°C		~450°C	
ID	Short name	ID	Short name
G384	Fe-5Cr-NiSiP	G379	Fe
G385	Fe-9Cr	G384	Fe-5Cr-NiSiP
G389	Fe-9Cr-NiSiP	G385	Fe-9Cr
G394	Fe-14Cr-NiSiP	G389	Fe-9Cr-NiSiP
L252	Fe-9Cr (Mart.)	G394	Fe-14Cr-NiSiP
E97	Eurofer97	L252	Fe-9Cr (Mart.)
		E97	Eurofer97
		T91	(steel)

2.1.3.2 Ion irradiations

a) Ion irradiation of Fe-Cr(C) alloys

High purity Fe-Cr alloys were irradiated with 2 MeV Fe^{2+} ions at 300°C using the JANNuS-Saclay facility [5,6]. The ion flux was 6×10^{10} ions/(cm^2·s). The damage and implantation profiles, given in Figure 1 were calculated with SRIM (Stopping and Range of Ions in Matter) [7,8] using the ‘‘Quick’’ Kinchin and Pease option as recommended by Stoller et al. [9] and a displacement threshold of 40 eV [1]. The dose rate varied from $3x10^{-5}$ dpa/s near the surface up to $6.8x10^{-5}$ dpa/s at the damage peak.

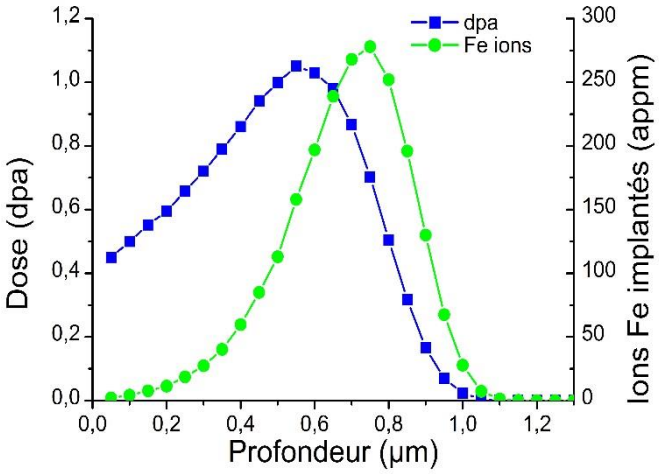

Figure 1: Damage and implantation profile calculated with SRIM 2013 [7,8].

b) Ion irradiation of Fe-Cr (NiSiP) alloys

Ion irradiations were performed at the ion beam center of HZDR. Samples were irradiated with 5 MeV Fe^+ ions up to 0.1 dpa or 0.5 dpa measured at 500 nm from the surface. A description of the irradiation sets is given Table 4. Two sets of irradiation experiments were performed for each condition. Samples of pure Fe were added to group 1 and 2 for the second set of ion irradiations.

Table 4: Irradiation conditions.

Irradiation temperature	Run 2	Run 3	Run 1
	0.1 dpa		0.5 dpa
200ºC			Group 1
300ºC	Group 2	Group 3	Group 1 + in-situ TEM
450ºC			Group 1

Group 1: Fe9CrNiSiP, Fe9Cr, Fe9Cr GETMAT, Fe5CrNiSiP, Fe14CrNiSiP
Group 2: Fe9Cr, Fe9CrNi; Fe9CrP, Fe9CrSi; Fe9CrNiSiP
Group 3: Fe14Cr, Fe14CrNi; Fe14CrP, Fe14CrSi; Fe14CrNiSiP

Figure 2 and Figure 3 provide the damage and injected Fe concentration profiles for the two target doses 0.1 and 0.5 dpa at 500 nm respectively. The dose rate at 500 nm was about 5.10^{-5} dpa/s (fluence of about $1.3\ 10^{11}$ $cm^{-2}.s^{-1}$). More details about irradiation conditions are available in millestone MS 2.3.3

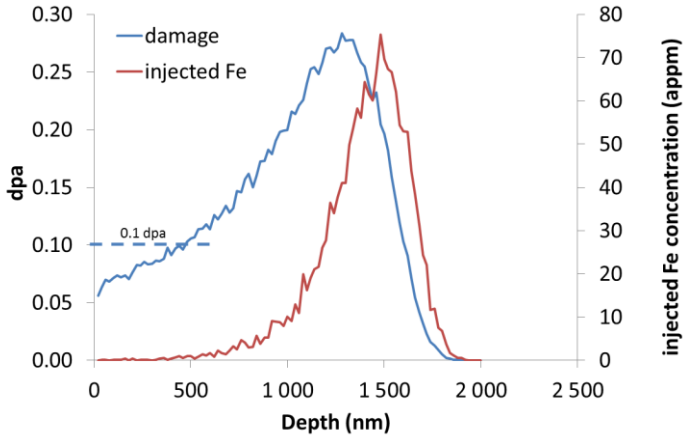

Figure 2: Damage and injected Fe concentration profiles for the target 0.1 dpa at 500 nm.

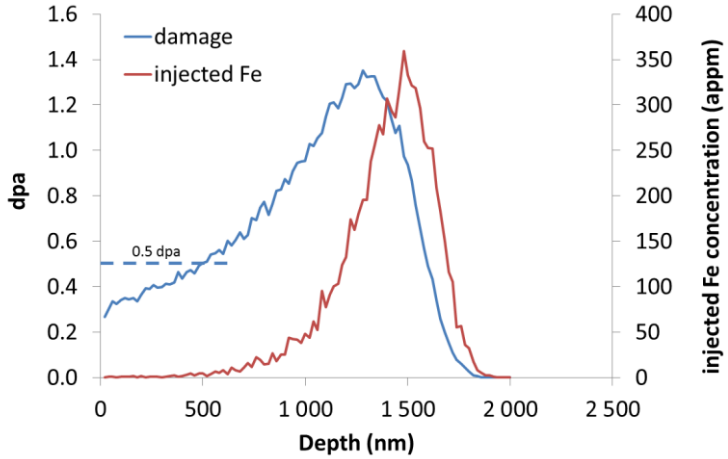

Figure 3: Damage and injected Fe concentration profiles for the target 0.5 dpa at 500 nm.

2.1.3.3 Electron irradiations

Irradiations were performed using the 1 MeV High Voltage Electron Microscope (HVEM) of JANNuS-Saclay platform on needle-shaped and thin foil specimens that were then used for the APT and TEM studies respectively. The electron flux was 3.55 x 10^{18} electrons/cm^2/s and the calculated doses, using a displacement threshold energy of 40 eV [10,11], were 0.012, 0.023, 0.2 and 0.7 dpa (damage rate 3.9 x 10^{-5} dpa/s). All samples were irradiated at a temperature of 300°C, measured with a thermocouple placed in contact with the sample.

The APT samples were irradiated using a sample holder that was specifically designed for HVEM irradiation of needle-shaped APT samples. To limit surface effects (such as point defects migration and elimination at free surfaces) occurring when the area of interest is too close to the tip surface, needles with large tip radius (1-2 µm) were irradiated. The tips were placed perpendicular to the electron beam and a 6 – 8 µm zone of the samples was irradiated. Based on finite element calculations, beam heating was evaluated to be limited to 29 K for our experimental conditions. After irradiation, the samples were annular milled using a 1530XB Zeiss Focused Ion Beam (FIB) in order to obtain needles suitable for APT analysis (tip radius ≈50 nm).

The TEM thin foils were irradiated to doses of 0.023 and 0.2 dpa. An 8 µm diameter-sized area of the thin foil was irradiated within the HVEM using the same conditions as for the atom probe samples. The temperature was controlled by an integrated sample holder thermocouple and kept at 573 K during these experiments.

2.2 Microstructural characterisation techniques

2.2.1 Relaxation techniques: internal friction (IF) and magnetic after effect (MAE)

IF and MAE are two relaxation techniques that provide information on, especially, interstitial chemical species dispersed in the specimen matrix. IF is based on the interaction between an applied mechanical stress field and anisotropic lattice distortions caused by interstitial or substitutional atoms and other defects. The energy dissipation, caused by the stress-induced movement of the defects, leads to the IF effect. MAE is based on the interaction between the magnetic domain walls and the lattice defects. It is important to mention that if mechanical and magnetic relaxation processes are caused by the same type of lattice defects, the measurements in both types of experiments should provide similar data. Both techniques are established at SCK•CEN for the measurements of both non-active and active materials.

In comparison with other microstructural characterization techniques, IF and MAE have the great advantage to be sensitive not only to the mere presence of lattice defects, but to their movement as well. Both methods represent efficient tools to study various types of interstitials (carbon, nitrogen, and hydrogen) and dislocation-related relaxation processes allowing the determination of corresponding parameters of defect motion, such as defect activation energies and concentrations.

2.2.2 Positron Annihilation Spectroscopy (PAS)

PAS is a valuable method to obtain information on vacancies and vacancy clusters formation under irradiation and their thermal stability. Two measurement techniques based on positron annihilation can be used. These are Doppler broadening (DB) spectroscopy and positron lifetime spectroscopy (PALS). While the PALS measurements give information on the electronic density of the material at the place of positron annihilation, the DB spectroscopy allows the measurements of the momentum distribution of the electron-positron annihilation pair thus giving information on the chemical environment of the positron annihilation site. PAS is particularly sensitive to open volume defects, such as vacancies, vacancy clusters and dislocations. The sensitivity range for the vacancy detection in metals starts at about one vacancy per 10^7 atoms. It is the only experimental technique that provides information about vacancy clusters evolution under irradiation. Additionally, carbon strongly binds with a vacancy, so PAS usually complements the relaxation measurements with respect of carbon distribution analysis.

Doppler broadening spectra are characterized by an S parameter (line-shape parameter) and a W parameter (wing parameter). S and W parameters are defined as the ratio of low momentum and high momentum regions of the DB spectrum to total momentum respectively (c – speed of light, pL- longitudinal component of the

positron-electron momentum along the direction of γ-ray emission). S and W carry different information. Annihilation with the valence electrons lead to a small difference in the energy of γ-rays, while the inner shell electrons can lead to energy changes of any magnitude. The former contributes to the low-momentum region and is observed by the S parameter, which therefore carries information about open volume defects. The latter, on the other hand, contributes to the high-momentum region represented by W parameter.

PAS experiments were performed at SCK•CEN and HZDR on neutron irradiated samples. Unirradiated and ion irradiated samples were investigated at HZDR and CNRS/CEHMTI.

PAS measurements on neutron irradiated samples:

Doppler broadening measurements

In order to minimize the background in case of active materials, CDB (Coincident Doppler Broadening) spectra were measured using two Ge detectors located at an angle of 180° relative to each other that allows both annihilation photons to be detected coincidentally. To prevent pileup, due to the activity of the specimens, the detectors could be moved further from specimen (up to 1.5m). The analysis of the results is based on channel selection through the coincidence region of the two-dimensional (2-D) spectra. The resulting 1-D spectrum was normalized to pure, non-irradiated, defect free iron. S and W parameters were extracted from each spectrum. The momentum ranges were defined as $|p_L| < 2.5x10^{-3}m_0c$ for S and $15x10^{-3}\ m_0c < |p_L| < 25x10^{-3}\ m_0c$ for W (c – speed of light, pL- longitudinal component of the positron-electron momentum along the direction of γ-ray emission).

PALS

Positron annihilation lifetime spectroscopy (PALS) measurements were performed at the GiPS (Gamma induced positron spectroscopy) beamline of the HZDR linac ELBE. The GiPS facility is the only suitable setup worldwide to measure sample material with an information depth > 50 µm. For this reason, this setup is a unique opportunity to measure extended volume samples and reduce the influence of surface effects expected in the materials under investigation. Due to positron production directly inside the sample there is no contribution from the positron source like in common setups. In the context of the complex chemical composition of the materials investigated this simplifies the analysis considerably, because the lifetime spectra just contain contributions from the sample. Furthermore, GiPS enables the acquisition of lifetime spectra independently of the gamma-start signal, which, in the case of neutron irradiated Fe-based alloys, significantly decreases the background noise originating from the ^{60}Co decay in the material.

Samples of 1 mm thickness and 6 or 9 mm diameter were wrapped in Hostaphan foil to exclude contaminations of the environment and fixed on thin threads to reduce background signals. characteristic annihilation quanta were registered in coincidence by 4 sets of pairs of high-purity Germanium semiconductors for accurate energy determination and BaF_2 scintillation detectors for accurate timing [12]. The measured lifetime (LT) distributions were analyzed by means of the PALSfit [13] software package.

PAS measurements on ion irradiated samples:

Doppler broadening measurements

Depth-resolved Doppler Broadening Positron Annihilation Spectroscopy and in selected cases Coincidence Doppler Broadening (at 16 keV) were performed using the slow positron beam SPONSOR [16] at HZDR. In SPONSOR positrons emitted from a ^{22}Na source are moderated and accelerated to the sample with defined energies between 27 eV and 35 keV to reach depths of up to about 3 µm. Therefore, the method is specifically useful to investigate open-volume defects in ion-irradiated samples where the defects are distributed in a near surface region on the order of 1 µm.

Slow-positron DB was applied to selected ion-irradiated samples and the respective unirradiated reference samples. The samples where mechanically mirror-polished followed by electro-polishing in a solution of 2% perchloric acid in 98% ethylene glycol monobutyl to remove the surface damage introduced by mechanical polishing. Data analysis was performed using pure annealed Fe as reference for calculation of the S and W parameter. The energy ranges for S and W parameter calculation were set to $|E_\gamma\text{-}511\ keV| < 0.97$ keV and $2.2\ keV < |E_\gamma\text{-}511\ keV| < 3.2$ keV, respectively, for all samples.

The CEMHTI slow positron accelerator was also used to perform Doppler broadening Spectroscopy measurements [14]. Vacancy type defects induced by irradiation were characterised in all Fe-9Cr samples containing different Ni, Si and P contents. The positron-annihilation characteristic that was investigated is the positron-electron pair momentum distribution. It was measured at 300 K by recording the Doppler broadening of the 511-keV annihilation line with a Ge detector [FWHM ≈ 1.24 keV at 514 keV]. Approximately 8×10^5 events were collected in the peak at each positron energy value. The window 511[-6.35;+6.35] keV was used to calculate the total number of annihilation events. The broadening of the annihilation γ line, $\Delta E\gamma$, is proportional to the momentum component of the annihilating electron-positron pair, p_L , along the emission direction of the photons: $2\Delta E\gamma=cp_L$. Two parameters are used to characterize the shape of the momentum distribution. The low momentum parameter S in the window at the peak, 511[-0.636;+0.636] keV, corresponds to the fraction of annihilations taking place in the momentum range (|-2.177| to |2.177|)$\times10^{-3}m_0c$. The high-momentum parameter W in the windows at the wings, 511[-6.35;-2.46] keV and 511[+2.46; +6.35] keV, corresponds to the fraction of annihilations taking place in the momentum range (|-24.88| to |-9.64| and |9.64| to |24.88|)$\times10^{-3}m_0c$.

To investigate the depth dependence of S and W, the curves S(E) and W(E) were recorded as a function of the beam energy E increased in 0.5-keV steps from 0.5 to 25 keV. To determine whether only two distinct annihilation characteristics contribute to a set of data (S,W) in a given energy range, we use the graphical analysis where S is plotted as a function of W with the energy E as running parameter. When only two distinct annihilation characteristics (S_1 ,W_1) and (S_2 ,W_2) contribute, the S(W) plot falls on a segment of a straight line that is a fingerprint of the superposition of the two annihilation characteristics and goes from (S_1 ,W_1) to (S_2 ,W_2).

2.2.3 Small Angle Neutron Scattering (SANS)

SANS is the most important characterization technique among indirect analysis methods. Solute clusters in a size range from 0.5 to up to 100 nm and concentrations > 0.005 vol% are identified through an increase in scattering intensity. Information on the size distribution of scatterers, their number density and volume fraction is obtained with an inverse transformation of the scattering pattern. SANS is able to probe a sample volume of several tens of mm^3, while still resolving changes on a sub-nanometer scale. Based on the ratio of magnetic and nuclear scattering conclusions on the type of scattereres can be drawn.

Samples of 1 mm thickness and 6 or 9 mm diameter were investigated. The exact same samples (14Cr-NiSiP only) were used for positron annihilation lifetime spectroscopy (PALS).

The SANS experiments were conducted at the SANS-1 beamline of MLZ Garching (research reactor FRM-2) [15]. A ^{3}He-detector of 1 m^2 cross section consisting of 128 x 128 pixels was used. The sample-detector distances were 1.6 and 8 m with corresponding beam collimation lengths The scattering intensity was measured with a neutron beam of 0.45 nm wavelength. A scattering-vector range of Q = 0.1 to 3.2 nm^{-1} was measured. The samples were placed in a magnetic field of 1.5 T (Cryomagnet) in order to separate magnetic and nuclear scattering. Data calibration was done using acrylic glass (PMMA) (detector efficiency) and a reference sample with well-known differential magnetic and nuclear scattering cross section. Data reduction was carried out using the BerSANS software package [16].

The scattering cross sections of the unirradiated reference samples were subtracted from the respective cross sections of the irradiated samples in order to derive the characteristics of irradiation-induced scatterers. These difference scattering curves were transformed into size distributions of scatterers using two different methods: the indirect Fourier transform method (commercial code) [17] and the Monte Carlo method (own HZDR code) [18]. Different details of the fit procedure and data scatter can cause slight deviations between the results obtained from both methods, but generally good consistency was found. The advantages of the MC-based code are a higher degree of objectivity and the output of error bands of the reconstructed size distributions.

The A-ratio first introduced by Beaven et al. [19] was calculated from the magnetic and nuclear contributions. It is a one-parameter signature of the mean composition of irradiation-induced scatterers.

2.2.4 Atom Probe Tomography (APT)

APT is a quantitative and destructive analytical technique. It is the only material analysis technique offering extensive capabilities for both 3D imaging and chemical composition measurements at the atomic scale. The

strength of APT is its ability to detect all the atoms with an equivalent efficiency (from the lightest to the heavier) and its high spatial resolution (around 0.1-0.3 nm resolution in depth and 0.3-0.5 nm laterally). APT is sensitive to dilute and small objects which are invisible for TEM. Clusters of as few as 10 atoms of impurity species are detectable in principle. In case of concentrated species, the detection limit of particles or clusters is about 0.5 nm in radius. APT is thus well adapted to the detection and quantitative characterization of nanometric solute clusters (composition, size, number density) and segregations at dislocation loops and lines or at grain boundaries. It gives quantitative information which is not accessible using global experimental techniques. But APT cannot provide information about vacancy, vacancy clusters, cavities and voids and about dislocation lines or loops without segregation. The small size of the probed volume (typically $30 \times 30 \times 150$ nm^3) limits APT ability to detect objects with a low density and its statistical representativeness. The basic principle of APT and data treatment may be found in different books or reviews [20–24].

The APT samples were prepared using two methods : electropolishing and focussed ion beam (FIB). In case of electropolishing, samples were prepared from 0.3 x 0.3 x 15 mm sticks. They were obtained by choosing suitable electro polishing conditions (75% acetic acid -25% perchloric acid and 98% ethylen glycol monobutyl ether – 2% perchloric acid). In case of FIB preparation, the APT samples were lifted out using either a Helios 650 NanoLab FEI Focused Ion Beam or a ZEISS Crossbeam 540 at different depths in order to characterise precipitation/clustering with respect to the damage and implantation profiles. The final milling was performed with a Ga beam energy of 2kV in order to reduce implantation of Ga ions in the material.

The samples were examined using LEAP 4000X HR Atom Probes from CAMECA equipped with a Delay Line Detector (DLD) [25] having a detector efficiency of 36% (GPM/CNRS) or 42% (CEA Saclay). The LEAP HR APTs are equipped with a reflectron which provides a high mass resolution and improves the accuracy of composition measurements. The samples were cooled down to a temperature of 55K in order to mitigate the preferential field evaporation of Cr atoms. During analyses, the atom probe specimens were electrically pulsed with a pulse fraction of 20%, a pulse rate of 200 kHz. Detection rate was set up between 0.1% and 0.35%.

The reconstructions of the volumes were done with IVAS 3.6.8 (CAMECA software) using standard parameters such as a compression factor of 1.4-1.7, an evaporation field of 33 V.nm^{-1} and a *k* factor of 3.0 – 5.6 (depending on the tip support i.e. needle or micro-coupon). Compression factors used were systematically derived from the crystallographic angles between poles observed on the desorption maps. *k* factors were calculated so as to obtain the correct inter-planar distances of the crystallographic planes observed in the volume.

The analysis of the atom probe data was carried out using the 3D Data Software for Atom Probe Tomography developed by the GPM research group in Rouen, France. Measurement of the size and number density of clusters was performed using the “iso-position” concentration data filter [26,27]. This filter enables the particles to be distinguished from the surrounding matrix based on their composition. The parameters used are given in the results part. The cluster’s composition was measured in the core of the clusters using either radial or erosion concentration profiles [24]. Composition values were averaged over all the measurements.

The number density of the particles was determined by a simple ratio of the number of the observed clusters to the overall analysed volume. The radius of each precipitate was calculated considering spherical particles: $R_{ppt} = \sqrt[3]{\frac{3nV_{at}}{4\pi Q}}$, with *n* the number of atoms in each particle, V_{at} the Fe atomic volume and *Q* the detector efficiency. Fe shells were sometimes observed around particles/clusters. These shells were removed using an erosion method before measuring the radius. The volume fraction was defined as the ratio of the number of atoms inside the clusters/clusters to the total number of collected atoms.

In the cases of as-received (AR) and low dose irradiation (0.1 dpa) conditions, the identification of the clusters is not possible—or limited— using the iso-position tool. In such cases, alternative statistical tools have been used to analyse the level of randomness of the solute distributions. The Thuvander et al. test [28] has been applied to rectangular volumes of about 0.7-3.0 millions of atoms to account for the ordered, random or clustered distribution of the Cr in the samples. In this method the APT volume is subdivided in small boxes. The frequency distribution of the Cr concentration is then measured and its standard error is measured and compared with the standard deviation of the binomial distribution corresponding to and homogeneous distribution of the Cr in all the tested volume. This comparison between the standard error and the standard deviation is made for several box sizes, a characteristic curve which indicates the deviation from the random distribution as a function of the sampling size has been obtained for each specimen. Thus early stages of α/α’ decomposition can be identified.

Concerning the distribution of the impurities (NiSiP) on the AR states and at low dose, its study has been based on the calculation of the so called *V* parameter [29,30]. This parameter measures the statistical distance between the random distribution of the specified specie and its experimental distribution. In the current case, frequency distributions of the 1st near-neighbour (1NN) distances of P-P, Ni-Ni and Si-Si pairs have been measured. These frequency distributions have been obtained from the APT volume in regions far away from

the field desorption lines and poles. The V parameter is a semi-quantitative parameter which will allow to make comparisons about the impurities distribution in the different materials and irradiation conditions.

2.2.5 Transmission Electron Microscopy (TEM)

The basic principles of Transmission Electron Microscopy (TEM) are presented in [31] and the specific use of TEM applied to the characterisation of radiation damage is published in [31]. Information from TEM comes from the images of the microstructure by using different contrast methods to image the different features in the microstructrure. TEM allows the characterisation of the microstructure in a wide range of magnifications, going through different spatial scales, from the grain scale to atomic resolution. Additionnally, crystallographic information can be obtained from electron diffraction. Chemical information can also be provided by the employment of different techniques combined to a transmission electron microscope.

In the case of the characterisation of radiation damage, diffraction contrast is applied to image dislocation loops with a resolution about 1.5 nm. Other features such as voids, may also be observed by phase contrast, forming the images in out of focus mode.

In the present work, TEM investigations were performed by means of a microscope JEOL JEM-2010 operating at 200 keV, with LaB_6 filament. Bright Field (BF) and Weak Beam Dark Field (WBDF) conditions were employed to image the defects created by irradiation. From TEM images, quantitative information can be extracted such as number density and size distribution. The characterization of the features induced by irradiation in the case on BCC metals involves obtaining information about density and size distribution of the specific features. In the particular case of dislocation loops, it is desirable to know their Burgers vector as well as their interstitial or vacancy nature. The methodology usually employed is well described in the above mentioned references.

In the present work, the images were taken using different reflections, g, type (110) or (200), around zone axis ⟨111⟩, ⟨110⟩ and ⟨100⟩ when possible. Every BF image from each region has been compared to the corresponding WBDF image, making it possible to discern most of the visible loops in each orientation. Through this comparison, it is observed that smaller loops are better discerned in WBDF images. Large loops are sometimes not easy to discern completely in WBDF, but they are clearly observed in BF. Loop sizes have been measured in both types of images, paying attention to avoiding double counting so histograms show data of all the visible loops. Size data refer to the largest dimension of the image of the dislocation loops and correspond to the loop diameter. The loop size histograms were fitted to a log-normal function from which the average size was calculated. Quantitative information about the number density was obtained by counting visible loops in a defined region, considering both, BF and WBDF, again avoiding double counting. The amount of ambiguous features difficult to distinguish from very small irradiation-produced loops is considered as the error in the counting. Such features were counted as half each following previous practice reported in Refs. [31]. It has to be noted that part of the dislocation loops present in the material may not be visible under certain diffraction conditions, due to the fact that when the product $\mathbf{g}\cdot\mathbf{b} = 0$ (**g** being the diffraction vector and **b** the Burgers vector of the dislocation), the contrast of a dislocation vanishes or is very weak [2]. For instance, one half of the loops with $b=1/2a_0\langle 111\rangle$ and one third of the loops with $b=a_0\langle 100\rangle$ will be invisible in images with g type {110}. Therefore, the number of visible defects counted in one image, taken with the corresponding condition, **g**, has to be corrected taking into account the proportion of each family of loops and, then, the amount of loops not visible with that specific **g**. The “statistical $\mathbf{g}\cdot\mathbf{b}$ analysis” [31], was employed to calculate the proportion of each Burgers vector and the total number density, thus taking into account all the loops.

Neutron irradiated specimens for TEM characterisation were received in the form of 6 mm diameter discs, from where 3mm discs where punched out. Discs were mechanically thinned up to 0.1 mm. Final thinning to electron transparency was obtained by electropolishing in a 5% perchloric acid in methanol at -60ºC.

In the case of the ion-irradiated materials a modified method was employed in order to extract a TEM sample from the 1.5 µm thick ion-irradiated layer. Discs of 3 mm in diameter were punched out from the ion-irradiated plate. As a first step, a short electropolishing was applied to the sample. The amount of material removed during this step was estimated taking into account the initial thickness of every sample and the total time to perforation. In this way, possible surface damage, oxidation, etc., are removed and the region to be examined by TEM is located within the damaged area. The estimated depth, together with the estimated dose in dpa at the examined region, are presented in Table 5. After the short electropolishing, the ion-irradiated surface is protected from contact with the electrolyte and final thinning is performed by removing material from the non-irradiated backside of the sample.

Table 5: Estimated dose in dpa at the region examined by TEM

Specimen Code	Initial thickness (µm)	t_{flash} (s)	Total time until perforation (s)	Depth after material removal (nm)	Estimated dose at the specimen thickness (dpa)
G379-Fe (3)	90	3	290	931	0.940
G384-2-Fe5CrNiSiP- (1)	90	3	410	658	0.647
G385-2-Fe9Cr- (2)	100	0	668	0	0.268
G385-2-Fe9Cr- (3)	100	3	788	380	0.465
L252-4.6-Fe9Cr- (2)	100	3	768	390	0.471
G389-FeNiSiP (1)	90	3	666	405	0.471
G394-2-Fe14CrNiSiP (1)	100	3	705	425	0.484

2.3 Mechanical characterisation techniques

2.3.1 Nano-indentation (NI)

Nanoindentation is a well-recognized tool to probe the mechanical behaviour of thin layers. It is extensively used to study irradiation hardening in structural materials irradiated with ions, where mechanical testing methods usually applied to neutron irradiated (bulk) material are not applicable.

Nanoindentation testing on selected ion-irradiated samples and their respective unirradiated references was performed at HZDR utilizing a Universal Nanomechanical Tester (UNAT) equipped with a Berkovich indenter. The samples where mechanically mirror-polished followed by electro-polishing in a solution of 2% perchloric acid in 98% ethylene glycol monobutyl to remove the surface damage introduced by mechanical polishing. Calibrations of the indenter area function and the instrument stiffness were based on measurements on two reference materials (fused silica, sapphire) with known elastic modulus. The quasi continuous stiffness measurement (QCSM) method was applied, where the load is superimposed with a sinusoidal oscillation at discrete loads. This method allows the contact stiffness to be calculated along the loading curve and the full loading curve to be exploited to calculate the indentation hardness (H_{IT}) as a function of contact depth (h_c). The tests were performed with a maximum load of 50 mN with a corresponding contact depth of about 1 µm. More than 30 indents per material and condition were performed. Zero point and thermal drift correction were applied to each individual curve. Thereafter, an average curve was calculated and analysed using the method described by Oliver and Pharr [31]. The hardness value at a reference depth of 200 nm was chosen as the hardness representative for the irradiated layer and to calculate the irradiation-induced hardness change. A linear superposition of the initial hardness and the hardness contribution by the irradiation-induced defects is assumed. Moreover, it is assumed that the indentation size effect (ISE) does not significantly change with irradiation.

2.3.2 Tensile tests

The tensile tests were performed on an Instron 1341 machine, at different temperatures, with a constant crosshead speed of 0.1 mm/min, which corresponds to a strain rate of $1.4 \cdot 10^{-4}$ s^{-1}. Two types of tensile specimens were used: (a) cylindrical and (b) flat. Cylindrical specimens were 24 mm long, with a cylindrical gauge section of 2.4 mm in diameter, and 12 mm in length. Flat specimens were 15 mm long with a rectangular gauge section of 1.7 x 1.5 mm^2, and 5 mm in length. Neutron irradiated samples were tested with Instron 1341 machine placed in the hot cell. Results of non-irradiated samples are shown and discussed together with neutron irradiated samples.

2.3.3 Hardness tests

The Vickers hardness HV10 (load 98.1 N) was measured at HZDR using the Vickers hardness devices Shimadzu HSV20 (unirradiated samples only) and semi-automatic Akashi AVK-C1 in a hot cell lab (neutron-irradiated and unirradiated reference samples). The measurements were performed according to the Standard test procedure DIN EN ISO 6507-1:2006-03.

3 Characterisation of the as-received alloys

3.1 Metallography

The basic characterization of the as-received materials was performed by HZDR, CIEMAT and SCK•CEN (metallographic and TEM characterization, tensile tests and macro-hardness measurements). Results are given in

Table *6*. The density of dislocations is not especially high. Metallography images are given in Figure 4, Figure 5 and Figure 6. More details are available in milestone MS.2.3.1.

Table 6: grain size, engineering stress (yield strength σ_y and ultimate tensile strength σ_u), engineering strain (uniform elongation ε_u and final elongation ε_f) and hardness at room temperature. Data and uncertainties were obtained over 3 tensile specimens for model alloys and 6 for steels.

Alloy	Grain size (µm)	σ_y (MPa)	σ_u (MPa)	ε_u (%)	ε_f (%)	HV10
Fe	95	196 ± 22	303 ± 13	17 ± 3	33 ± 3	58 ± 2
Fe5Cr	36	205 ± 25	310 ± 8	19 ± 4	39 ± 5	77 ± 1
Fe5Cr0.1Ni	37	180 ± 5	300 ± 2	24 ± 1	46 ± 1	82 ± 2
Fe5Cr0.2Si	37	197 ± 4	323 ± 2	24 ± 1	45 ± 3	83 ± 1
Fe5Cr0.03P	36	221 ± 11	325 ± 2	19 ± 3	37 ± 5	88 ± 6
Fe5CrNiSiP	31	231 ± 5	353 ± 5	21 ± 1	40 ± 3	102 ± 2
Fe9Cr	25	252 ± 8	391 ± 2	17 ± 2	35 ± 3	110 ± 1
Fe9Cr0.1Ni	24	246 ± 7	379 ± 2	19 ± 1	40 ± 1	104 ± 1
Fe9Cr0.2Si	27	242 ± 5	378 ± 1	20 ± 1	39 ± 1	103 ± 1
Fe9Cr0.03P	26	237 ± 3	373 ± 3	20 ± 3	39 ± 3	101 ± 3
Fe9CrNiSiP	27	257 ± 4	399 ± 3	20 ± 1	38 ± 3	113 ± 3
Fe14Cr	241	230 ± 4	306 ±7	17 ± 3	31 ± 3	105 ± 6
Fe14Cr0.1Ni	240	250 ± 7	319 ± 9	18 ± 5	32 ± 7	113 ± 5
Fe14Cr0.2Si	217	248 ± 13	319 ± 13	18 ± 4	31 ± 6	112 ± 4
Fe14Cr0.03P	253	263 ± 6	343 ± 6	17 ± 6	30 ± 8	114 ± 3
Fe14CrNiSiP	239	268 ± 16	319 ± 23	10 ± 5	20 ± 4	123 ± 6
T91	14	577 ± 6	716 ± 3	7.7 ± 0.4	25 ± 1	229 ± 2
P92	31	498 ± 9	672 ± 2	10.4 ± 0.4	26 ± 2	213 ± 3
E97	6	547 ± 7	681 ± 4	6.3 ± 0.3	25 ± 1	220 ± 1

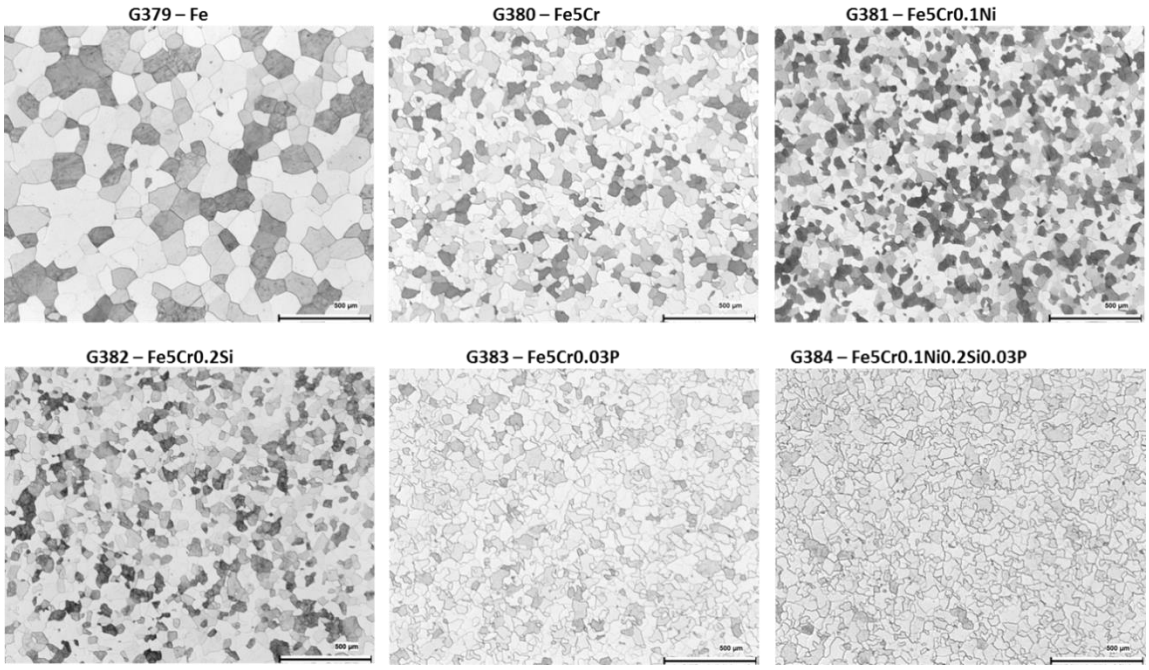

Figure 4: Metallography of the Fe5Cr(NiSiP) alloys.

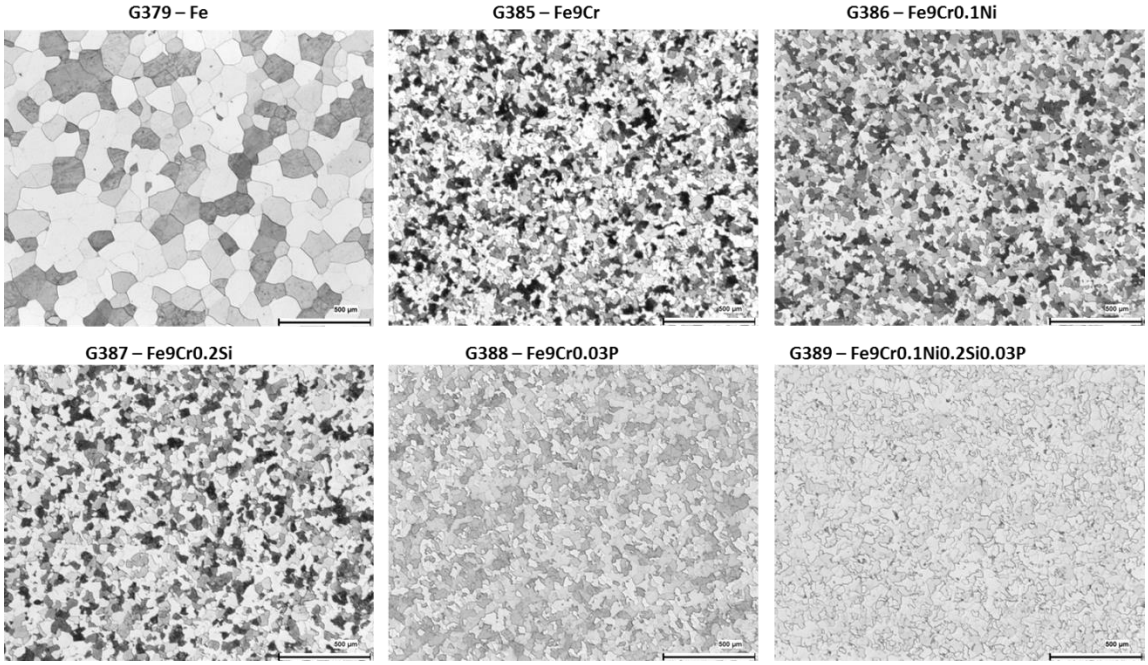

Figure 5: Metallography of the Fe9Cr(NiSiP) alloys

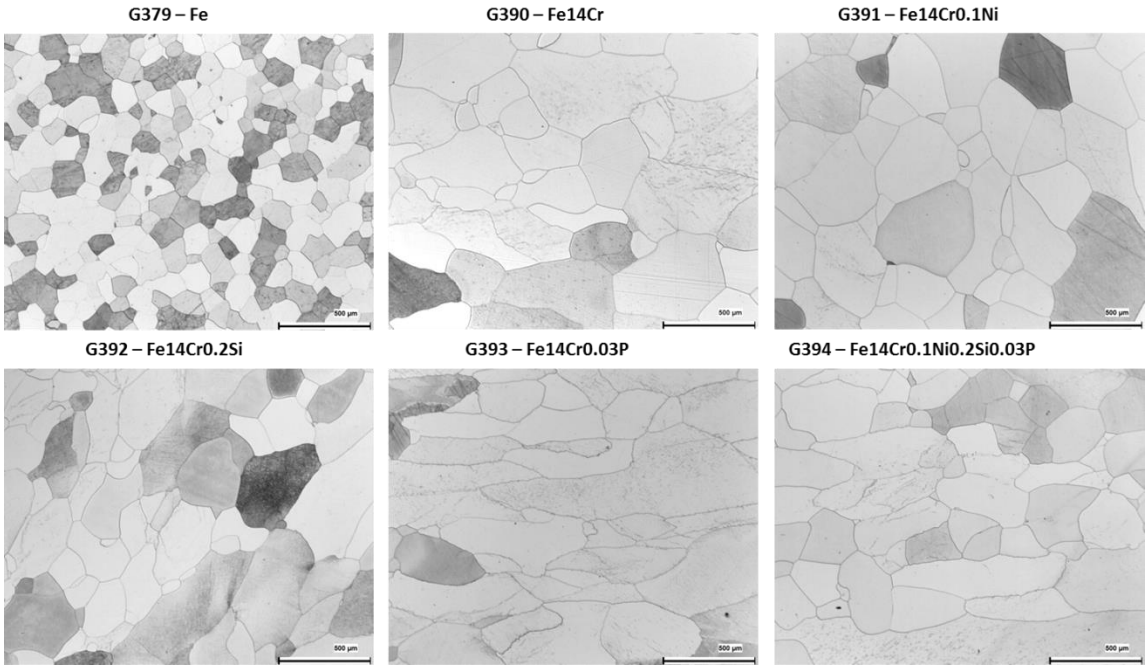

Figure 6: Metallography of the Fe14Cr(NiSiP) alloys

3.2 SEM/EBSD

EBSD maps have been obtained from some materials, images are shown in Figure 7. The analysis of these maps allows to confirm that materials present no texture, showing a random orientation distribution of grain orientation. In order to determine the grains, a critical misorientation angle of 10º has been defined. Grain size distribution and average size have been obtained, being in agreement with those obtained from metallography.

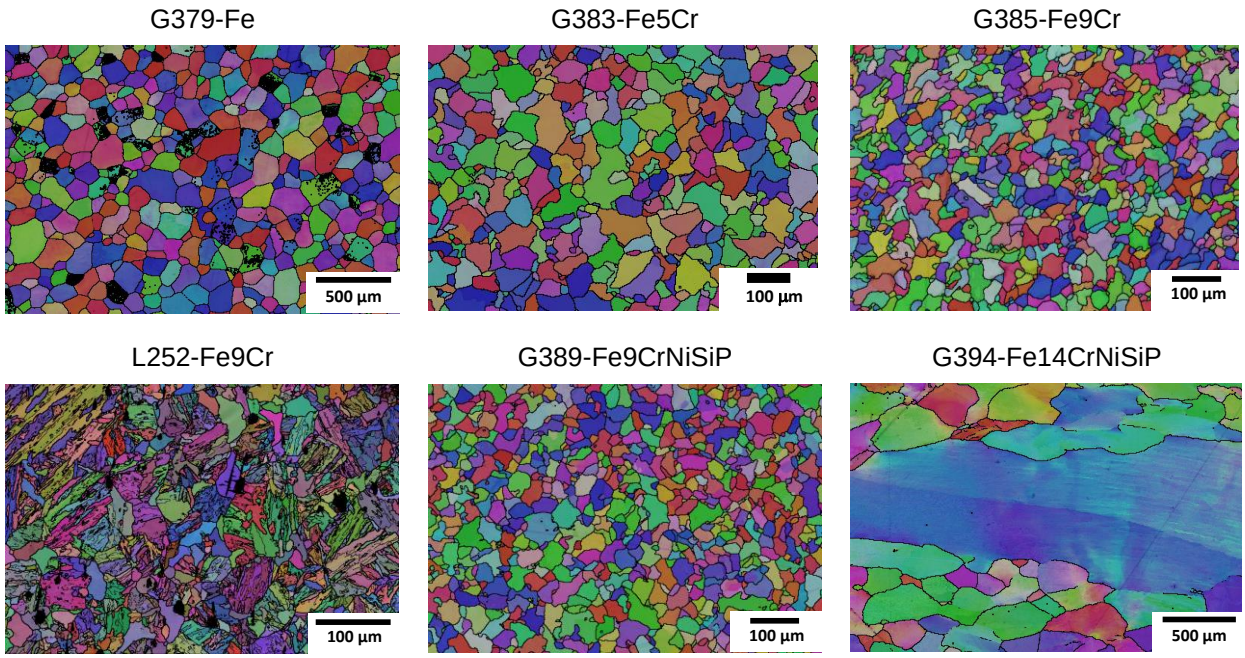

Figure 7: EBSD maps from some FeCr alloys (note differences in magnification)

3.3 TEM

Figures below show some examples of TEM images of materials under study, in as-received condition. From this type of images, information about initial microstructure before ion or neutron irradiation can be obtained.Figure 8 shows examples of typical regions found in four non irradiated materials. Dislocation density has been measured in these and similar images. Results are summarised in Table 7 below.

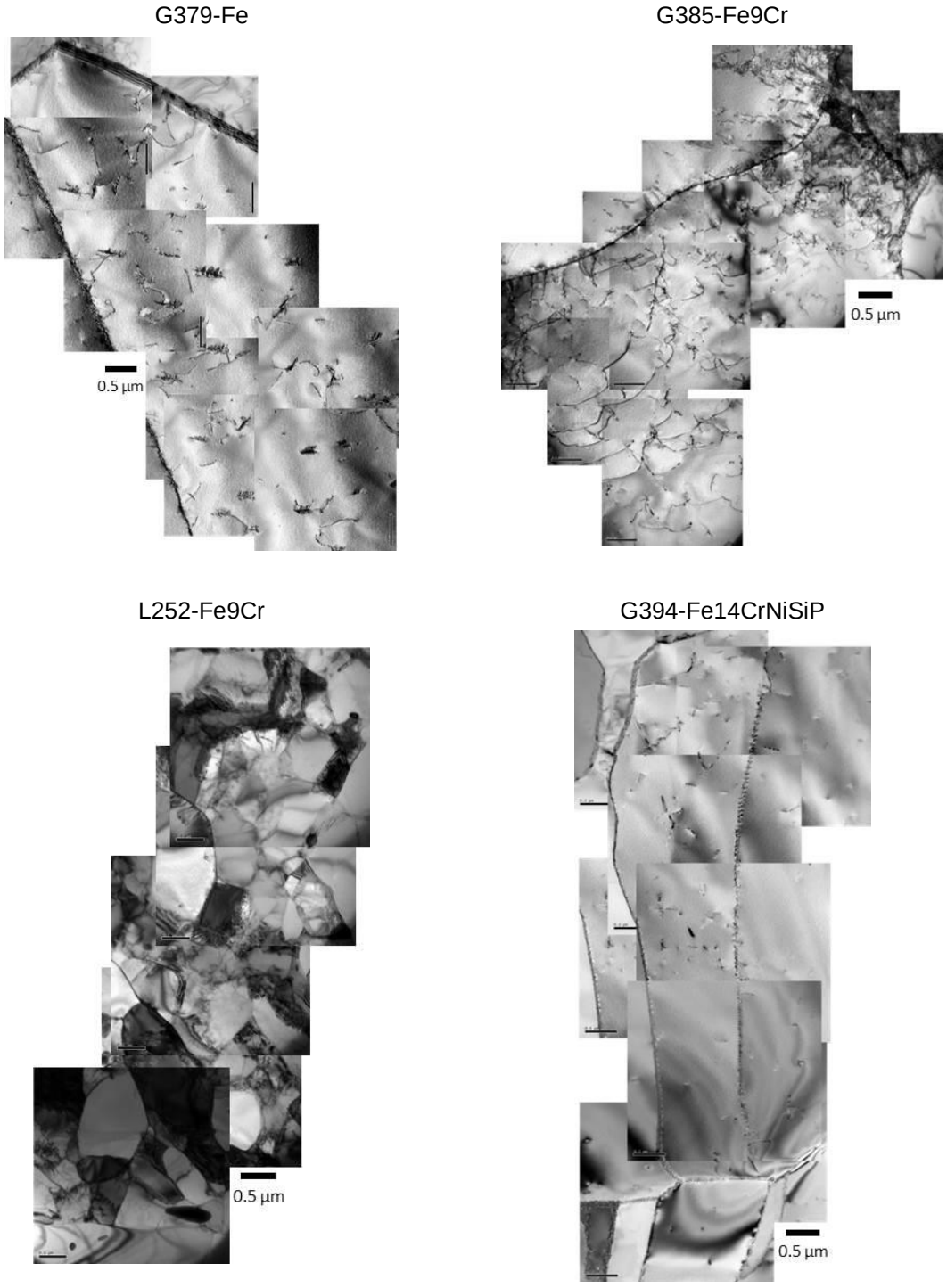

Figure 8: TEM images at low magnification showing part of the dislocation structure in the Fe9Cr alloys.

Table 7: Dislocation density in some FeCr alloys.

Material code	Dislocation density (m^{-2})
G379-Fe	(1.6±0.2) x 10^{13}
G385-Fe9Cr	(4.2±0.1) x 10^{13}
L252-Fe9Cr	(2.0±0.3) x 10^{13}
L252-Fe9Cr	(1.5±0.3) x 10^{13}

Some particular features were observed in each material. Images at higher magnification illustrating such features are shown in figures below. Figure 9 shows the type of features observed in pure iron, G379-Fe. Round features as well as rombohedric features that may be precipitates, most probably carbides, are observed at the interior of the grains, in between the dislocation segments and, sometimes, attached to them.

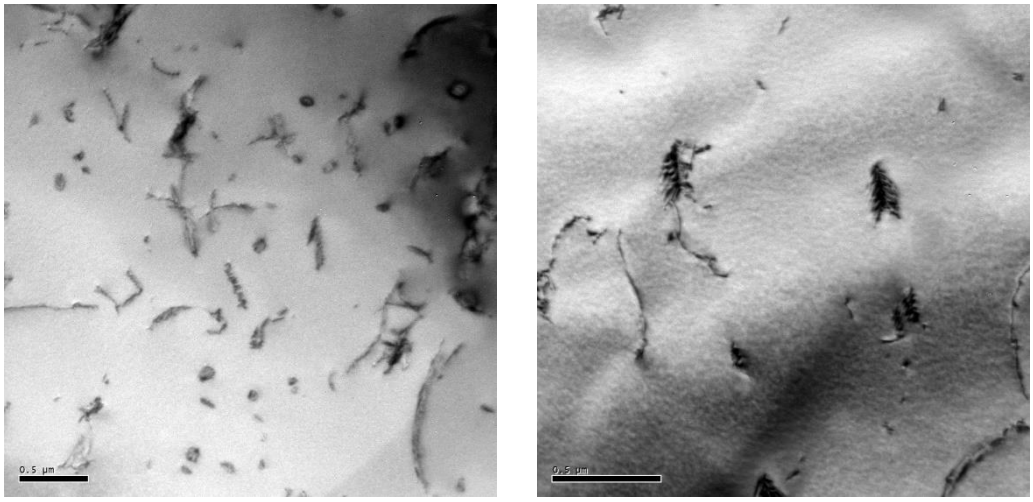

Figure 9: TEM images of non irradiated G379-Fe

Figure 10 shows TEM images of ferritic G385-Fe9Cr, in as-received condition, illustrating the presence of areas presenting different dislocation density. Some regions of small grains with very high dislocation density appear nearby regions of large, ferritic grains, with lower dislocation density, as the one shown inFigure 8 above. Some dislocations appear pinned at some points that may be small precipitates at the interior of the grains. The numbers in Table 7 refer to regions similar to the grain shown in Figure 8 or the image in the right in Figure 10, i. e., where the dislocation density is lower.

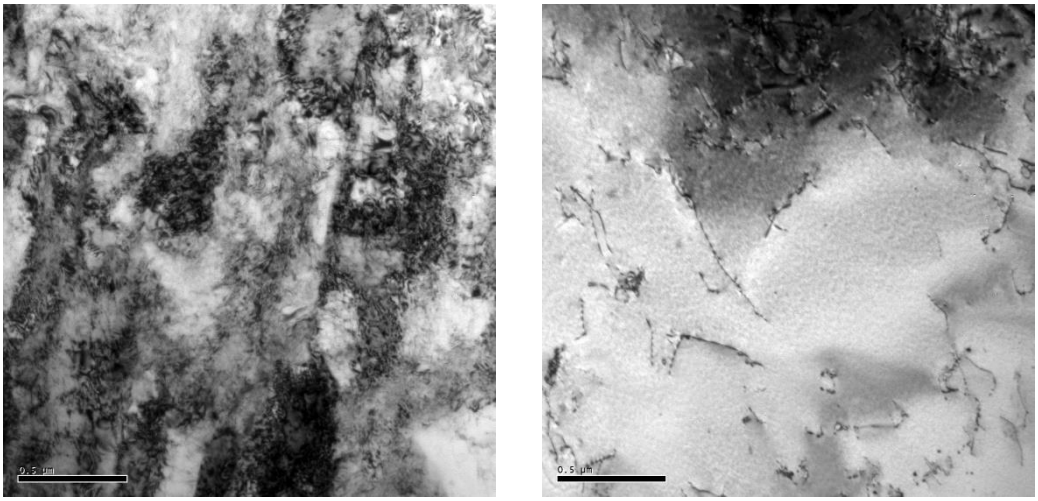

Figure 10: TEM images of non irradiated G385-Fe9Cr.

Figure 11 shows TEM images of the ferritic-martensitic L252-Fe9Cr, in as-received condition. The grain structure shows regions of small grains nearby to some ferritic larger grains. Precipitates are observed both intragranular and intergranularly, with shapes either elongated or globular.

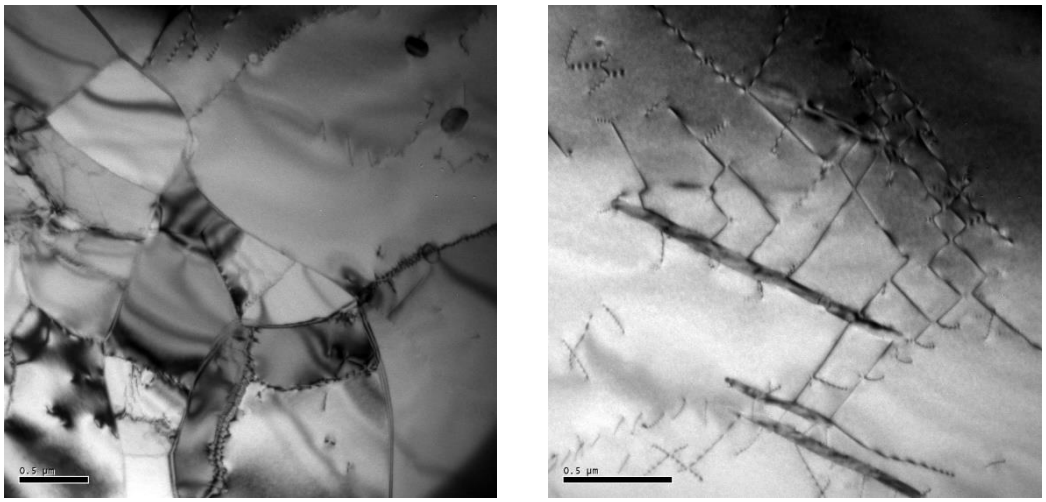

Figure 11: TEM images of non irradiated L252-Fe9Cr

Figure 12 shows a TEM image of pure iron, G394-Fe14CrNiSiP, in as-received condition. This material show the presence of quite large grains with relatively low dislocation density. It is worth noting the presence of precipitates at grain boundaries. Their nature is under study.

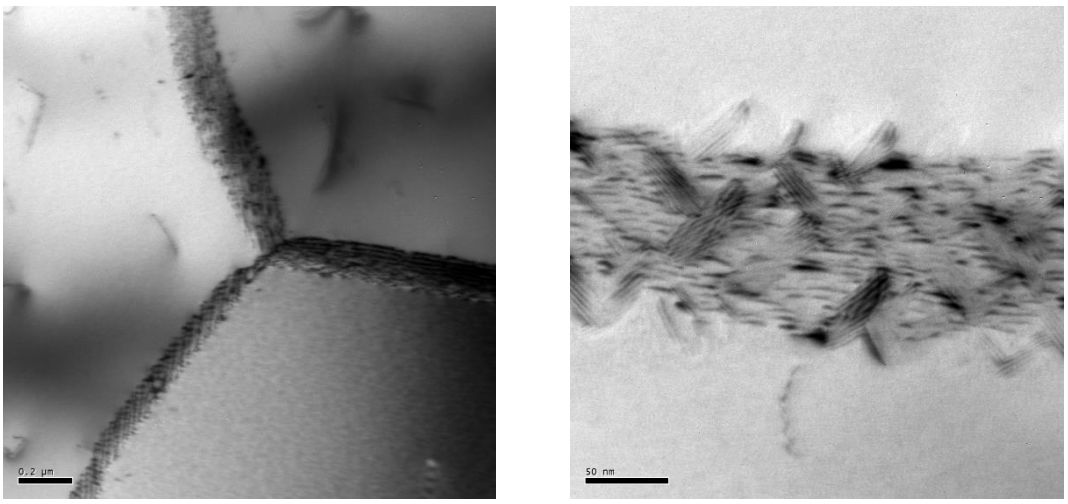

Figure 12: TEM images of non irradiated G394-Fe14CrNiSiP

3.4 Internal Friction

Internal friction spectra in the temperature range between 100 and 700 K of non-irradiated pure Fe (G379) are shown in Figure 13. They were obtained at SCK•CEN.

The temperature dependent internal friction (IF) of non-irradiated and non-deformed (ND) spectra of Fe show the existence of a peak at about 350 K which can be assigned to the relaxation of carbon atoms (Snoek peak). The intensity of the Snoek peak corresponds well to the concentration of carbon atoms, which is reported to be around 70 ppm in these alloys. The next peak is situated at about 530 K is enhanced in intensity after application of cold work (CD). This peak is conventionally associated with the relaxation of carbon atoms in the vicinity of dislocations. Table 8 summarizes the observations of carbon peaks in investigated alloys.

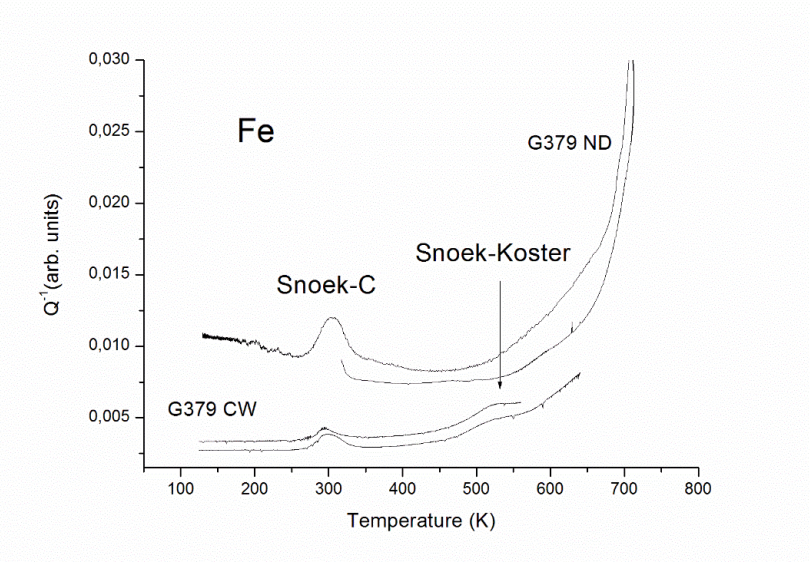

Figure 13. Internal friction spectra of non-irradiated pure Fe.

Table 8 - The presence of Snoek (carbon), and Snoek-Koster (carbon+dislocation) relaxation peaks in FeCr model alloys.

Alloy	Relaxation peaks	
	Carbon	carbon+dislocation
Fe	Y	Y
Fe5Cr	Y	N
Fe5CrNiSiP	N	N
Fe9Cr	N	N
Fe9CrNiSiP	N	N
Fe14CrNiSiP	N	Y

These results indicate the existence of carbon atoms freely distributed in the iron matrix only in Fe and Fe5%Cr alloys. In other alloys, carbon atoms are most probably associated with solute atoms, perhaps in small carbides, providing no possibility to cause the relaxation process. In pure Fe and Fe14CrNiSiP, carbon atoms are found to be bound to open volume defects (most probably dislocations or associated vacancies). While in Fe this fact usually originates from specimen production process, in Fe14CrNiSiP the presence of the Snoek-Koster peak might indicate the existence of inhomogeneity.

Neutron irradiated IF samples are too active to be tested out of the hot cell environment

3.5 APT characterisation

APT characterisation has been perfomed in order to check the composition homogeneity and the randomness of the as-received (AR) alloy. Table 9 reports the measured values in at.%.

Table 9: Nominal concentration of AR materials measured by APT. NM: Not measured.

Short Name	**Cr (at%)**	**Ni (at%)**	**Si (at%)**	**P (at%)**	**Al (at%)**	**C (at%)**	**N (at%)**	**V (at%)**	**Co (at%)**	**Cu (at%)**	**Mn (at%)**
Fe5CrNiSiP	5.3 *± 0.4*	0.096 *± 0.015*	0.38 *± 0.08*	0.028 *± 0.017*	0.058 *± 0.003*	0.02 *± 0.02*	0.04 *± 0.13*	0.005 *± 0.004*	0.004 *± 0.001*	0.001 *± 0.001*	<0.001
Fe9CrNiSiP	9.4 *± 0.4*	0.089 *± 0.002*	0.387 *± 0.008*	0.06 *± 0.03*	0.059 *± 0.003*	0.008 *± 0.008*	0.019 *± 0.018*	0.005 *± 0.006*	0.003 *± 0.001*	NM	<0.001
Fe14CrNiSiP	14.8 *± 0.4*	0.096 *± 0.014*	0.42 *± 0.04*	0.07 *± 0.06*	0.056 *± 0.003*	0.009 *± 0.019*	0.03 *± 0.02*	0.003 *± 0.019*	0.004 *± 0.001*	0.002 *± 0.001*	0.003 *± 0.002*
Fe14CrNi	15.55 *± 0.11*	0.099 *± 0.001*	0.013 *± 0.013*	0.003 *± 0.001*	0.07 *± 0.001*	0.01 *± 0.004*	0.08 *± 0.02*	0.004 *± 0.001*	0.004 *± 0.001*	NM	<0.001
Fe14CrSi	15.06 *± 0.18*	0.006 *± 0.001*	0.422 *± 0.019*	0.002 *± 0.001*	0.068 *± 0.001*	0.01 *± 0.02*	0.02 *± 0.03*	0.003 *± 0.001*	0.003 *± 0.001*	NM	<0.001
Fe14CrP	15.0 *± 0.7*	0.006 *± 0.01*	0.016 *± 0.012*	0.042 *± 0.002*	0.064 ± 0.001	0.002 *± 0.001*	0.01 *± 0.02*	0.003 *± 0.001*	0.003 *± 0.001*	0.002 *± 0.001*	0.001 *± 0.001*
Fe9Cr MIRE	8.7 *± 0.2*	0.063 *± 0.014*	0.11 *± 0.02*	0.033 *± 0.008*	<0.001	0.002 *± 0.001*	0.014 *± 0.014*	0.007 *± 0.001*	0.01 *± 0.001*	0.004 *± 0.003*	0.005 *± 0.001*
Fe12Cr MIRE	11.2 *± 0.04*	0.07 *± 0.01*	0.18 *± 0.01*	0.025 *± 0.002*	NM	NM	NM	NM	NM	NM	NM

The measured values correspond to the chemical compositions given in Table 2. Statistical tests performed on Cr, Ni, Si and P confirmed the random distribution of these species.

4 Results on neutron irradiated alloys

The list of the materials that were characterised within the project are given in Table 10 and in

Table 11. Also indicated are the techniques used in each case. Results obtained are described below in parts assigned to the different characterisation techniques. PAS was also performed on non-irradiated thermally aged alloys at 450°C to highlight only the irradiation contribution.

*Table 10: List of the neutron irradiated materials that were characterized by TEM, APT, SANS and PAS (PALS or DB). Dose: 0.11dpa where not specifyed. * DB was also performed on non-irradiated thermally aged alloys at 450°C to highlight only the irradiation contribution.*

290°C			~450°C		
ID	Short name	Characterization	ID	Short name	Characterization
G379	Fe		G379	Fe	DB*, TEM
G384	Fe-5Cr-NiSiP	SANS	G384	Fe-5Cr-NiSiP	DB*, TEM, SANS
G385	Fe-9Cr		G385	Fe-9Cr	DB*, TEM
G389	Fe-9Cr-NiSiP		G389	Fe-9Cr-NiSiP	DB*, TEM
G394	Fe-14Cr-NiSiP	SANS, PALS	G394	Fe-14Cr-NiSiP	DB*, TEM, SANS, PALS
L252	Fe-9Cr (Mart.)		L252	Fe-9Cr (Mart.)	DB*, TEM
E97	Eurofer97		E97	Eurofer97	DB*, TEM
L252	Fe9Cr (Mart.) (0.06 dpa)	APT	T91	(steel)	DB*, TEM
L253	Fe12Cr (Mart.) (0.06dpa)	APT			
	Optifer (0.8dpa)	SANS			

Table 11: List of mechanical characterisation performed on neutron irradiated materials . Dose: 0.11dpa.

290°C			~450°C		
ID	Short name	Characterization	ID	Short name	Characterization
			G379	Fe	Tensile
G384*	Fe-5Cr-NiSiP	Tensile, HV_{10}	G384	Fe-5Cr-NiSiP	Tensile, HV_{10}
G385*	Fe-9Cr	Tensile	G385	Fe-9Cr	Tensile
G389*	Fe-9Cr-NiSiP	Tensile	G389	Fe-9Cr-NiSiP	Tensile
G394*	Fe-14Cr-NiSiP	Tensile	G394	Fe-14Cr-NiSiP	Tensile, HV_{10}

4.1.1 Mechanical characterisation

4.1.1.1 Tensile tests

Tensile test results of non-irradiated and neutron irradiated samples are collected in Table 12 and Figure 14**.** Two types of specimens were used: flat and round specimens. Tensile tests were performed on round specimens for as-received alloys. These specimens are the standard ones. Nevertheless, for reasons of space available in the irradiation device, it has been only possible to irradiate flat ones. Tests on flat specimens may give different results from round specimens and are not always reliable. So the comparison of irradiated and non-irradiated data in Table 12 is not fully warranted. It is suspected that flat specimens provide lower values of characteristic tensile properties than round specimens.

Table 12 - Summary of mechanical test results on ferritic model alloys and steels.

Material	As received			Aged at 450 ^{0}C for 6 weeks			Irradiated to 0.11 dpa			
	Test temp (^{0}C)	Yield strength (MPa)	Specimen type	Test temp (^{0}C)	Yield strength (MPa)	Specimen type	Irr temp (^{0}C)	Test temp (^{0}C)	Yield strength (MPa)	Specimen type
G379 Fe	22	184	round (L)	22	136	flat	450	25	185	Flat
	23	180	round (T)	300	105	flat				
				-100	391	flat				
				22	64	flat				
G384 Fe5CrNiSiP	23	221	round (L)	22	147	flat	290	25	372	Flat
	22	235	round (T)	300	143	flat	290	25	379	Flat
				-100	360	flat	450	25	247	Flat
				22	191	flat				
G385 Fe9Cr	23	241	round (L)	22	169	flat	290	25	191	Flat
	23	263	round (T)	300	136	flat	290	25	211	Flat
				-100	382	flat	450	25	182	Flat
				23	193	flat				
G389 Fe9CrNiSiP	23	243	round (L)	22	183	flat	290	25	444	Flat
	23	247	round (T)	300	124	flat	290	25	426	Flat
				-100	347	flat	450	25	418	Flat
				22	140	flat				
G394 Fe14CrNiSiP	23	229	round (L)	22	220,102	flat	290	25	403	Flat
	22	242	round (T)	300	147,104	flat	290	25	438	Flat
				-100	347,895	flat	450	25	421	Flat
				22	206,025	flat				

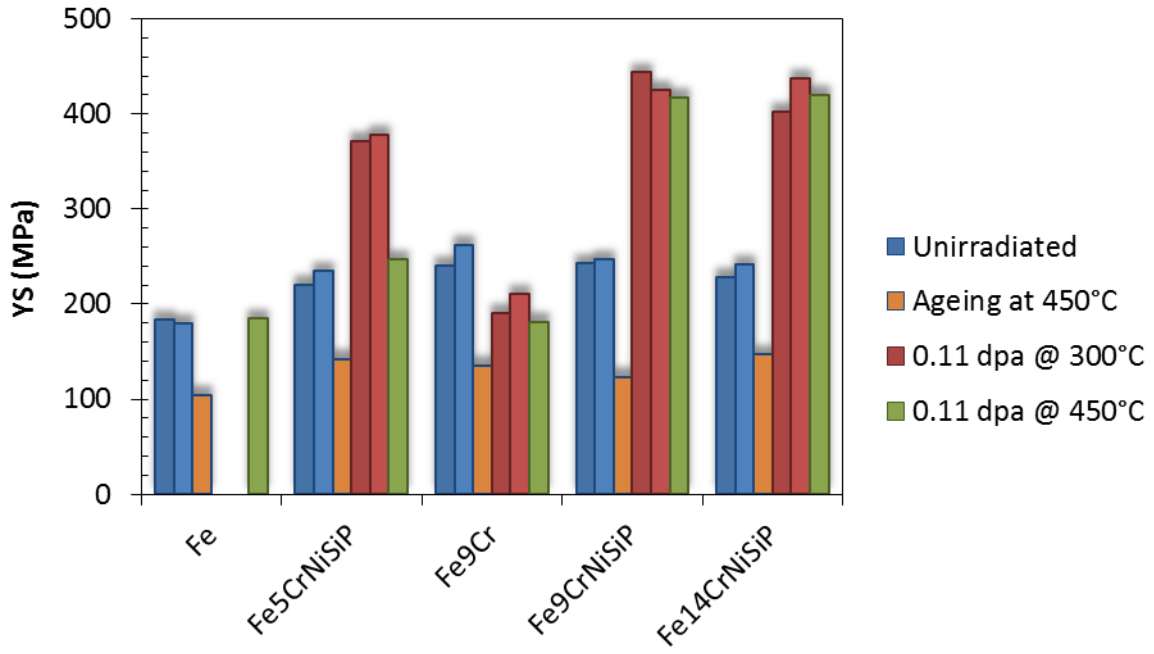

Figure 14: Yield strength of non-irradiated and neutron irradiated samples at 450°C and 300°C.

The ageing for 6 weeks at 450°C decreased significantly the yield strength of FeCr model alloys. Since the materials irradiated were exposed for 6 weeks not only to neutrons but also to 450°C, the yield after ageing is probably the most adequate reference to assess irradiation hardening in terms of yield increase. Moreover, the same type of specimen (flat) was used in this case. It appears that FeCr model alloys show different behaviour under neutron irradiation depending on their chemical composition. For the samples which were neutron irradiated at 300°C, Fe9Cr does not harden if compared to the as-received values (one might even say that it softens a bit) while Fe5CrNiSiP, Fe9CrNiSiP and Fe14CrNiSiP show significant hardening. After neutron irradiation at 450°C, Fe9Cr does not harden whereas Fe9CrNiSiP and Fe14CrNiSiP show significant hardening. Concerning Fe5CrNiSiP, it shows similar hardening as the non-irradiated sample which is thermally aged at 450°C but shows hardening with respect to the sample thermally aged at 450°C.

4.1.1.2 Hardness

Two sets of hardness measurements were performed. The first set covered all unirradiated materials distributed within the Work package of MatISSE as a kind of intake inspection and contribution to the basic characterization. The results are summarized in Table 13 (average values out of four measurements for each material).

The second set of Vickers hardness measurements is aimed to estimate the neutron-irradiation-induced hardness increase. It is important to note that only one neutron-irradiated sample from each material was delivered to HZDR in order to perform SANS and GiPS measurements and that Vickers hardness as a destructive method can only be applied after completion of SANS and GiPS. This means that Vickers hardness measurements (although feasible at any time) are only available for a small subset of samples by now. This is not a serious drawback, because the main objective of the respective HV10 measurements is to be correlated with volume fraction derived from SANS.

For each studied neutron-irradiated sample and unirradiated reference sample, eleven hardness tests were performed to calculate the average value and standard deviation of HV10 as well as ΔHV10. The results are compiled in Table 13.

Table 13: Hardness measurements performed on unirradiated and neutron irradiated Fe-5Cr(NiSiP) and Fe-14Cr(NiSiP) alloys.

Material	Fe-5Cr (NiSiP)			Fe-14Cr (NiSiP)		
Code	G384			G394		
Irradiation (0.1 dpa)	unirrad.	290 °C	450 °C	unirrad.	290 °C	450 °C
Average HV10	108	176	171	122	216	201
Standard deviation	2	4	4	3	6	5
Average ΔHV10	-	68	63	-	94	79
Standard deviation	-	5	5	-	6	6

4.1.2 PAS

4.1.2.1 Doppler Broadening

The results of coincidence Doppler broadening (CDB) positron annihilation experiments performed at SCK•CEN are shown in Figure 15. The results of the CDB measurements for non-irradiated materials are given in Figure 15a), where the W parameter is plotted as a function of S parameter for all alloys and steels, including the data for pure Fe [32]. It is found that the steels exhibit somewhat higher S parameter and lower W parameter than the Fe-Cr-C alloys. Typically this effect occurs due to higher dislocation density and more complex chemical composition of steels in comparison with model alloys.

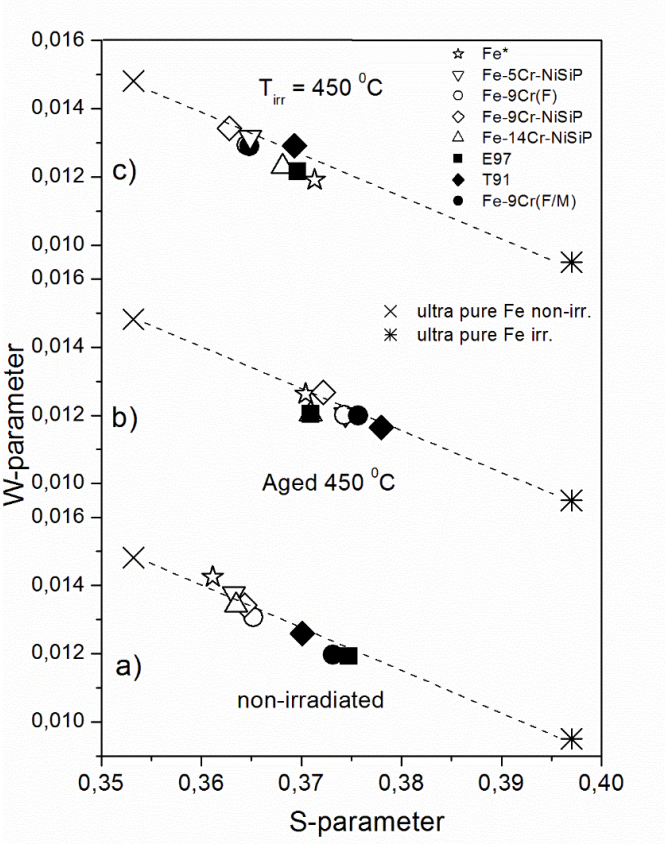

Figure 15. W versus S parameter of a) non-irradiated, b) termally aged at 450 ^{0}C, and c) neutron irradiated at 450 ^{0}C FeCr alloys and steels.

Thermal aging at 450 ^{0}C caused the increase of the S parameter and decrease of the W parameter in Fe, Fe5CrNiSiP, Fe9Cr, Fe9CrNiSiP and Fe14CrNiSiP, see Figure 15b. E97 and T91 as well as F/M Fe9Cr alloy are found not to be affected by thermal ageing. Such an effect could be the consequence of the formation of small carbon-vacancy clusters in the steels, due to the quenching / rapid cooling after thermal treatment.

The results of CDB measurements for the alloys and steels irradiated at 450°C are given in Figure 15c. Clearly, the S and W parameters of the model alloys are similar to the non-irradiated case. However, a significant

decrease of the S parameter (and consequently an increase of W) is observed for both steels and F/M alloys. These results suggest that significant dislocation annealing has occurred under neutron irradiation at 450 ^{0}C.

4.1.2.2 PALS

Positron annihilation lifetime spectroscopy was performed for Fe-14Cr-NiSiP (material G394) by means of Gamma-induced Positron Spectroscopy (GiPS) at HZDR. The measured lifetime (LT) distributions of the three different conditions are shown in Figure 16 as symbols, where the corresponding dashed lines represent the two/three component fit results using the PALSfit software package. The extracted resolution function of the test set-up with the full width at half maximum, FWHM = 0.1750 ns, is also plotted in this diagram. Additionally, three lines are indicated typical for LT-components of bulk material (0.108 ns), 1 vacancy (0.175 ns), and vacancy clusters of about 4 vacancies (0.252 ns) [33,34]. The results after decomposition of the spectra are summarized in Table 13.

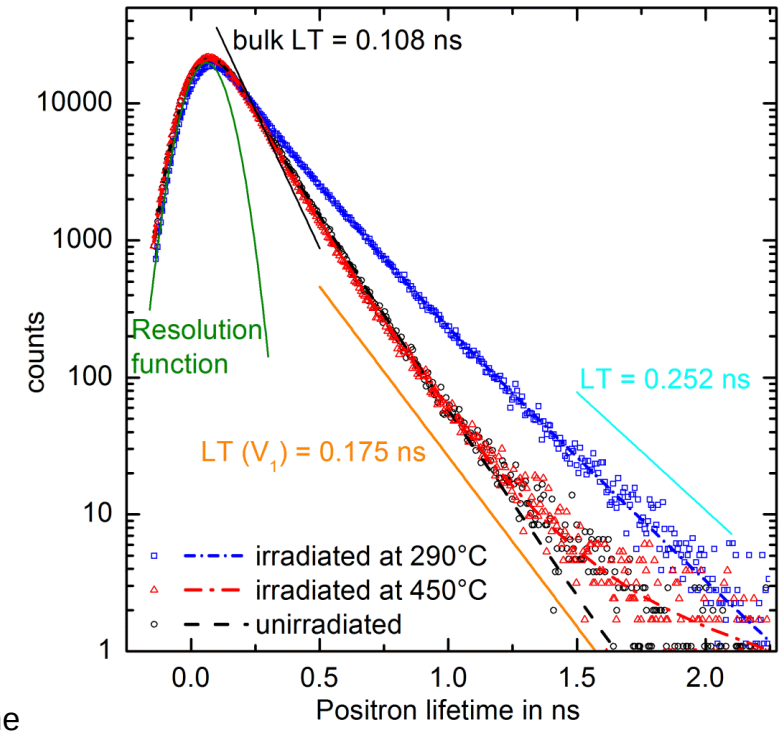

the

Figure 16: Positron Lifetime spectra of three conditions of Fe-14Cr-NiSiP (symbols), data fits by PALSfit (dashed lines) and obtained lifetime components (straight lines) after the decomposition.

The mean LT of positrons in the material, which was irradiated at 290°C, is 0.189 ns and therefore significantly higher than in the unirradiated reference and the irradiated condition of 450°C. Only 16% of all positrons annihilate directly in the bulk. The dominant trapping center of positrons is the single vacancy (0.175 ns). In addition, a further LT component occurs at 0.252 ns. 32% of all positrons were trapped in this type of defect, which can be interpreted as clusters of about 4 vacancies.

Table 14: Decomposition of LT components of the measured spectra in Figure 16.

Condition	Component	LT in ns	Intensity in %
unirradiated reference	1 2	0.108 0.162 ± 0.001 mean LT = 0.139	41.73 ± 1.54 58.27 ± 1.54
irradiated at 450°C	1 2 3	0.108 0.175 0.768 ± 0.139 mean LT = 0.134	62.74 ± 0.35 37.05 ± 0.37 0.21 ± 0.04
irradiated at 290°C	1 2 3	0.108 0.175 0.252 ± 0.004 mean LT = 0.189	15.84 ± 1.18 52.10 ± 3.28 32.06 ± 2.17

4.1.3 SANS

4.1.3.1 MatISSE model alloys

SANS measurements were performed for Fe-5Cr-NiSiP (material G384) and Fe-14Cr-NiSiP (material G394) of the unirradiated reference and the irradiated conditions at 290°C and 450°C, respectively. The complete set of measured magnetic scattering cross sections is shown in Figure 17 as a function of scattering vector, Q. Increased intensities were observed for all irradiated conditions at high Q-values. This increase is caused by irradiation-induced clusters and other features. The two configurations of the instrument, the two used sample-detector distances and corresponding collimation lengths, show an accurate data overlap (full and open symbols in Figure 17) after the calibration.

For the Fe-5Cr-NiSiP (Figure 17a) all conditions converge at $Q < 0.15$ nm^{-1}. The intensity in this region follows the Q^{-4} dependence. This is caused by the presence of the same large structures of dimension > 50 nm. The increased intensity at $Q > 0.2$ nm^{-1} in comparison to the unirradiated reference is caused by irradiation-induced features with radii up to about 4 nm. The unirradiated reference was subtracted in order to reconstruct their size distribution. These scattering curves are shown in Figure 18a together with the data fits corresponding to the size distributions plotted in

Figure 19a. The mean radius of irradiation-induced clusters is significantly larger for the irradiation at 450°C. Also the volume fraction increases slightly. Parameters of irradiation-induced features determined by SANS are summarized in Table 15. Based on the measured A-ratio of 3.5 for both temperatures, the type of clusters is unchanged. This A-ratio is consistent with clusters already identified in Fe-Cr alloys with less than 9%Cr, irradiated to different dpa as part of the Mire-Cr campaign [2].

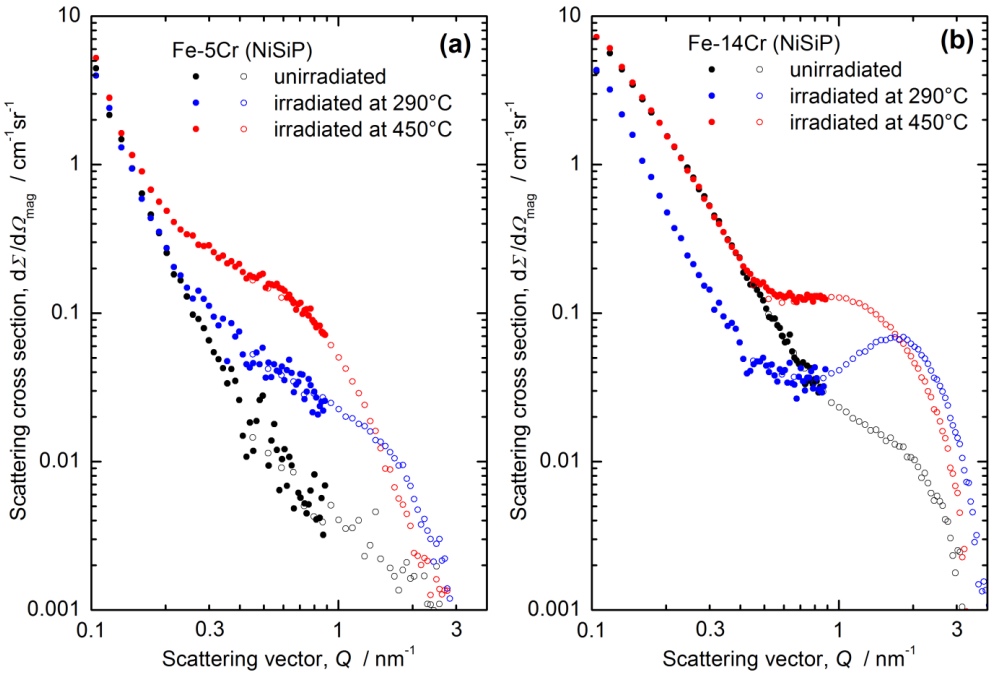

Figure 17: Measured magnetic scattering cross sections of different conditions of (a) Fe-5Cr-NiSiP (G 384) and (b) Fe-14Cr-NiSiP (G 394). Open and full symbols correspond to the measurements at 1.8 m and 8 m sample-detector distance, respectively.

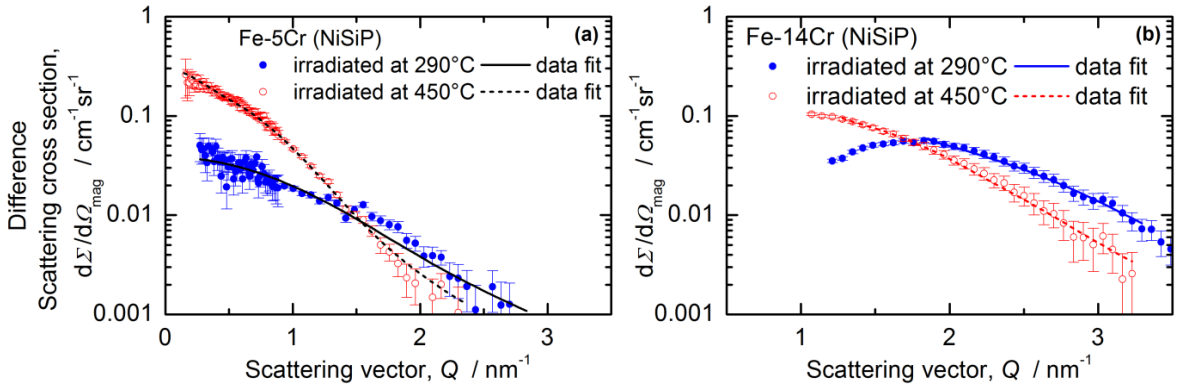

Figure 18: Measured magnetic difference scattering curves with the respective unirradiated conditions as reference for (a) Fe-5Cr-NiSiP (G 384) and (b) Fe-14Cr-NiSiP (G 394). Lines represent fits needed in order to reconstruct size distributions.

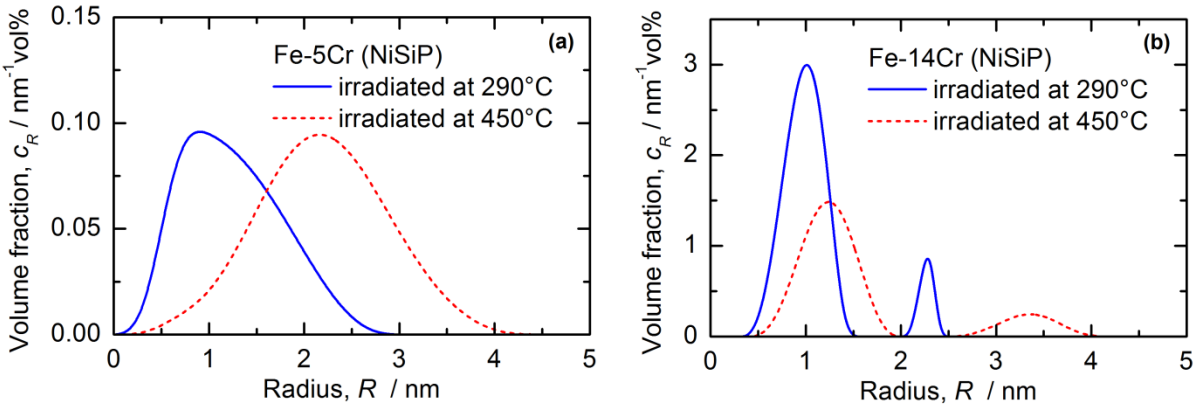

Figure 19: Size distribution of irradiation-induced clusters for (a) material G384 and (b) material G394.

Table 15: Parameter of irradiation induced features determined by SANS

Condition	Volume fraction in %	Mean radius in nm	Number density in 10^{22} m^{-3}	*A*-ratio
Fe5CrNiSiP- 290°C	0.13 ± 0.01	0.97 ± 0.08	27 ± 3	3.5 ± 0.5
Fe5CrNiSiP - 450°C	0.16 ± 0.01	1.49 ± 0.07	16 ± 1	3.5 ± 0.5
Fe14CrNiSiP - 290°C	1.75 ± 0.09	0.83 ± 0.08	592 ± 76	2.15 ± 0.25
Fe14CrNiSiP - 450°C	1.10 ± 0.09	1.07 ± 0.08	174 ± 27	2.15 ± 0.25

The measured SANS intensities for the Fe-14Cr-NiSiP (Figure 17) are significantly higher in comparison to Fe-5Cr-NiSiP. This applies to all conditions. The unirradiated reference and the irradiated condition of 450°C converge already at Q < 0.5 nm^{-1}, whereas the intensity of the irradiated condition at 290°C for Q < 0.8 nm^{-1} is lower than the unirradiated reference. The reason for this behaviour is interparticle interference in the case of high density of scattering centres. This caused a reduction of intensity at lower Q-values and explains the appearance of intensity maxima for both irradiation conditions.

The size distribution (see

Figure 19b) was calculated from the difference scattering curves in Figure 18b without consideration of a structure factor of interparticle interference. To this end, only the data beyond the local maximum of the scattering curve were fitted. In addition, the integral intensity of SANS, the so-called "invariant", was calculated in order to estimate correctly the total volume fraction of the scatterers. The uncertainty of the integral due to the limited measured Q-range can be estimated to be about 5%.

The size distributions of the irradiation-induced features in Fe-14Cr-NiSiP are presented in

Figure 19b. Two components can be discerned at both irradiation temperatures. The mean size, volume fraction and number density of the scatterers presented by the first and second peak are summarized in Table 15 along with the data obtained when considering the distribution as a whole. The first component is dominant in terms of number density and volume fraction. The A ratio (2.15) which is dominated by this component indicates α' formation. The number density of the second component is two orders of magnitude lower. The volume fraction of irradiation-induced clusters in Fe-14Cr-NiSiP is one order of magnitude higher than in Fe-5Cr-NiSiP.

4.1.3.2 Optifer

SANS measurements have been carried out on irradiated Optifer II steel (9.5 Cr, 0.125 C, 0.49 Mn, 0.006 W, 0.28 V, 0.018 Ta, 0.0059 B Fe bal wt%), made available by the Karlsruhe Institut for Technology (KIT-IAM). The investigated sample had been submitted to preliminary thermal treatment (1075 °C 30 min + 780 °C 2 h), then neutron irradiated at HFR-Petten to 0.8 dpa at 250°C. A reference, un-irradiated sample, submitted solely to the same thermal treatment as the irradiated one, has also been investigated. Transmission Electron Microscopy (TEM) observations on this irradiated sample and other similar ones are reported in ref. [35] : in Optifer II irradiated at 250°C, dislocations loops, α' clusters and small helium bubbles (approximately 20 Å in size) were locally observed, the latter probably originated by □ transmutations. The observed irradiation hardening and changes in the fracture mode were tentatively correlated with the density of such micro-structural defects.

The SANS measurements have been carried out at the D22 instrument, Institut Max von Laue Paul – Langevin (ILL), Grenoble. Sample-to-detector distances of 3 m and 6 with neutron wavelength 6 Å, and of 17 m, with neutron wavelength 11.5 Å, were selected. The corresponding experimental Q interval ranged from 0.001 $Å^{-1}$ to 0.2 $Å^{-1}$ approximately. An external magnetic field of 1 T was applied to saturate the magnetization in the samples and investigate separately the nuclear and the magnetic SANS components. SANS raw data calibration and determination of SANS cross-sections in physical units were carried out by the "GRASP" program, available at the ILL; the SANS components parallel and perpendicular to the magnetic field (nuclear and nuclear plus magnetic, respectively) were determined by selecting approximately 15° wide sectors around the corresponding directions in the detector plane. The 2-dimensional SANS patterns detected for the 17 m and 11.5 Å configuration are shown in Figure 20. The nuclear and nuclear plus magnetic SANS components are shown in Figure 21. In the Q-range corresponding to defect sizes approximately 10 Å to 50 Å, no difference can be detected between the irradiated and the reference sample. Differences are detected for Q values corresponding to sizes larger than 150 Å approximately, suggesting that the irradiation might have reduced the density of pre-existing, large metallurgical inhomogeneities (including possibly magnetic domains). However, more detailed TEM information would be needed to check this hypothesis.

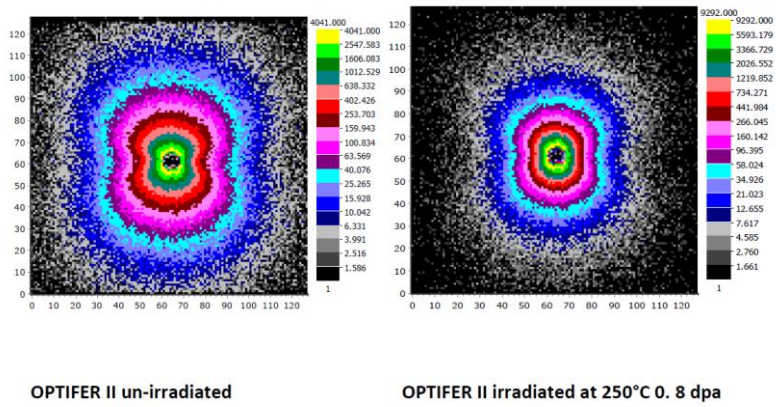

Figure 20: 2D SANS raw patterns for the investigated samples (17 m, λ = 11.5 Å, external magnetic field horizontal in the plane of the figure).

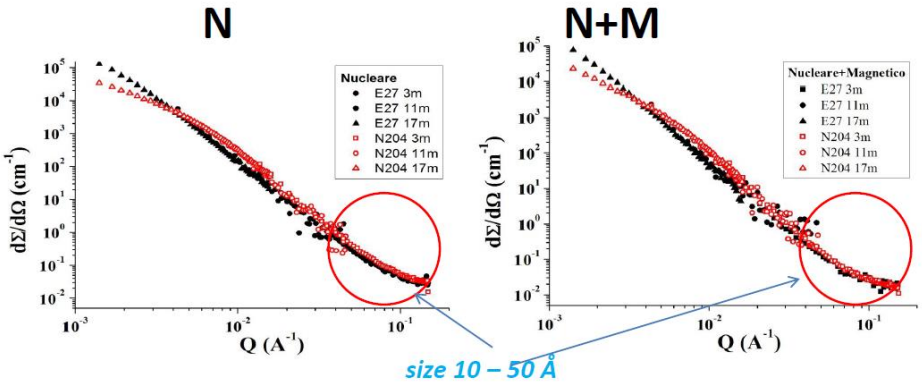

Figure 21: SANS cross sections parallel (N) and perpendicular (N+M) to magnetic field, for OPTIFER II un-irradiated (red) and irradiated at 250°C 0.8 dpa (black).

The ratio of the two SANS components, perpendicular to parallel to the magnetic field, is weakly depending on Q and close to 2 for both samples, suggesting the presence of non-magnetic inhomogeneities, such as $M_{23}C_6$ carbide clusters: in fact, if there is also a contribution from micro-voids or helium bubbles in the irradiated sample, it is too low to be detected with the available resolution.

This result is in agreement with previous SANS measurements, carried out in a narrower Q-range (Q > 0.01 $Å^{-1}$), on similar steels, neutron irradiated at 250°C 0.8 dpa, namely OPTIFER I (9.3 Cr wt %) [36,37] and F82H-mod. (7.73 Cr wt%) [38]: no SANS difference could be detected between irradiated and reference samples. In contrast, irradiation to 2.4 dpa produced in these same steels well detectable SANS effects, discussed in the refs [36–38]. In the case of MANET steel (10.5 Cr wt%), polarized SANS measurements detected a significant increase in SANS cross section after irradiation at 250°C 0.8 dpa, with significant changes in the nuclear-magnetic interference term and in the ratio of the two SANS components: based also on TEM results, such effects were tentatively attributed to the occurrence of small α' clusters [39]. Further changes were observed on another MANET sample, tempered 2 h at 525°C after neutron irradiation at 250°C 0.8 dpa, tentatively attributed to micro-voids [39]. In summary, the SANS characterization of technical steels, with low Cr content, irradiated for dose levels lower than 1 dpa, appears very difficult, probably due to the very small volume fractions of the defects: these are locally observable by TEM, but apparently do not give rise to a detectable SANS effect. It is worth noting the importance, in the investigation of such complex steels, of extending the SANS measurements over a Q range as large as possible.

ACKNOWLEDGMENT: Dr. R. Lindau (KIT) is gratefully acknowledged for providing the OPTIFER II samples and organizing their transportation to the neutron source.

4.1.4 TEM

TEM has been applied to the examination of neutron irradiated FeCr alloys: pure Fe, Fe9Cr and Fe9CrNiSiP[1]. The investigation of the neutron irradiated microstructures of these three materials may provide information about the effect of Cr content and the effect of the presence of impurities such as Ni, Si and P. Next figures show examples of the microstructure observed by TEM after neutron irradiation at 450ºC and up to 0.11 dpa. Figure 22 shows TEM images of the microstructure of neutron irradiated pure Fe.

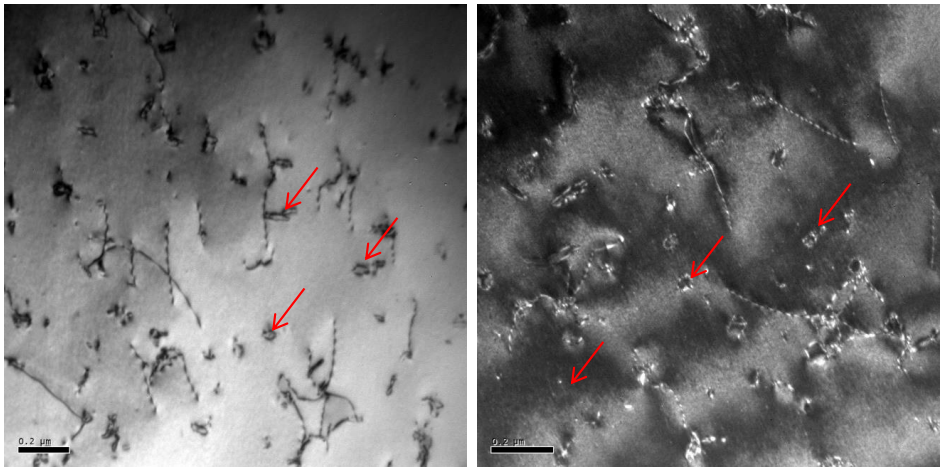

Figure 22: BF and WBDF TEM images of G379-Fe neutron irradiated at 450ºC up to 0.11 dpa (Note magnifications are slightly different).

The presence of large dislocation loops was found, some examples are arrowed in the figure above. Small dots also appear in the matrix when imaging in WBDF conditions. The loops are distributed all over the sample, though with a fairly low number density. Large loops may reach about 50 nm in diameter, in spite of the very low neutron fluence of 0.11 dpa. Burgers vector analysis has not been performed yet, though according to results reported in literature in similar irradiation conditions, they are most probably <100> type.

Figure 23 below shows TEM images of the neutron irradiated microstructure of Fe9Cr. (Note the magnification of the left image is similar to images in Figure 22, while the one on the right is higher).

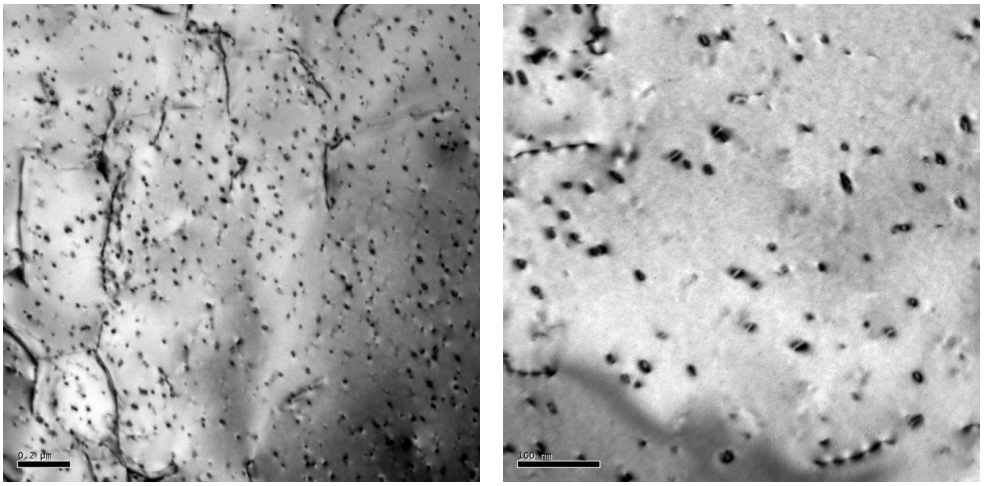

Figure 23: BF TEM images of G385-Fe9Cr neutron irradiated at 450ºC up to 0.11 dpa, for two different magnifications.

[1] The quality of the specimen fabricated from the neutron irradiated L252-Fe9Cr (F/M) was not good enough to perform the TEM examination.

Dislocation loops are observed all over the examined region in Fe9Cr, neutron irradiated at 450ºC, up to 0.11 dpa. They appear distributed quite homogenously. However, the amount of loops appears higher close to some grain boundaries than at the interior of the grains: this point will need further assessment. In general, no other inhomogeneities are observed, for instance, no dislocation decoration is observed. Loop sizes are about 10-20 nm. It is not quantified yet, but qualitatively it is possible to say that the size of the loops is notably smaller and the number density much higher than in pure Fe. Burgers vector analysis of the loops is in course.

Finally, examples of the neutron irradiated microstructure of Fe9CrNiSiP alloy are shown in Figure 24 below. (Note magnification is higher in these images)

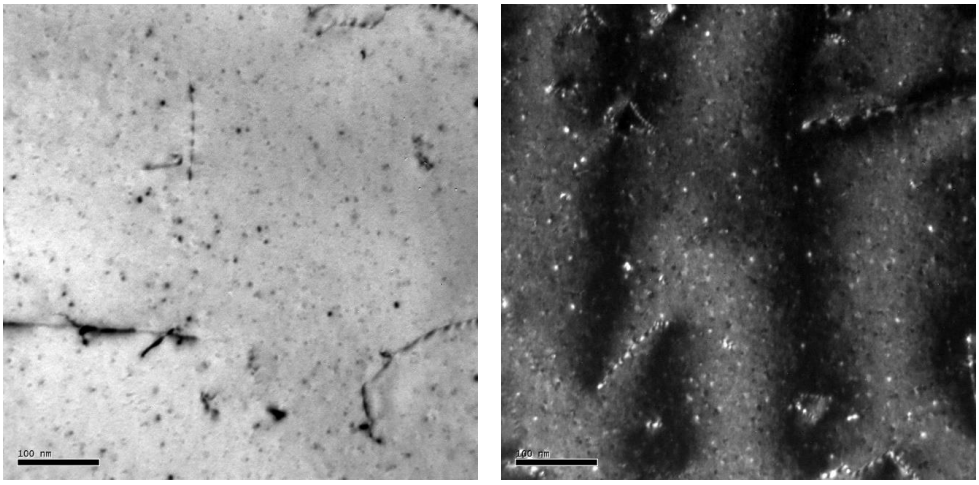

Figure 24: BF and WBDF TEM images of G389-Fe9CrNiSiP neutron irradiated at 450ºC up to 0.11 dpa.

TEM examination reveals the presence of small black dots caused by irradiation in Fe9CrNiSiP. They are distributed homogeneously all over the examined region. Though not yet quantified, comparison with images in Figure 22 and 23 allows one to deduce that loop size is much smaller than in the case of pure Fe9Cr and drastically smaller than in pure Fe. Regarding loop number density, it appear much higher than in the other two alloys, but this fact needs quantitative confirmation as, depending on the specimen orientation, part of the loops may not be visible and direct comparison is not possible. Burgers vector analysis of the loops is in course.

Figure 25 compares the irradiated microstructure of the three alloys. As explained above, a qualitative comparison of TEM images leads to deduce that the presence of Cr reduces size and increases the number density of loops, the effect of Ni, Si and P addition being to further reduce loop size and increase loop number density.

G379-Fe G385-Fe9Cr G385-Fe9CrNiSiP

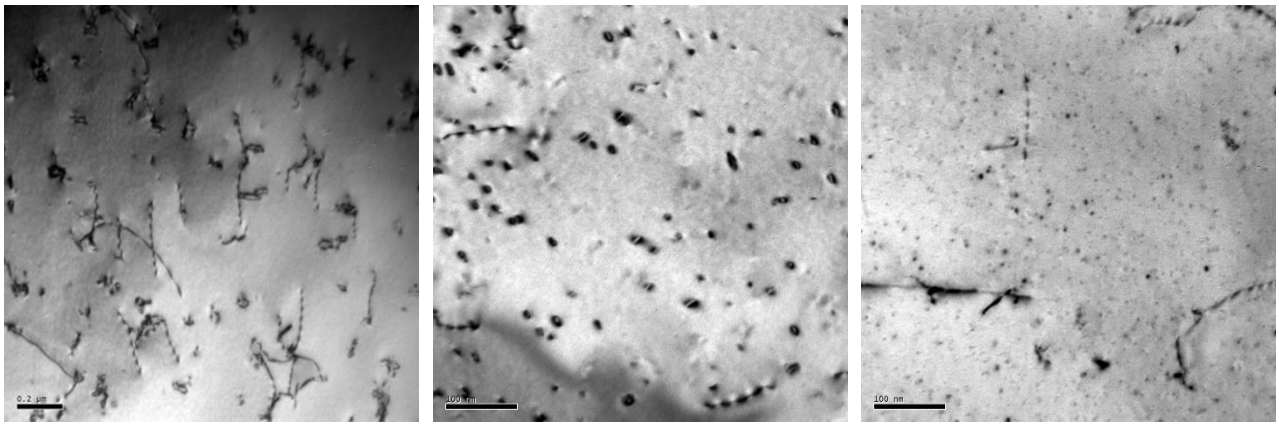

Figure 25: Examples of TEM images comparing the observed microstructure after neutron irradiation at 450ºC up to 0.11 dpa.

Note about other features:

As shown in pictures below, taken under out-of-focus imaging conditions, it is possible to see features whose contrast behaves as the one of voids, i.e., white contrast in underfocused condition and black in over-focused conditions.

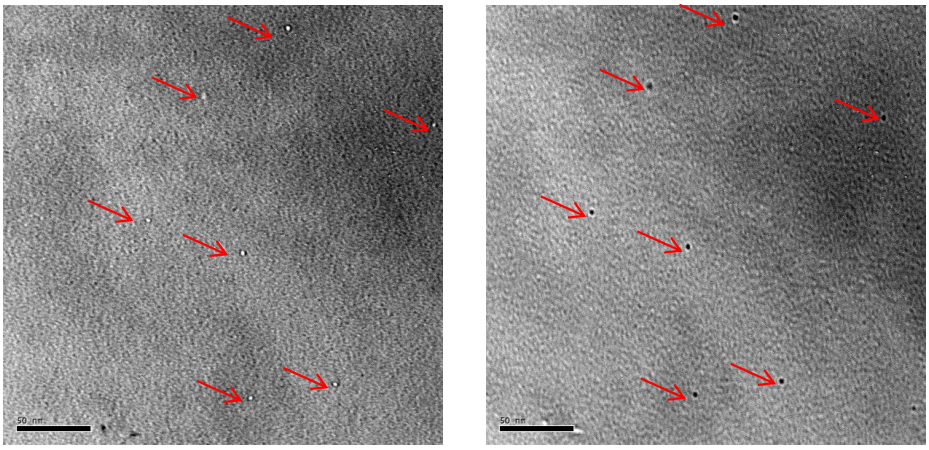

Figure 26 *shows such type of images in the case of pure Fe.*

Images under out of focus conditions in Fe9Cr and Fe9CrNiSiP, neutron irradiated are also shown below in

Figure *27*. Features whose contrast behaves as explained above are also observed. However, their size is quite large and number density seems also to be quite high. This issue still needs further assessment as one possible origin of these objects may be surface features on the specimen due to some contamination during sample preparation.

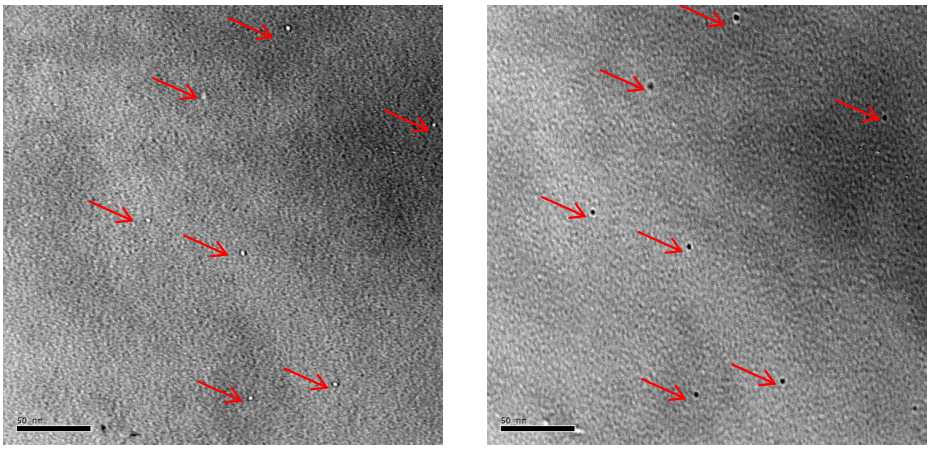

Figure 26: TEM images at under-focus (left) and over-focus (right) conditions showing the presence of voids in G379-Fe after neutron irradiation at 450ºC, 0.11 dpa.

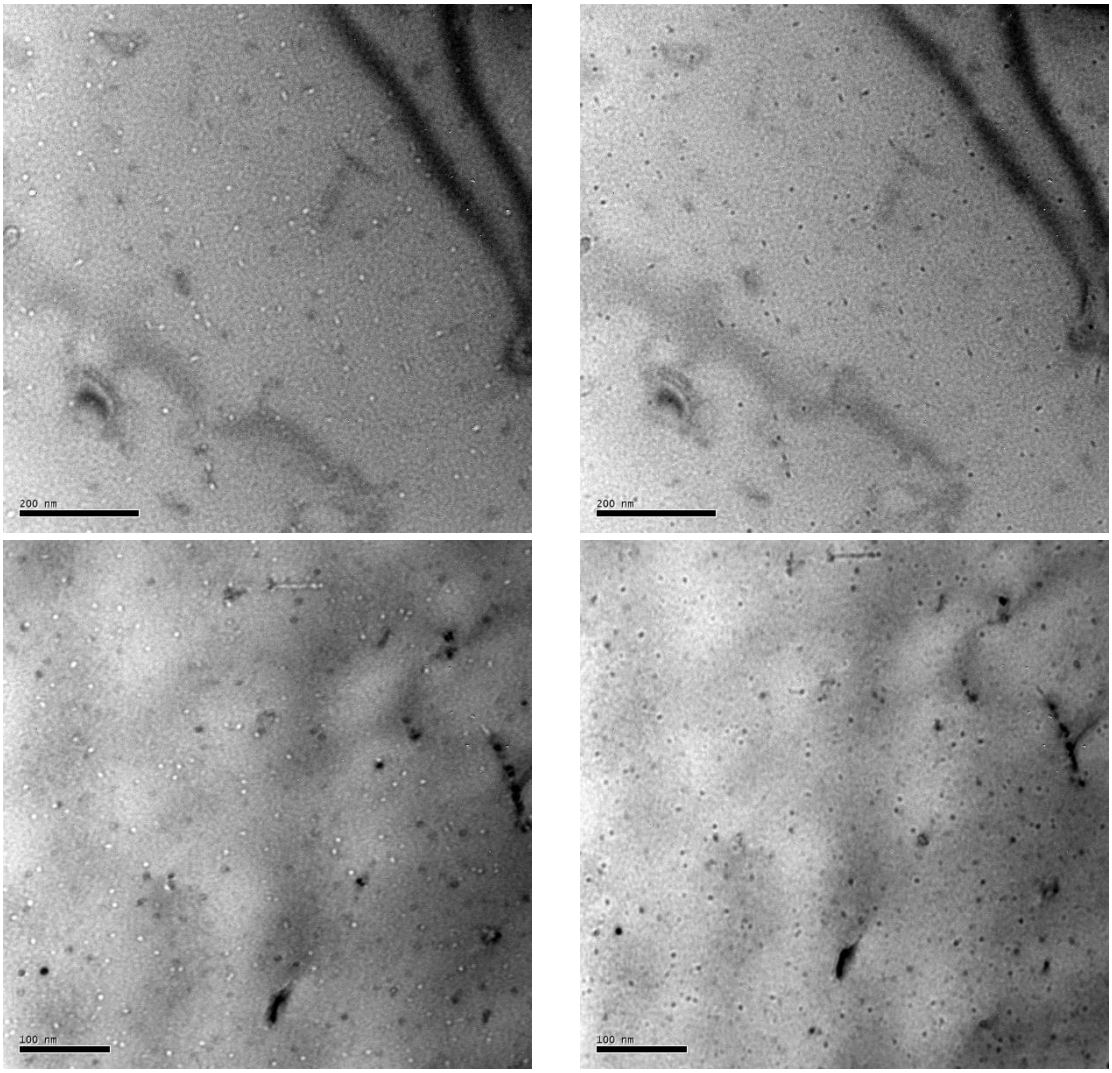

Figure 27: TEM images at under-focus (left) and over-focus (right) conditions showing the presence of features of unknown origin in G385-Fe9Cr (above) and G389-FeCrNiSiP (below) after neutron irradiation at 450ºC, 0.11 dpa. (Note magnification is higher in images below).

4.1.5 APT

APT investigation has been performed on Fe-9%Cr and Fe12%Cr MIRE-Cr neutron irradiated alloys at a dose of 0.06 dpa at 290^{0}C [2]. These materials were irradiated within the MIRE-Cr campaign and characterised using SANS, TEM and PALS [2,40]. They were also studied under different irradiation conditions during the GETMAT project [2,41–46]. However, no APT analysis had been performed so far. APT characterization shows that only NiSiPCr-enriched clusters are observed at 0.06dpa. There is no α' phase, at variance with observations at 0.6 dpa [44].

Figure 28 shows the volume fraction (Fv (%)), the number density (Nv (m^{-3})) and the average cluster radius (R (nm)) together with the composition of the clusters in both Fe-9Cr MIRE and Fe-12Cr MIRE. All these characteristics are similar in both materials. The solute rich clusters (SRC) are very rich in P and present a only a very slight Cr enrichment, if any. As in results obtained at 0.6 dpa, no carbon enrichment due to irradiation has been found in the samples.

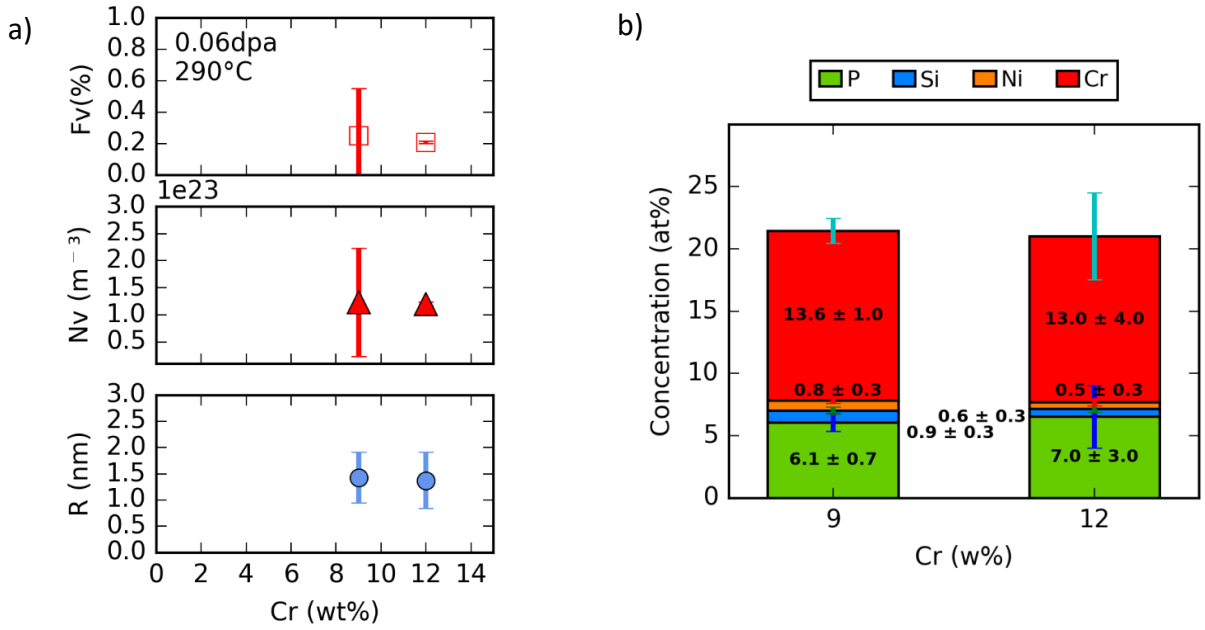

Figure 28: Cluster characteristics of neutron-irradiated Fe-9Cr MIRE and Fe-12Cr MIRE at 0.06 dpa at 290^{0}C as a function of the %Cr. a) Fv, Nv and R of the SRCs, b) Solute concentration of the clusters.

A comparison of the current results with those obtained at 0.6 dpa [44] is presented in

Figure 29. The data of ref. [44] have been retreated using the new version of the data software and the same threshold as the one used at 0.06 dpa. These are the data presented in

Figure 29.

There is a slight increase in number density and in volume fraction with dose and a slight decrease in size. Concerning composition, a very clear increase in Si, Ni and Cr content is observed at higher dose. This is coherent with the fact that these species have much lower diffusion coefficient than P and more time is needed for them to enriched clusters.

A grain boundary (GB) was found and analysed in the Fe-12Cr MIRE material irradiated at 0.06 dpa. It is shown in Figure 30. P and Si atoms are segregated at the GB. An area free of clusters is found close to the GB. The SRCs found near the GB have the same composition and radius values, within the experimental uncertainties, as the purely intra-granular clusters analysed in other tips.

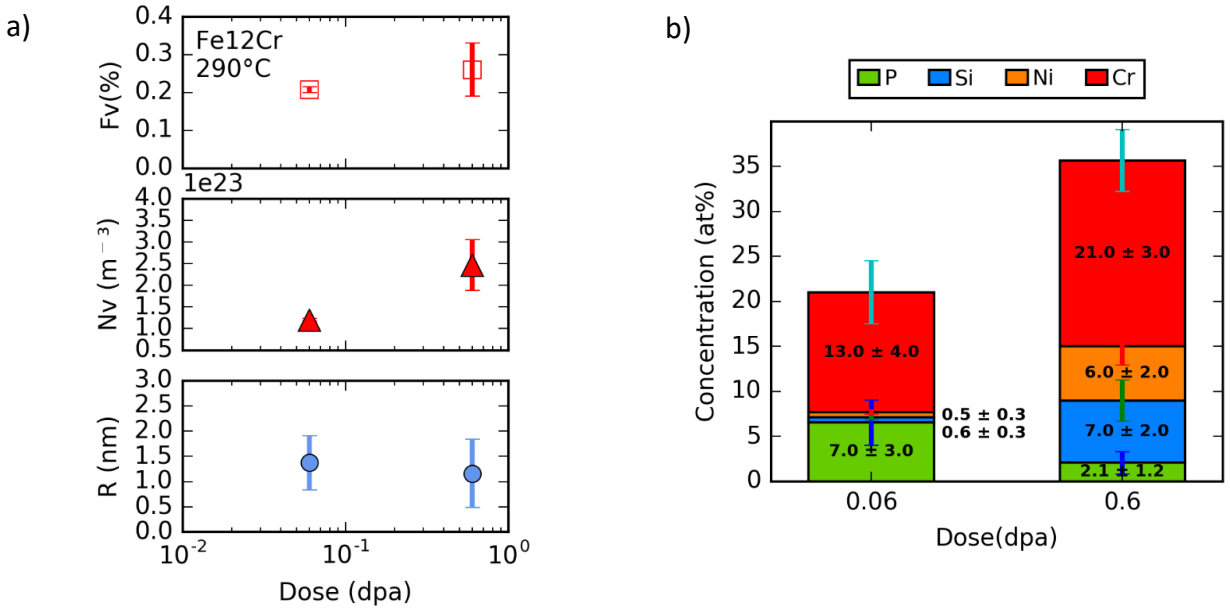

Figure 29: Cluster characteristics of Fe12Cr(Mart.) neutron-irradiated at 290^{0}C as a function on the dose. a) Fv, Nv and R of the NiSiP-rich clusters, b) Solute concentration of the clusters. Data corresponding to 0.6 dpa come from [44].

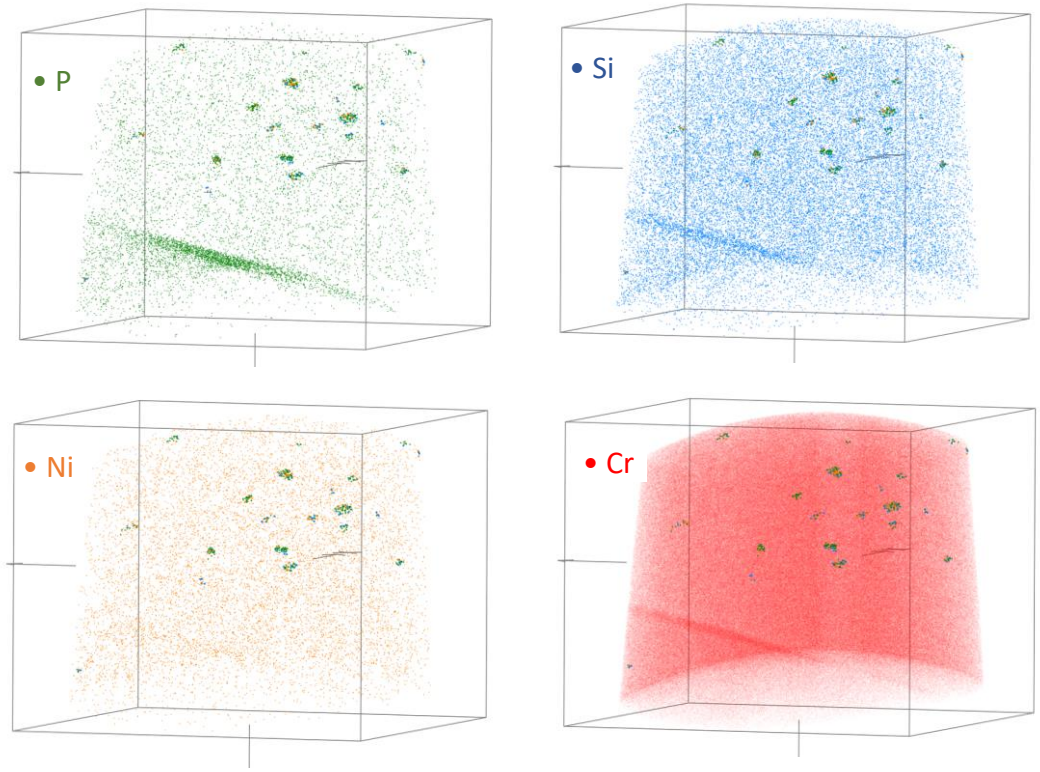

Figure 30: Solute distribution of a Fe12Cr(Mart.) tip irradiated at 300°C up to 0.06 dpa. Different solutes are highlited in a volume of 97x95x79 nm. Si, P and Cr distributions reveal the presence of a GB. SRCs are highligted in all images.

5 Results on electron irradiated alloys [47].

5.1.1 APT

A high purity Fe14Cr_HR (Fe-15at.%Cr) alloy was irradiated-with 1 MeV electrons at 573K.

Figure 31 presents the 3D distributions of Cr atoms to doses of 0.012, 0.023, 0.2 and 0.7 dpa at 300°C. A very high number density of Cr-enriched particles are clearly observable since the earliest dose. Characterization of the particle radius, number density, volume fraction and composition together with the Cr content within the matrix are given in Table 16. The evolution corresponding to these figures as a function of dose are plotted in Figure 32 (a), (b), (c), and (d) and Figure 33.

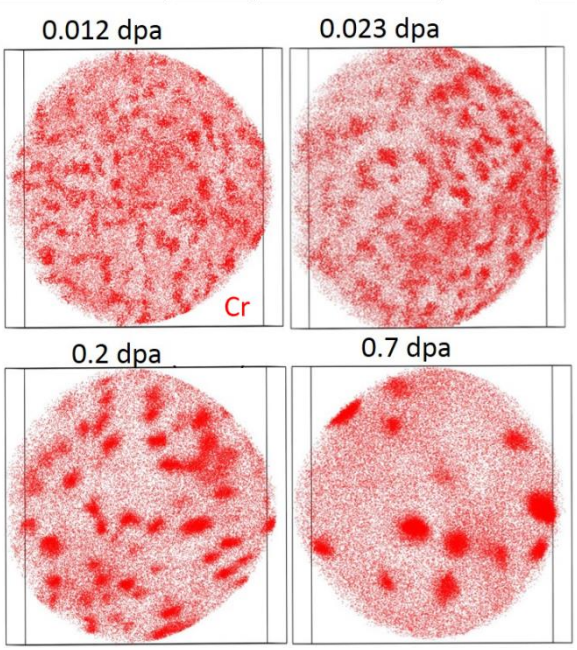

Figure 31: 3D distribution of Cr atoms in the Fe14Cr_HR alloy irradiated at 573K and from 0.012 dpa to 0.7 dpa. Region with at least 24 % of Cr are underlined (V=51 x 51 x 10 nm3 for 0.012, 0.023 and 0.2 dpa; V=48 x 47 x 10 nm3 for 0.7 dpa).

The particle density decreased over the investigated dose range and tends toward the LSW t^{-1} law [48,49] for high doses (Figure 33) and the cubic radius evolves linearly with dose (Figure 32). These results show that coarsening occurred since 0.012 dpa.

Regarding the volume fraction as a function of the dose, after a rapid increase between 0.012 and 0.2 dpa, a slight decrease is observed at 0.7 dpa. As shown in Figure 32 (d) the particle average composition increased from (49±2) at.%Cr to (96±2) at.%Cr after 0.012 and 0.7 dpa. The matrix concentration decreased very rapidly with dose and reached a constant value of 8.7±0.5 at.% after 0.2 dpa.

It should also be mentioned that C contamination was consistently measured in the irradiated samples by APT. This pollution corresponds to a content of 0.1 at.% in average for all doses.

Table 16: Number density, volume fraction, mean radius and composition of the α' particles together with the matrix composition of the electron irradiated Fe-15at.%Cr alloy from dose of 0.012 to 0.7 dpa.

Fe14Cr_HR Dose (dpa)	Matrix composition (at.%Cr)	Density (m^{-3}) x10^{+24}	Volume fraction (%)	Mean radius (nm)	α' composition (at.%Cr)
0.012	12.7 ± 0.3	7.4 ± 0.7	5.5 ± 1	1.16 ± 0.3	49.3 ± 2
0.023	12.0 ± 0.5	6.5 ± 0.7	7.9 ± 1	1.32 ± 0.4	57.9 ± 2
0.2	8.5 ± 0.8	2.4 ± 0.4	9.8 ± 1.3	2.0 ± 0.5	78.2 ± 2
0.7	8.8 ± 0.5	0.5 ± 0.05	6.7 ± 1.3	2.9 ± 0.9	96.0 ± 2

According to the phase diagram proposed by both Xiong et al. [50] and Bonny et al. [51], the Fe14Cr_HR (Fe-15at.%Cr) alloy is supersaturated at 300°C. This supersaturation means that the α – α' decomposition is thermodynamically favourable. As shown by previous irradiation studies [52–54], the α' precipitation arises from a radiation enhanced mechanism due to both supersaturation of Cr in the matrix and the high concentration of point-defects created by irradiation, particularly vacancies.

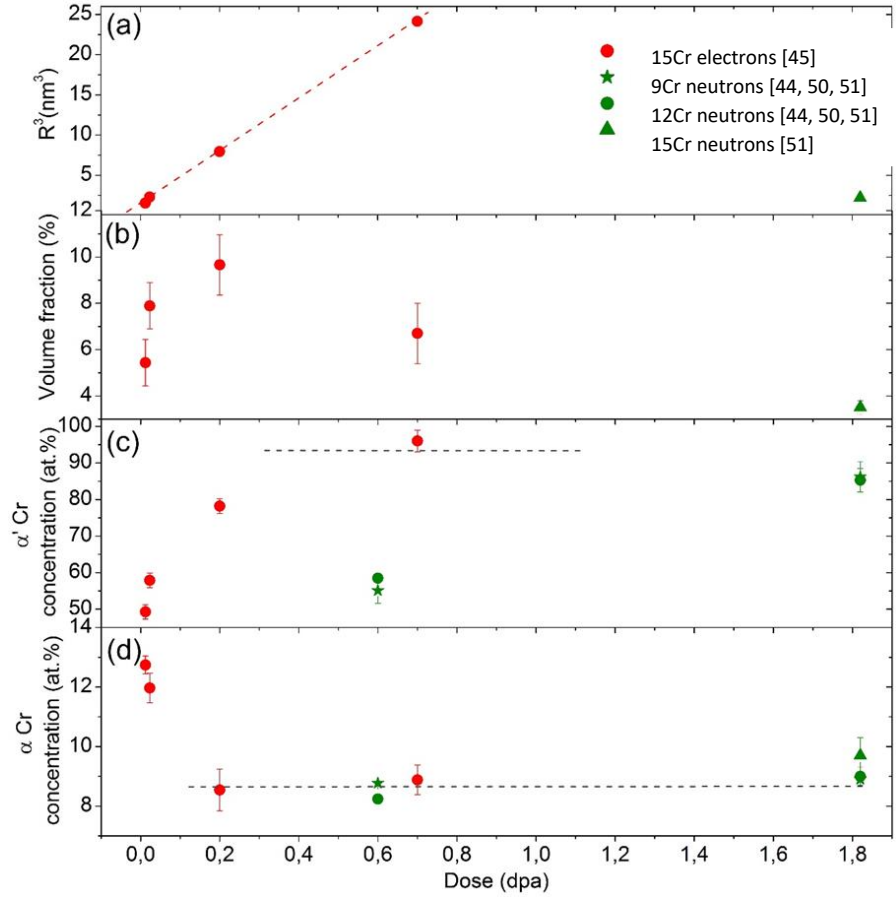

Figure 32 : Evolution of (a) cubic radius, (b) volume fraction, (c) particles Cr concentrations and (d) matrix composition of a Fe-15at.%Cr alloy irradiated with electrons to different dose (red circles)[47]. Values of published data of Fe-15 (1.82dpa) [53], 12 and 9at.%Cr (0.6dpa) [46,52,53]irradiated with neutrons are plotted in green (triangle, square, star). The grey dashed lines correspond to the value expected by the thermodynamics [50].

For comparison, neutron irradiation data of FeCr alloys at the same temperature [41,52,53] were plotted in Figure 32. These alloys contained some impurities which have been shown to be involved in the appearance of NiSiPCr-enriched clusters. Their rather small number density (~10^{23} m^{-3}) is not supposed to significantly affect α' precipitation, though. The Fe15Cr was irradiated up to 1.82 dpa (62 days) [53], the Fe9Cr up to 0.6 dpa (55 days) [52] and the Fe12Cr both to 1.82 and 0.6 dpa [52,53]. Figure 32 (a), (b) and (c) show that the decomposition was greater in the Fe15Cr alloy after electron irradiation doses of 0.7 dpa than after neutron

irradiation of 1.82 dpa. The volume fraction is 6.7% after electron irradiation at the highest dose of 0.7 dpa, whereas a volume fraction of only 3.8% was reached after neutron irradiation at 1.82 dpa [53]. Furthermore, after electron irradiation the volume fraction increases from 5.5% at 0.012 dpa to 9.8% at 0.2 dpa and then decreases to reach 6.7% at 0.6 dpa. This unexpected behaviour can be explained by considering the early precipitation of all available Cr in the alloy up to 0.2 dpa, without reaching the α' equilibrium composition. After 0.2 dpa, precipitate coarsening may be related to the Cr content increase with dose, without decreasing the matrix composition that already reached its equilibrium value.

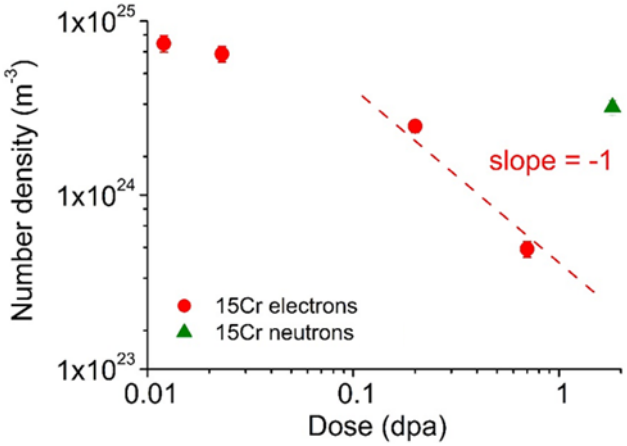

Figure 33 : Evolution of number density of a Fe-15at.%Cr alloy irradiated with electrons to different dose (red circles) [47] . Published data for Fe-15at.%Cr (1.82dpa) [53] irradiated with neutrons is given as green triangle. The dashed line represent the t^{-1} law predicted by the LSW theory [48,49] for long ageing time.

Furthermore, Figure 32 (c) shows that there is an increase in the Cr content of the particles since the earliest dose. As the Cr content is lower when the particles are smaller, one could argue that there is a dilution of the small particles due to local magnification effect (atom probe artefact) [55,56] (Fe atoms from the matrix could enter the particle composition). Nevertheless, it is worth noting that α' particles observed at 1.82 dpa under neutron irradiation and containing about 87at.%Cr [53] have a radius of 1.2 – 1.3 nm while particles of the same size contain ≈ 60at.%Cr at 0.6 dpa under neutron irradiation [52] and at 0.012 and 0.023 dpa under electron irradiation (Figure 32 (c)). This strongly suggests that the evolution of the Cr content within the particles is a kinetics effect and not an APT artefact, as already suggested by Novy et al. [57].

As shown in Figure 32 (c), the equilibrium composition of the α' phase as predicted by Xiong [50] is reached at 0.7 dpa under electron irradiation (96±2 at.%Cr) but not at 1.82 dpa under neutron irradiation. This supports the further decomposition under electron irradiation. It is the first direct measurement of the equilibrium composition of α' phase at 300°C by APT that validates the predicted value of Xiong et al. [50].

The Cr solubility limit measured after electron irradiation, (8.7±0.5) at.%Cr, is in very good agreement with the value obtained based on neutron irradiation data. This value is consistent with the FeCr phase diagram proposed by Xiong *et al.* [50] and Bonny *et al.* [51], which both predict a solubility limit of ≈9at.% at 573K. These results suggest that the solubility limit is not modified by neutron and electron irradiation. Note that the solubility limit is not reached in the Fe15Cr alloy irradiated with neutron at 1.82 dpa, supporting the idea of slower kinetics of decomposition under neutron irradiation. This is not surprising as it is well known that 1 MeV electron irradiation is very efficient at accelerating atomic diffusion, since all defects are created as isolated point defects. Conversely, the efficiency of neutrons for producing freely migrating defects is only of a few percent [58,59]. Moreover, because point defects clusters are created in the displacement cascades under neutron irradiation, the sink density for point defects is much larger under neutron irradiation. These two differences point in the same direction: the fraction of isolated points defects is much lower under neutron irradiation for a given dpa value. Another point that might influence the kinetics is the initial microstructure of the alloys. Nevertheless, if in the Fe9Cr and Fe12Cr the microstructure is martensitic [8-13], the Fe-15at.%Cr [12], is ferritic as in the present study. So this cannot explain the difference.

5.1.2 TEM

The defect microstructure in terms of dislocation loops in the electron irradiated specimens of high purity Fe-15%Cr alloy was characterized using a JEOL 2100 Transmission Electron Microscope (TEM) operating at 200kV and equipped with a LaB_6 electron source. TEM investigations performed on samples irradiated to 0.023 and 0.2 dpa revealed the presence of dislocations loops (Figure 34). The thickness of the analysed area was determined using thickness fringes. The number density, loop mean size and foil thickness are reported in Table 17. The average loop size and number density increased with the dose. Determination of the nature of the dislocation loops showed that 100% were of <100> type. Images in Figure 34 show that at 0.2 dpa, the loops are no more randomly distributed. They are aligned along the <100> directions.

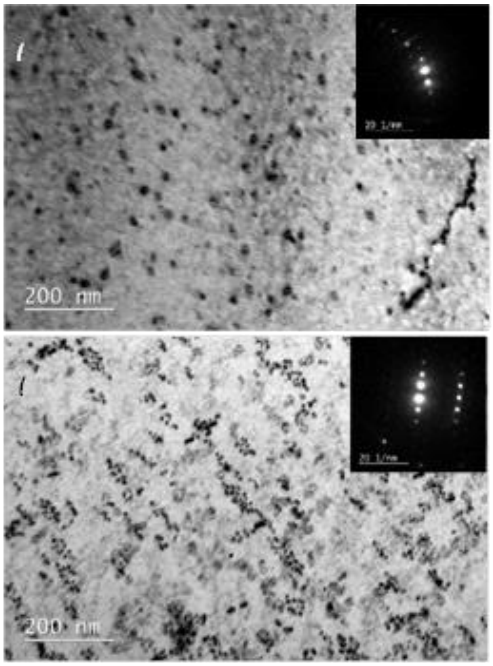

Figure 34: TEM observation of the loop microstructure in a Fe-15at.%Cr after electron irradiation at (a) 0.023 dpa and (b) 0.2 dpa. Bright field imaging, g=[110] near a zone axis (111).

Table 17: Dislocation loops characteristics.

Dose	Foil thickness (nm)	Density (m^{-3})	Mean diameter (nm)
0.023	220	(1.8 ± 0.6) $x10^{+21}$	11 ± 3
0.2	202	(6.6 ± 2.2) $x10^{+21}$	13 ± 3.5

6 Results on ion irradiated alloys

List of materials, irradiation conditions and characterisation techniques applied are provided in Table 18.

Table 18: Summary of post-ion-irradiation characterisations performed within the project. The dose is given at 500 nm depth when not specified.

	Unirradiated	0.1 dpa – 300°C	0.5 dpa 300°C	0.5dpa 450°C	0.5 dpa 200°C
Fe	PAS		PAS, TEM	PAS	PAS
Fe9Cr	PAS, NI	PAS, NI	PAS, NI, TEM	PAS, NI	PAS, NI
Fe9Cr-MIRE	PAS, NI, APT		PAS, NI, APT, TEM	PAS, NI	PAS, NI
Fe9CrNiSiP	PAS, NI, APT	PAS, NI	PAS, NI, APT, TEM	PAS, NI	PAS, NI
Fe9CrSi, Fe9CrP, Fe9CrNi	PAS	PAS			
Fe14Cr	PAS	PAS			
Fe14CrNiSiP	PAS, NI, APT	PAS, APT	PAS, NI, APT, TEM	PAS, NI	PAS
Fe14CrSi, Fe14CrP, Fe14CrNi	PAS, NI, APT	PAS, NI, APT			
Fe5CrNiSiP	PAS, NI, APT		PAS, NI, APT	PAS, NI	PAS
Fe15Cr*	APT		APT		

* target dose of 0.6 at 200 nm.

6.1.1 Mechanical characterisation: Nano-indentation (NI)

The indentation hardness was measured as a function of contact depth for a selected set of alloys and ion irradiation conditions, including the respective unirradiated reference samples. In Figure 35, the indentation hardness of Fe9Cr-NiSiP is shown as a function of contact depth in unirradiated condition and after irradiation with 5 MeV Fe ions at 200°C, 300°C and 450°C to a nominal dose of 0.5 dpa at a depth of 500 nm by way of an example representative for the whole set of measurements. For the unirradiated samples the indentation hardness shows the typical indentation size effect, i.e. the measured hardness increases with decreasing contact depth, except for depth below about 100 nm where artefacts related to tip rounding and/or surface preparation cannot be neglected.

For the ion-irradiated samples a higher indentation hardness with a distinct maximum at about 200 nm contact depth is observed, which is related to the irradiation-induced hardening of the ion irradiated layer. The decrease of indentation hardness with increasing contact depth beyond the maximum is dominated by the increasing contribution of the softer unirradiated substrate. The decrease of the indentation hardness with decreasing contact depth for depths smaller than about 200 nm is attributed to the graded dpa-profile.

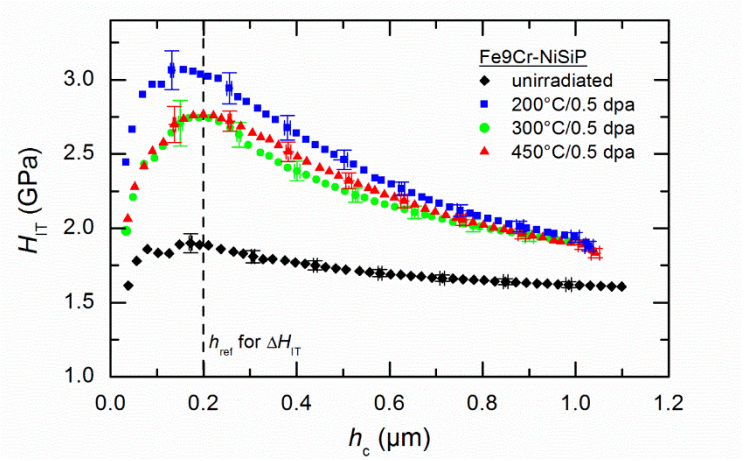

Figure 35: Indentation hardness of Fe9Cr-NiSiP as a function of contact depth in unirradiated condition and after irradiation with 5 MeV Fe ions at 200°C, 300°C and 450°C to 0.5 nominal dpa @ 500 nm, as example.

In the following only the irradiation induced hardness change with respect to the unirradiated reference is considered. A reference depth of 200 nm was selected to calculate the hardness difference, which is close to the maximum indentation hardness for most irradiated conditions and ensures negligible substrate effect.

The irradiation-induced hardening observed for the FeCr-NiSiP alloys after irradiation at 300°C and 450°C up to 0.5 dpa is shown in Figure 36 as a function of the Cr content. Hardening is significant for all alloys and at both temperatures. The highest hardening is observed for Fe5Cr-NiSiP at both temperatures. The hardening of Fe9Cr-NiSiP and Fe14Cr-NiSiP is similar. There is no distinct minimum of hardening at 9%Cr.

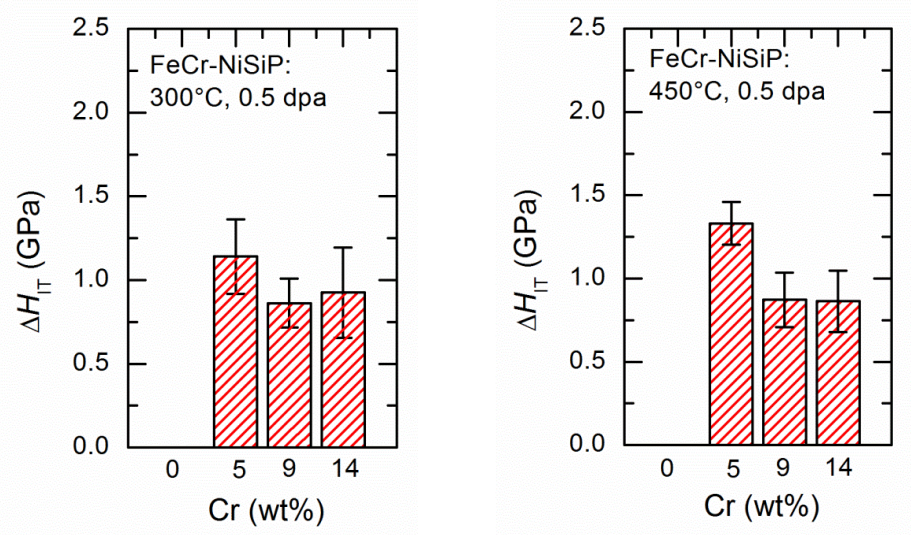

Figure 36: Ion-irradiation induced hardening in FeCr-NiSiP after irradiation with 5 MeV Fe ions at 300°C (left) and 450°C (right), respectively, to a nominal dose of 0.5 dpa at a depth of 500 nm.

The results indicate that α'-phase mediated hardening is not the dominant hardening contribution. The hardening is rather dominated by NiSiP(Cr)-clusters. Their contribution is expected to be similar for all NiSiP bearing alloys.

In Figure 37 the irradiation-induced hardening observed for the Fe9Cr alloys at 200-450°C is plotted against the sum of their Ni, Si and P contents. Again significant hardening is observed at all temperatures. There is a decreasing trend of hardening with increasing temperature. The results confirm that the presence of Ni, Si and P has a strong impact on the irradiation response in terms of enhancing irradiation-induced hardening. In the NiSiP-bearing alloys the hardening contribution related to NiSiP either directly by means of NiSiP clusters or indirectly by their effect on nucleation and growth of dislocation loops dominates hardening for the Ni, Si and P contents studied here. The effect is present at all investigated temperatures. No obvious effect of ferritic or martensitic microstructure is seen.

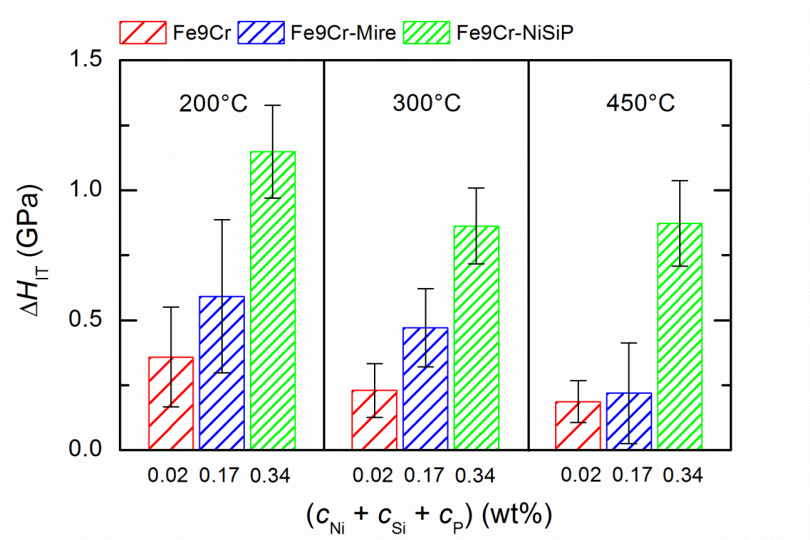

Figure 37: Ion-irradiation induced hardening in Fe9Cr with different NiSiP contents after irradiation with 5 MeV Fe ions at 200°C, 300°C and 450°C, respectively, to a nominal dose of 0.5 dpa at a depth of 500 nm

The dependence of irradiation induced hardening on the damage level in terms of dpa is summarized in Figure 38.

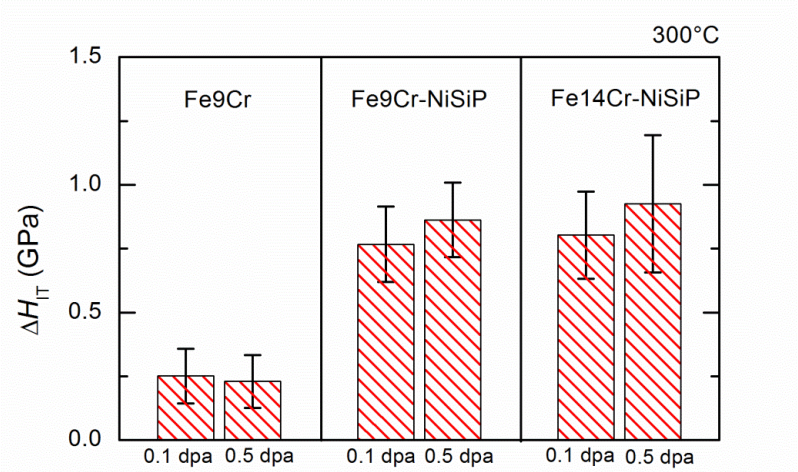

Figure 38: Ion-irradiation induced hardening in Fe-9Cr, Fe-9Cr-NiSiP and Fe-14Cr-NiSiP after irradiation with 5 MeV Fe ions 300°C to a nominal dose of 0.1 dpa and 0.5 dpa, respectively, at a depth of 500 nm

An increase in dpa of a factor 5 does not lead to a further increase of hardening compared to 0.1 dpa. This indicates a saturation of hardening. It cannot be excluded that this saturation is intermediate and the hardening further increases at higher dpa as a consequence of changes in the dominant hardening features (if any).

6.1.2 PAS

6.1.2.1 HZDR Contribution

Depth-resolved Doppler Broadening PAS

Effect of irradiation temperature and Cr content

Samples of pure Fe, Fe5Cr-NiSiP and Fe14Cr-NiSiP irradiated with 5 MeV Fe^+ ions at 200°C, 300°C and 450°C to a nominal displacement damage of 0.5 dpa at a depth of 500 nm were analysed by means of depth-resolved Doppler broadening positron annihilation spectroscopy with positron energies in the range of 27 eV

to 35 keV. Unirradiated samples of the same alloys were included to serve as reference. The S and W parameters extracted from the Doppler broadening spectra are plotted in Figure 39 as functions of the positron energy.

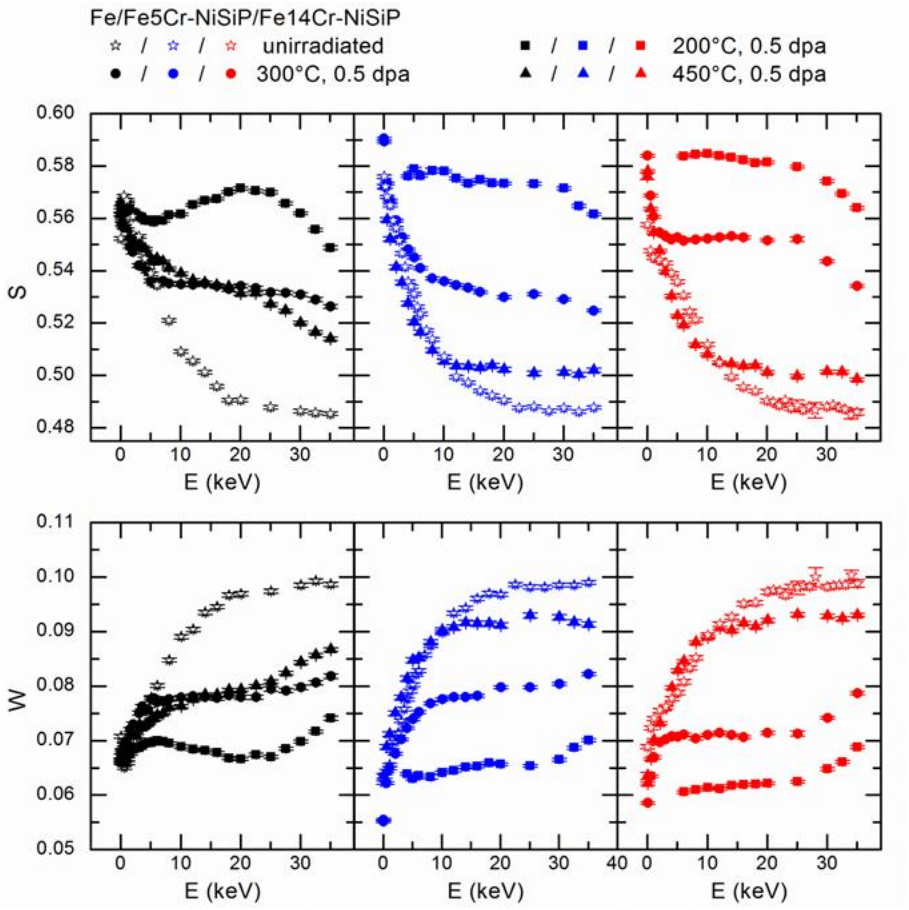

Figure 39: S and W parameter as a function of positron energy for pure Fe, Fe5Cr-NiSiP and Fe14Cr-NiSiP irradiated up to a nominal exposure of 0.5 dpa at 200°C, 300°C and 450°C.

The S and W plots obtained for the unirradiated samples exhibit a similar behaviour for all alloys including pure Fe. They are characterized by a rapid decrease of the S parameter / increase of W parameter with increasing positron energy which is related to the decreasing fraction of positrons annihilating at the sample surface. At high positron energies (> about 20 keV) a plateau representative for the bulk material is reached.

The S and W plots of the Fe-Cr alloys, i.e. Fe5Cr-NiSiP and Fe14Cr-NiSiP, ion-irradiated at 200°C and 300°C exhibit a similar behaviour. The S parameter decreases / the W parameter increases rapidly with increasing positron energy until an intermediate plateau is reached which is related to the formation of vacancy-type defects in the irradiated surface layer. S further decreases / W further increases beyond the plateau for positron energies larger than about 25 keV (see Figure 39) where an increasing fraction of the positrons annihilates in the unirradiated bulk of the sample. The S and W plot of the FeCr alloys irradiated at 450°C do not exhibit such a distinct plateau. Here, the curve shape is similar to the one obtained for the unirradiated material.

The S parameter representing the intermediate plateau observed for the Fe-Cr alloys decreases with increasing irradiation temperature in the Fe-Cr alloys. This indicates a decrease in number density and/or size of defects. Moreover, the S parameter representing the intermediate plateau increases with Cr content at 200°C and 300°C. No significant effect of Cr on the defect density is observed at 450°C.

Except for the irradiation at 300°C, pure Fe shows a different behaviour from the FeCr alloys in terms of the shape of the S and W plots. Similarly to the Fe-Cr alloys, the highest S parameter is observed at 200°C. However, the shape of the S parameter curve exhibits a distinct maximum and resembles the dpa-profile. In contrast, the S parameter measured in Fe irradiated at 450°C to 0.5 dpa decreases monotonously with increasing positron energy, neither peak nor clear plateau are observed. Moreover, at low depth the defect density observed after Fe irradiation at 450°C is higher than the S parameter after irradiation at 300°C. This may be an indication that at 450°C the effect of defect formation during irradiation is superimposed by an effect

of annealing of pre-existing defects leading to an increase in positron diffusion length, as indicated by the flatter slope of the curve at low energies with respect to the unirradiated sample.

The S and W plots measured for Fe and Fe14Cr-NiSiP after ion-irradiation at 300°C to a displacement damage of only 0.1 dpa at a depth of 500 nm resemble the S and W plots for the respective 300°C/0.5 dpa-irradiations in terms of the curve shape exhibiting an intermediate plateau (Figure 41). The S parameter representative for the intermediate plateau is higher for 0.1 dpa than for 0.5 dpa (Figure 40).

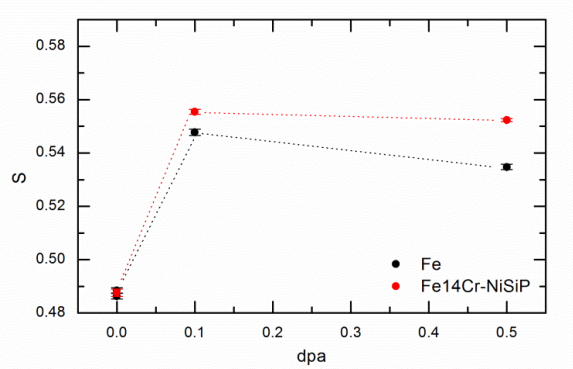

Figure 40 (top): S and W parameter as a function of positron energy for pure Fe in unirradiated condition and ion irradiated at 300°C up to a nominal exposure of 0.1 dpa and 0.5 dpa

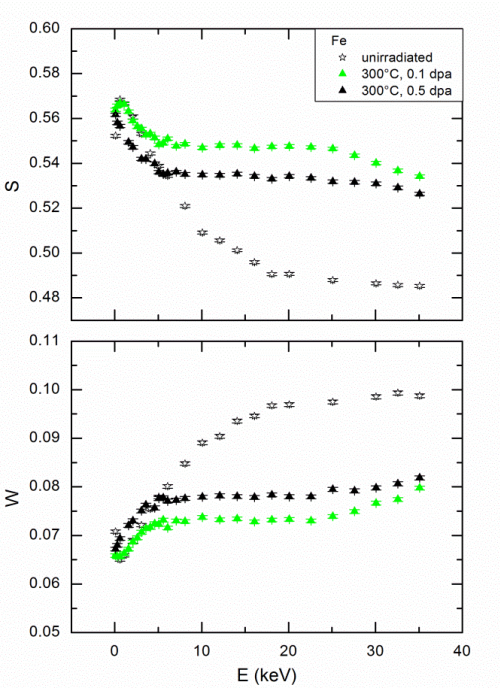

Figure 41 (left): S parameter as a function of dpa (in terms of nominal exposure at 500 nm depth) for pure Fe and Fe14Cr-NiSiP irradiated with 5 MeV Fe ions at 300°C

In Figure 42 the S parameter is plotted as a function of the W parameter. The plot is based on the S and W values representative for :

- the unirradiated bulk material taken from the plateau observed for the unirradiated samples
- the ion irradiated layer, taken from the intermediate plateau or alternatively the maximum / minimum observed in the S(E) / W(E) curves.

In the S-W plot the (S,W) points follow two straight lines both going through the (S,W) points representing the unirradiated bulk material. This indicates the presence of different annihilation states. For an irradiation temperature of 200°C larger vacancy-type defects are detected then for 300°C and 450°C. The plot also allows interpretation of the differences in the S parameter described above in terms of a change in defect density for alloys and conditions sharing the same straight line. This means:

- higher defect densities are observed in Fe14Cr-NiSiP than in Fe5Cr-NiSiP at 200°C and at 300°C, while there is no significant difference at 450°C,
- defect densities at 300°C are higher than at 450°C in the FeCr alloys,

- defect densities are higher at 0.1 dpa than at 0.5 dpa in Fe and Fe14Cr-NiSiP.

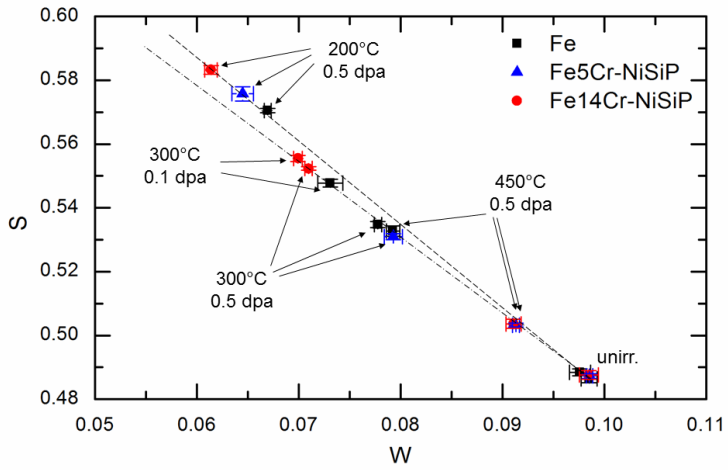

Figure 42: S-W-Plot based on S and W values representative for the bulk (plateau measured for unirradiated samples) and the irradiated layer (intermediated plateau or peak observed in ion-irradiated samples)

Effect of impurities and alloying elements

Samples of Fe14Cr, Fe14Cr-Ni, Fe14Cr-Si, Fe14Cr-P and Fe14Cr-NiSiP irradiated with 5 MeV Fe ions at 300°C to a nominal displacement damage of 0.1 dpa at a depth of 500 nm where analysed by means of depth-resolved Doppler broadening positron annihilation spectroscopy with positron energies in the range of 27 eV to 35 keV. The S and W parameter extracted from the Doppler broadening spectra are plotted in Figure 43 as functions of the positron energy. The unirradiated conditions for Fe14Cr-Ni and Fe14Cr-NiSiP are included to serve as reference.

A difference is observed for alloys containing P and those without P. While the alloys containing P exhibit an intermediate plateau as described in the previous section, the alloys without P exhibit a maximum. Moreover, the latter exhibit a larger irradiation-induced increase of S.

In Figure 44 the (S,W) points measured for a positron energy of 12 keV are plotted along with the straight lines shown in Figure 42. From this Figure it can be tentatively concluded that the effect of P is to suppress or retard the growth of larger vacancy clusters. For the alloys without P addition the highest S parameter (number density of vacancy clusters) is observed for Fe14Cr-Ni followed by Fe14Cr-Si. The addition of both Ni and Si to Fe14Cr-P does not result in an increase of S.

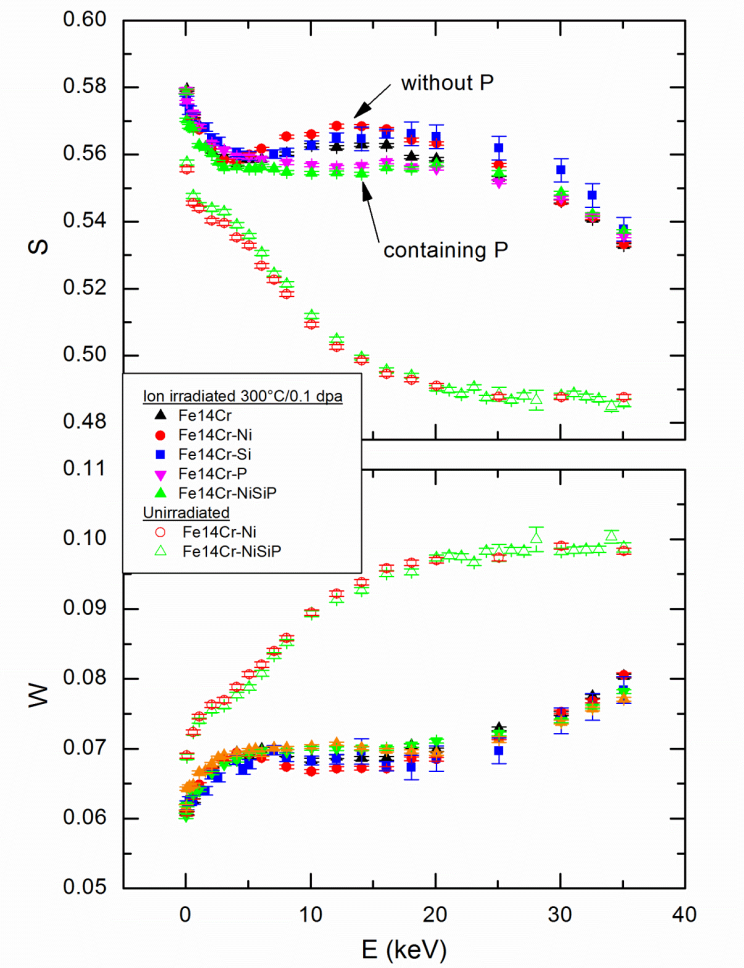

Figure 43: S and W parameter as a function of positron energy for Fe14Cr, Fe14Cr-Ni, Fe14Cr-Si, Fe14Cr-P and Fe14Cr-NiSiP irradiated up to a nominal exposure of 0.1 dpa at 300°C

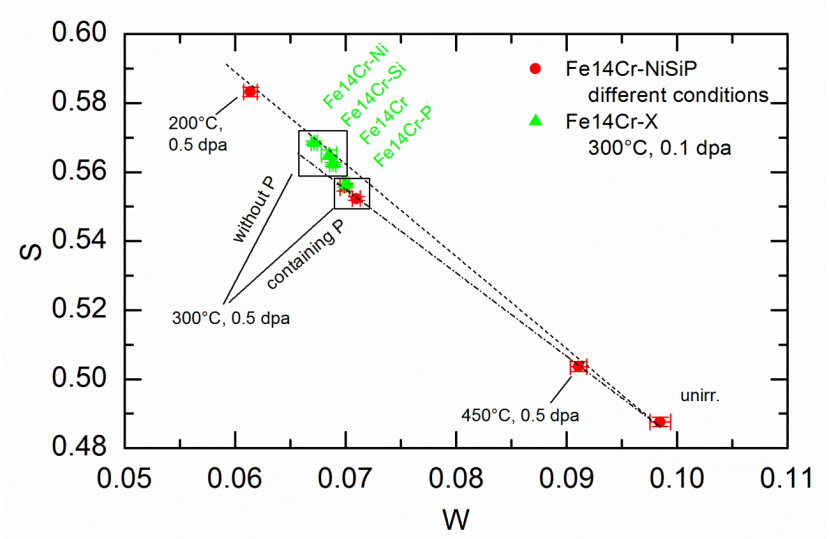

Figure 44: S-W-Plot based on S and W values representative for the bulk and the irradiated layer (300°C, 0.1 dpa), respectively, for the Fe14Cr alloys with different contents of Ni, Si and P, the straight lines are the same as shown in Figure 42

Coincidence Doppler Broadening PAS

Coincidence Doppler broadening (CDB) spectra obtained for selected alloys and conditions and a positron energy of 16 keV are summarized in Figure 42 to Figure 48. Figures are arranged such that they always contain CDB spectra of conditions with similar defects according to the S-W plots presented in Figure 42 and Figure 44. There is no obvious effect of any of the added elements on the shape of the CDB spectra.

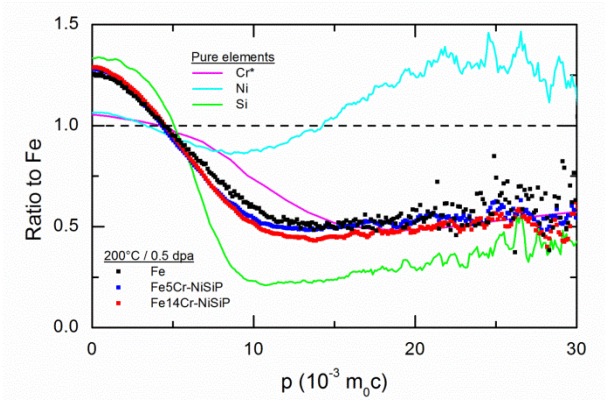

Figure 45: Coincidence Doppler broadening spectra for Fe, Fe5Cr-NiSiP and Fe14Cr-NiSiP irradiated with 5 MeV Fe ions at 200°C to a nominal exposure of 0.5 dpa at 500 nm depth

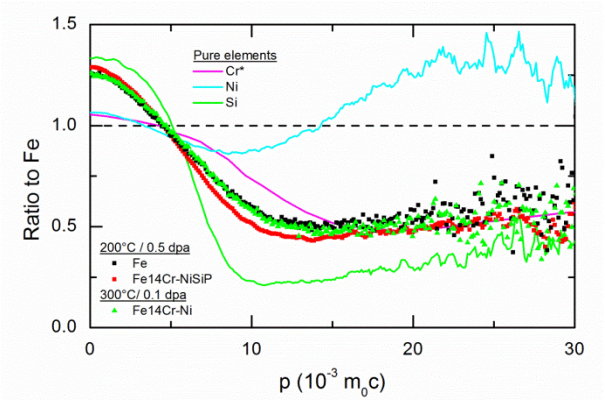

Figure 46 Coincidence Doppler broadening spectra for Fe14Cr-Ni irradiated with 5 MeV Fe ions at 300°C to a nominal exposure of 0.1 dpa at 500 nm depth along with Fe and Fe14Cr-NiSiP irradiated at 200°C to 0.5 dpa

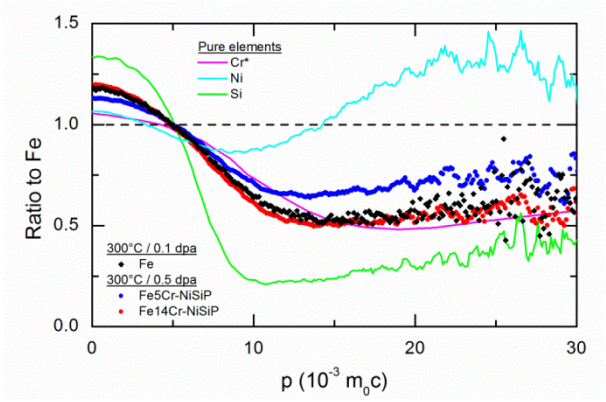

Figure 47: Coincidence Doppler broadening spectra for Fe, Fe5Cr-NiSiP and Fe14Cr-NiSiP irradiated with 5 MeV Fe ions at 300°C to a nominal exposure of 0.1 dpa and 0.5 dpa at 500 nm depth, respectively

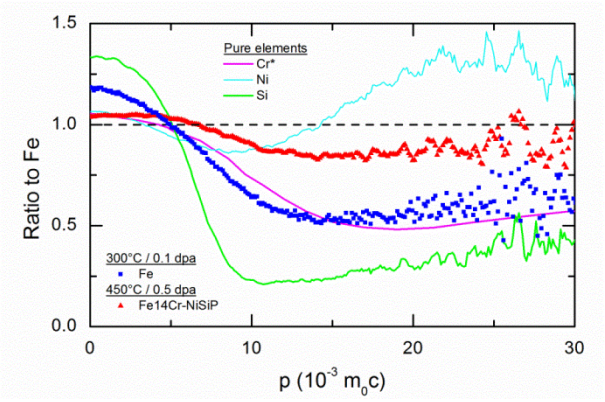

Figure 48: Coincidence Doppler broadening spectra of Fe14Cr-NiSiP irradiated with 5 MeV Fe ions at 450°C to a nominal exposure of 0.5 dpa at 500 nm depth, along with the spectrum for Fe irradiated at 300°C to 0.1 dpa

6.1.2.1 CEMHTI contribution

In addition to the previous work on Fe-5Cr, Fe-14Cr and pure Fe samples, Fe-9Cr samples were characterized by depth-resolved Doppler Broadening positron annihilation spectroscopy in CEMHTI. The sample list is given in Table 18. Samples were irradiated with 5 MeV Fe^+ ions at 200°C, 300°C and 450°C to a nominal displacement damage of 0.1 and 0.5 dpa at a depth of 500 nm. Unirradiated and irradiated samples were analysed with positron energies in the range of 500 eV to 25 keV. Measurement details are given in 2.2.2. It is important to note that the germanium detectors from CEMHTI and HZDR do not have the same resolution. Also, the windows used to calculate S and W parameters are different. Thus, it is not possible to do direct or

quantitative comparisons between S and W values measured on both positron accelerators. The comparisons can only be qualitative.

Unirradiated samples:

As-received samples were measured in order to check that the sample preparation (mechanical polishing and electropolishing) does not introduce defects in the first micron of the samples. The Figure 49 shows the evolution of S and W parameters as functions of the positron energy (E) and the S-W plot for all the different Fe-9%Cr samples. The curves are compared to the one of a defect-free pure Fe sample annealed in high vacuum at 750°C [60].

The S(E) curves show two different behaviours. A first set of samples, composed of Fe9CrNiSiP, Fe-9CrNi and Fe-9Cr Matisse samples has a behaviour close to the pure Fe one. The curves decrease regularly with the positron energy and the three samples reach the same S and W values as defect-free Fe sample at high positron energies. For each sample, the points on the S-W plots are located on one segment. Only two annihilation states are present in these samples: the surface and the bulk state. The bulk state is very close to the pure iron one indicating that these three samples are almost defect-free.

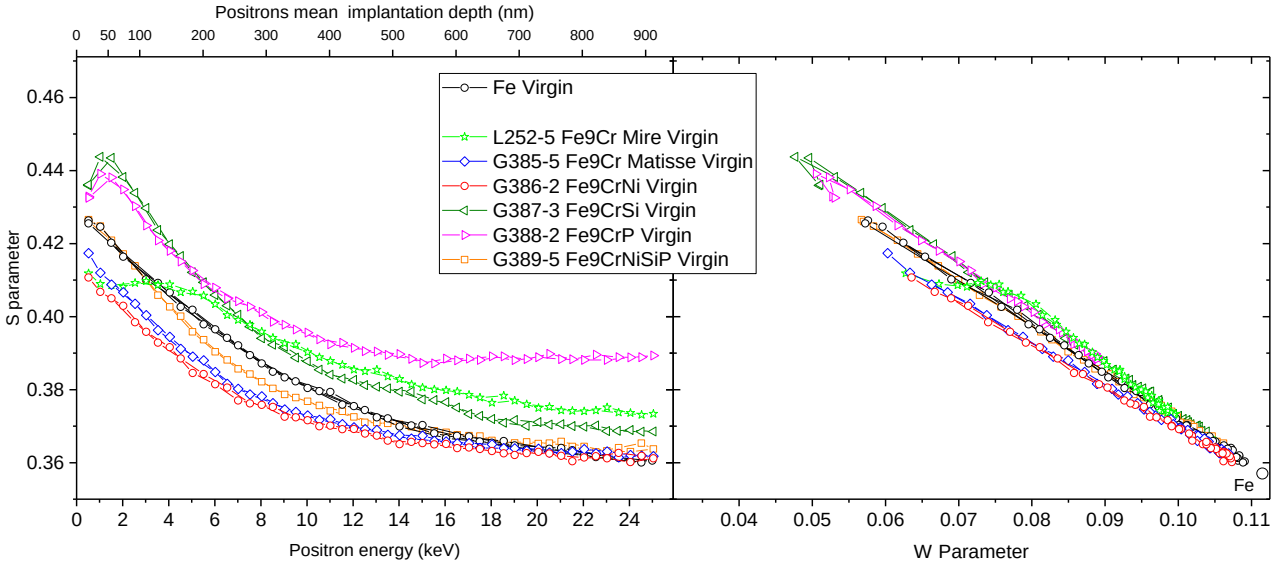

Figure 49 : S and W parameter as a function of positron energy and S-W Plot for unirradiated Fe-9Cr samples and a Fe virgin sample.

The second set of samples is composed of Fe-9Cr Mire, Fe-9CrSi and Fe-9CrP samples and does not follow the pure-Fe behaviour. The S values increase in Fe-9CrSi and Fe-9CrP samples between 0.5 and 2 keV and are stable between 0.5 and 6 keV in Fe-9Cr Mire sample. Then, the S values decrease regularly with the positron energy to get closer to the S values of the defect-free Fe sample. The points on the S-W plots follow different segments showing that more than two annihilation states are present in these samples. Vacancy-type defects or oxidation are present at the close surface of these samples but Fe-9Cr Mire and Fe-9CrSi samples reach S-W values close to defect-free Fe at high positron energies (i.e. in the bulk). In the case of the Fe-9CrP sample, S values remain high at high positron energies indicating that defects are present in the bulk most probably dislocations as mentioned in 4.1.2.

The study of the as-received state shows that most of the samples are almost defect-free in the bulk. The surface preparation can introduce some defects in the near surface region (<100nm) but high positron energies can be used to get the bulk values. Some defects are present in the virgin Fe-9CrP sample and should be taken into account in the analysis of the irradiated sample.

For the ion-irradiation studies we have extracted S and W average values from plateaus of the S(E) and W(E) curves in the positron energy range of [15-25] keV. These values are divided respectively by the S and W value of a defect-free iron (S_{Fe}= 0.357; W_{Fe} = 0.111) to see the variation of the S and W parameter between

different samples. The two characteristic lines found for monovacancies (V_{Fe}), vacancy-clusters (V_n) [61] and dislocations (D_{Fe}) in pure Fe are also reported to see qualitatively the proportion of different defects.

Effect of the temperature:

Samples of Fe-9CrNiSiP, Fe-9Cr Mire and Fe-9Cr Matisse were irradiated with 5 MeV Fe^+ ions at 0.5 dpa at 200°C, 300°C and 450°C. The characteristic points representative of the bulk in the irradiated samples were extracted from S(E) and W(E) curves and results are presented in the Figure 50 on a S-W plot.

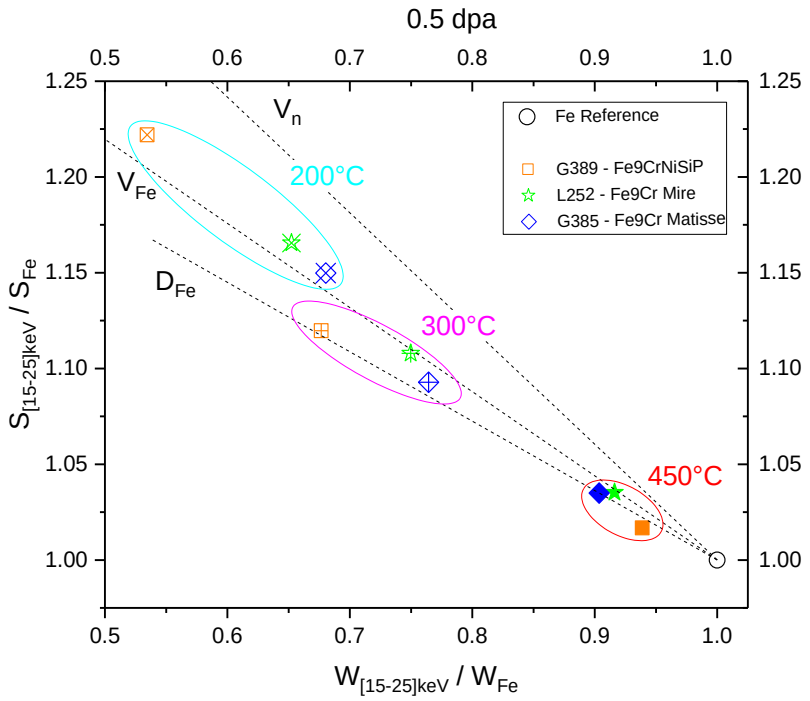

Figure 50 : S-W plot of Fe-9CrNiSiP, Fe-9Cr Mire and Fe-9Cr Matisse samples irradiated at 0.5 dpa at 200°C, 300°C and 450°C.

Three groups of points are distributed as a function of the ion irradiation temperature. At 200°C, the three samples have the highest S values and lowest W values. The S-W points are located between the lines of the monvacancy and the vacancy-clusters of pure Fe. The presence of these two defects is also detected by PALS in neutron-irradiated samples 4.1.2.2. At 300°C, S values have decreased and W values increased for both samples. This behaviour is also observed in Fe-5Cr and Fe-14Cr samples. S-W points are located between the pure Fe monovacancy line and the dislocation line. It is clear that the distribution of defects has changed compared to 200°C. At 300°C, vacancy-type defects are less stable than dislocations. Most probably, the concentration of vacancy-type defects have decreased at 300°C while the dislocation density remains stable or increases leading to a decrease of the S values and an increase of the W values.

At 450°C, S-W points are close to the point of the pure-Fe defect free sample. The dispersion of S-W points is the same as the one measured in as-received sample (≈ 3%). At this temperature vacancies and clusters are annealed and only voids/cavities are stable. If they exist in the samples, their concentration is too low to be detected by PAS.

It is interesting to note that at 200°C and 300°C, the defect density in the Fe-9CrNiSiP samples is higher than in the Fe-9Cr Mire samples and the Fe-9Cr Matisse samples have the lowest defect density. According to chemical analysis of Ni, Si and P elements (Table 2), Fe-9CrNiSiP samples have the highest concentration of alloying elements and Fe-9Cr Matisse samples the lowest. Then, the defect density could be correlated to the amount of alloying elements in the samples showing that alloying elements form vacancy-complex defects more stable with the temperature.

Effect of the irradiation dose

Fe-9CrNiSiP and Fe-9Cr Matisse samples were irradiated with 5 MeV Fe ions at 300°C at 0.1 and 0.5 dpa. The characteristic points representative of the bulk in irradiated samples were extracted from S(E) and W(E) curves and results are presented in the

Figure *51* on a S-W plot.

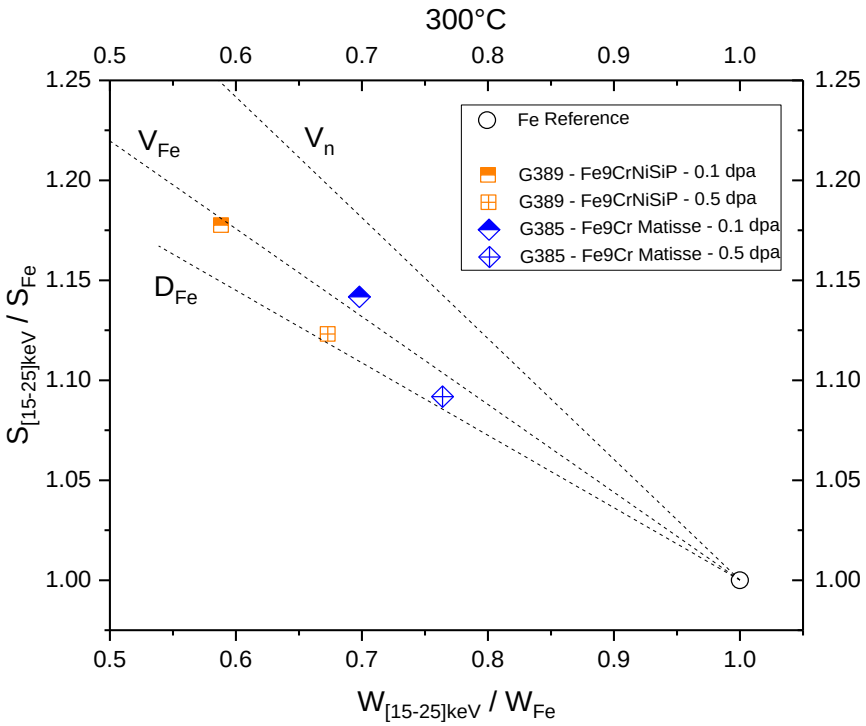

Figure 51 : S-W plot of Fe-9CrNiSiP and Fe-9Cr Matisse model alloy samples irradiated at 300°C at 0.1 and 0.5 dpa

The vacancy defect density is always higher in Fe-9CrNiSiP samples than in Fe-9Cr Matisse samples at both ion-irradiation conditions. As mentioned before, this could be due to the presence of alloying elements in Fe-9CrNiSiP samples that stabilizes defects.

It is observed that the irradiations at 0.1 dpa give higher S values and lower W values in Fe-9Cr samples indicating that the vacancy-type defect density is higher at 0.1 dpa than in 0.5 dpa. The same behaviour is observed in pure Fe and Fe-14Cr samples. In Fe-9Cr samples, the irradiation at 300°C and 0.1 dpa gives results equivalent to the irradiation at 200°C and 0.5 dpa where mainly monovacancies and vacancy clusters are detected. At 0.5 dpa, the distribution of the vacancy-type defects has changed. Most probably the dislocation density has increased, leading to a decrease of the S values and an increase of the W values.

Effect of alloying elements

In order to see the influence of alloying elements, Fe-9Cr Matisse, Fe-9CrNi, Fe-9CrSi, Fe-9CrP and Fe-9CrNiSiP samples were irradiated with 5 MeV Fe ions at 0.1 dpa at 300°C. The characteristic points representative of the bulk in the irradiated samples were extracted from S(E) and W(E) curves and results are presented in the Figure 52 on a S-W plot. The S-W point of the as-received Fe-9CrP sample containing native defects is also plotted. Its S-W point is located close to the dislocation line indicating that dislocations are the main defects present in the sample. In ion irradiated Fe-9CrP sample, the S value increases by 10% and W decreases by 25% and the S-W point is located on the monovacancy line indicating that vacancy defects are now the main defects detected.

In irradiated samples, Fe-9Cr Matisse model alloy has the lowest S value and the highest W value. Other samples have a larger defect density. This confirms that alloying elements or impurities stabilize defects. The

S-W points are distributed in two groups as observed in Fe-14Cr samples. The first group is composed of Fe-9Cr Matisse, Fe-9CrNi and Fe-9CrSi samples. S-W points are located between the lines of the monovacancy and the vacancy-clusters of pure Fe indicating that both defects are the most numerous in these samples. The samples containing Si or Ni give almost the same results. The second group is composed of samples containing phosphorus. Fe-9CrP and Fe-9CrNiSiP samples contain the same amount of P and have almost the same S and W values with respectively the highest and lower values. The S-W points are located on the monovacancy line. These samples have the highest defect density and the monovacancy seems to be the main defect. The presence of P seems to enhance the formation of small vacancy-defects such as monovacancy-phosphorus complexes (V-P). The presence of larger V_n-P complexes cannot be excluded because the effect of phosphorus on the positron-electron pair momentum distribution (i.e. the S and W values) is unknown. Whatever the explanation, it is clear that the phosphorus element plays a role in the early formation of vacancy type defects during irradiation compared to Ni and Si elements.

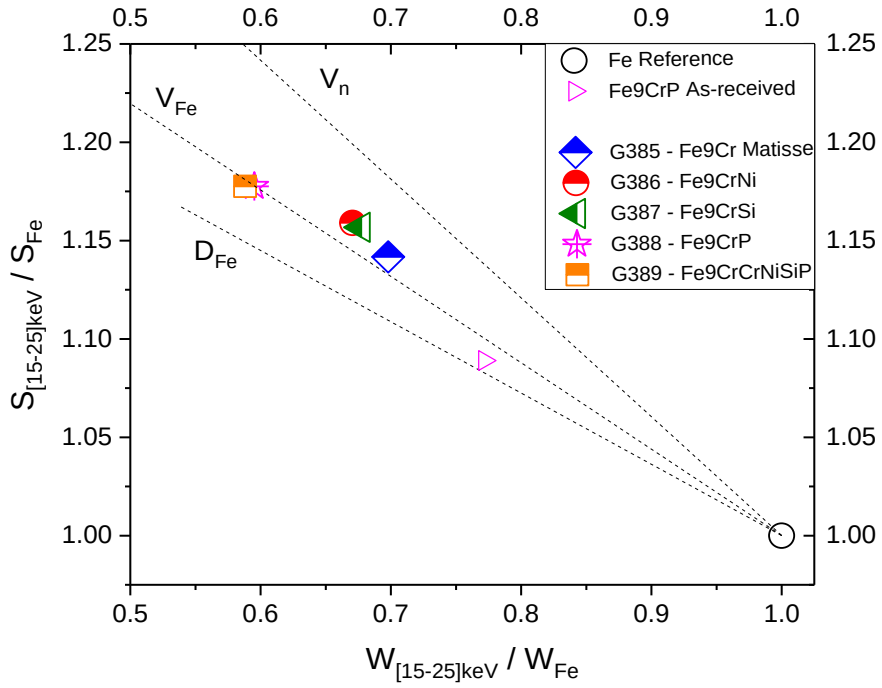

Figure 52: S-W plot of Fe-9Cr Matisse model alloy, Fe-9CrNi, Fe-9CrSi, Fe-9CrP and Fe-9CrNiSiP samples irradiated at 0.1 dpa at 300°C

Conclusion:

Separate effect experiment studies were done using the Fe-9Cr samples set. It was found that the surface preparation of samples is correct. Some defects can be present in the first hundred nanometres, but it is possible to extract data from the bulk using high positron energies. The study on the effect of the irradiation temperature has shown that the vacancy-defects concentration and size decrease between 200°C and 300°C. At 450°C, the concentration of defect is too low to be detected. The same observation was made with the irradiation dose. Between 0.1 and 0.5 dpa, it is found that the vacancy-defects concentration and size decrease while the dislocation concentration increases at an irradiation temperature of 300°C. The effect of the alloying elements/impurities is observed in all studies. Sample containing alloying elements or impurities have higher vacancy-defect concentration compared to the Fe-9Cr model alloy. The comparison of samples containing different alloying elements and irradiated at 0.1 dpa at 300°C has shown that phosphorus element plays a role in the early formation of vacancy type defects compared to Ni and Si elements.

6.1.3 TEM

6.1.3.1 TEM characterisation

Materials and irradiation conditions examined by TEM are summarized in Table 19, where the dose data in dpa is listed, estimated as explained in section 2.1.3.2. Results are listed for materials either with increasing Cr content or increasing Ni+Si+P content.

Table 19: Summary of specimens examined by TEM. Cr and Ni+Si+P content as well as estimated dose. T = 300°C.

Specimen code	Cr (wt%)	Ni+Si+P (wt%)	Estimated dose (dpa)
G379-Fe (3)	0.002	0.011	0.9
G384-Fe5CrNiSiP (1)	4.9	0.349	0.6
G385-Fe9Cr (2)	9.1	0.016	0.2
G385-Fe9Cr (3)	9.1	0.016	0.5
L252-Fe9Cr (2)	8.4	0.170	0.5
G389-Fe9CrNiSiP (1)	9.1	0.336	0.5
G394-Fe14CrNiSiP (1)	14	0.312	0.5

Figure 53 shows the damage profile estimated from SRIM calculations. The added points aim at placing the depth of the region examined by TEM on each alloy.

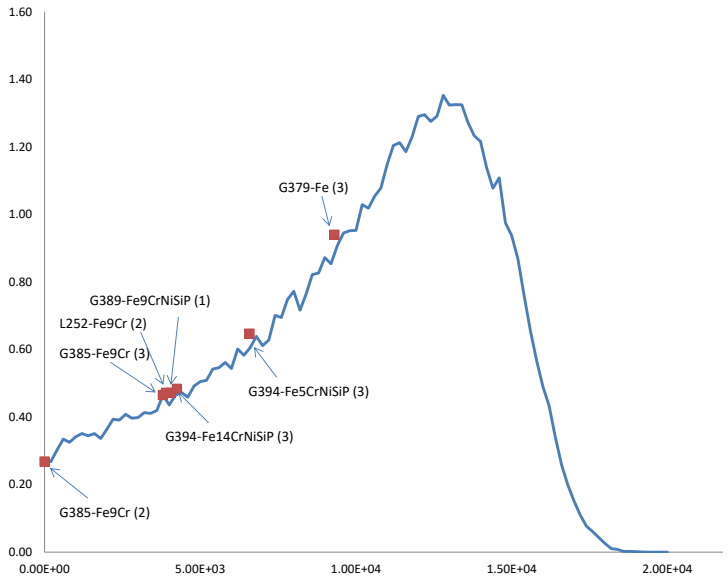

Figure 53: SRIM damage profile. The points denote the depth of the TEM-examined region in each alloy.

Figure 54 shows TEM images of the microstructure of Fe9Cr (F), Fe9Cr (F/M) and Fe9CrNiSiP (F), after ion irradiation at 300ºC and up to 0.5 dpa. The comparison of ion irradiated microstructures of these three alloys allows the effect of both initial microstructure, either, ferritic (F) or ferritic-martensitic (F/M), and presence of impurities such as Ni, Si and P, to be investigated.

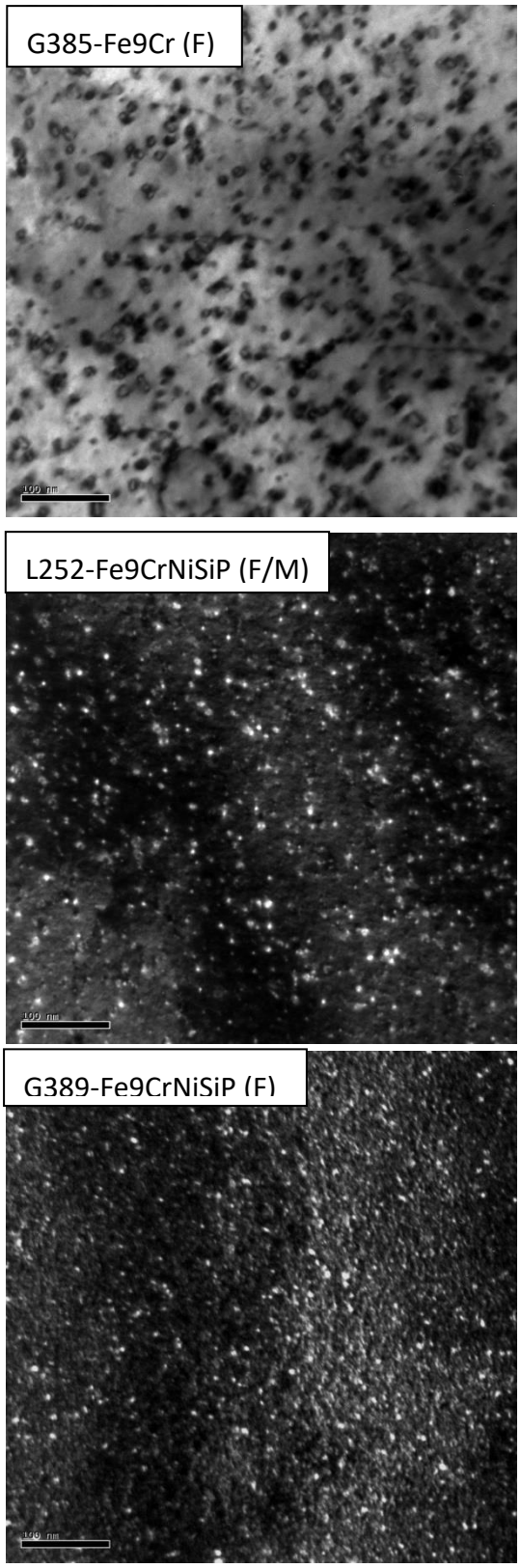

Figure 54: TEM BF and WBDF images of the Fe9Cr(NiSiP) alloys ion irradiated at 300ºC, up to 0.5 dpa. The amount of Ni+Si+P increases from top to bottom.

TEM examination reveals the presence of dislocation loops produced by the ion irradiation. The loops are observed all over the examined region, so their spatial distribution is quite homogeneous. Although some dislocation decoration with loops is observed occasionally, it is not general rule. It is worth pointing out, however, that denuded zones close to grain boundaries have been observed in Fe9Cr (F), as shown in Figure 55. Also, groups of loops forming chains or rafts can be observed.

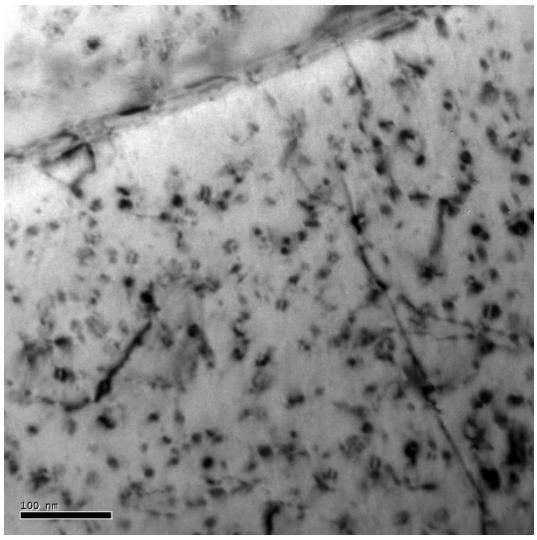

Figure 55: Presence of denuded zones close to grain boundaries in G385-Fe9Cr.

Qualitatively, the size of the loops appears to be larger in Fe9Cr (F) than in the other two Fe9Cr alloys. In Fe9Cr (F/M) and Fe9CrNiSiP (F), loops are smaller in size and appear quite homogeneously distributed all over the examined region. Quantitative information has been obtained from these and similar images. Figure 56 shows the loop size distribution graphs.

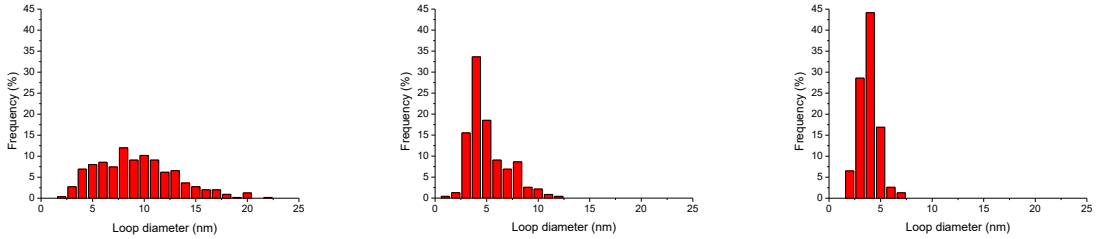

G385-Fe9Cr (F) L252-Fe9Cr (F/M) G389-Fe9Cr NiSiP(F)

Figure 56: Size distribution of dislocation loops observed by TEM and produced by ion irradiation at 300ºC up to 0.5 dpa.

Loop sizes extend from 2 up to 22 nm in the case of Fe9Cr (F). It is worth pointing out that Ni, Si and P contents in this material are the lowest, with Ni+Si+P=0.016 wt%. As the amount of Ni+Si+P increases, the loop size distribution becomes narrower and shifts to smaller sizes. For the Fe9Cr (F/M) the size distribution ranges from about 1 nm up to 12 nm and in the case of Fe9CrNiSiP (F), with the higher amount of Ni+Si+P, the maximum size reached by loops is about 7 nm. Average sizes have been obtained by fitting the size distribution graphs to a LogNormal function and are listed below, in Table 20.

The number of loops has been counted on TEM images, corresponding to different diffraction vectors. Due to the fact that part of the loops will not be visible at certain two-beam conditions, it is necessary to have first an estimation of the proportion of loops with each Burgers vector. To do so, we have followed the statistical **g□b** analysis method described in [62] and applied, for instance, in [63]. It is worth pointing out that, by applying this method, we are assuming the equal probability of all the Burgers vector families.

Table 20: Summary of quantitative data

	G385-Fe9Cr (F)	L252-Fe9Cr (F/M)	G389-Fe9Cr NiSiP(F)
Ni+Si+P (wt%)	0.016	0.170	0.336
BV proportion	<100>: 93% ½<111>: 7%	<100>: 59% ½<111>: 41%	<100>: 38% ½<111>: 62%
½<111>/<100> ratio	0.075	0.695	1.630
Total number density	1.11×10^{22} m^{-3}	1.71×10^{22} m^{-3}	0.9×10^{22} m^{-3}
Mean size, d (nm) Maximum size	(9.6±0.6) nm Max: 22 nm	(4.2±0.1) nm Max: 12 nm	(3.5±0.2) nm Max: 7 nm

The majority of loops are type <100> in Fe9Cr (F). The proportion of <100> loops is quite high taking into account the relatively high Cr content. As reported in literature (see for instance results from in situ irradiation, [63]) the addition of Cr is expected to lead to an increase in <111> proportion compared to irradiated pure Fe. The proportion of <100> decreases for the other two Fe9Cr alloys. The trend of the <111>/<100> ratio correlates better with the increase of alloying or impurities content than with the Cr content: as the amount of Ni+Si+P increases, the <111>/<100> ratio increases. Though there is a big initial microstructure difference, F or F/M, the effect of composition (impurities) on the evolution of the microstructure seems to be predominant and as Ni+Si+P increase, the size of the loops decreases and the proportion of ½<111> loops increases. This fact indicates a prevalent effect of the impurity presence over the effect of Cr content, which is the same for the three alloys, and over the effect of the initial microstructure.

Once the Burgers vector is known, the loop number density has been estimated: no significant differences in density amongst the three alloys is found.

Next Figure 57 shows TEM images of the microstructure after ion irradiation at 300ºC, for Fe, Fe5CrNiSiP, Fe9CrNiSiP and Fe14CrNiSiP. The Fe9CrNiSiP is included here again to compare the microstructure of alloys with increasing Cr content. It is worth pointing out that the dpa level reached at the region examined differs from one material to another.

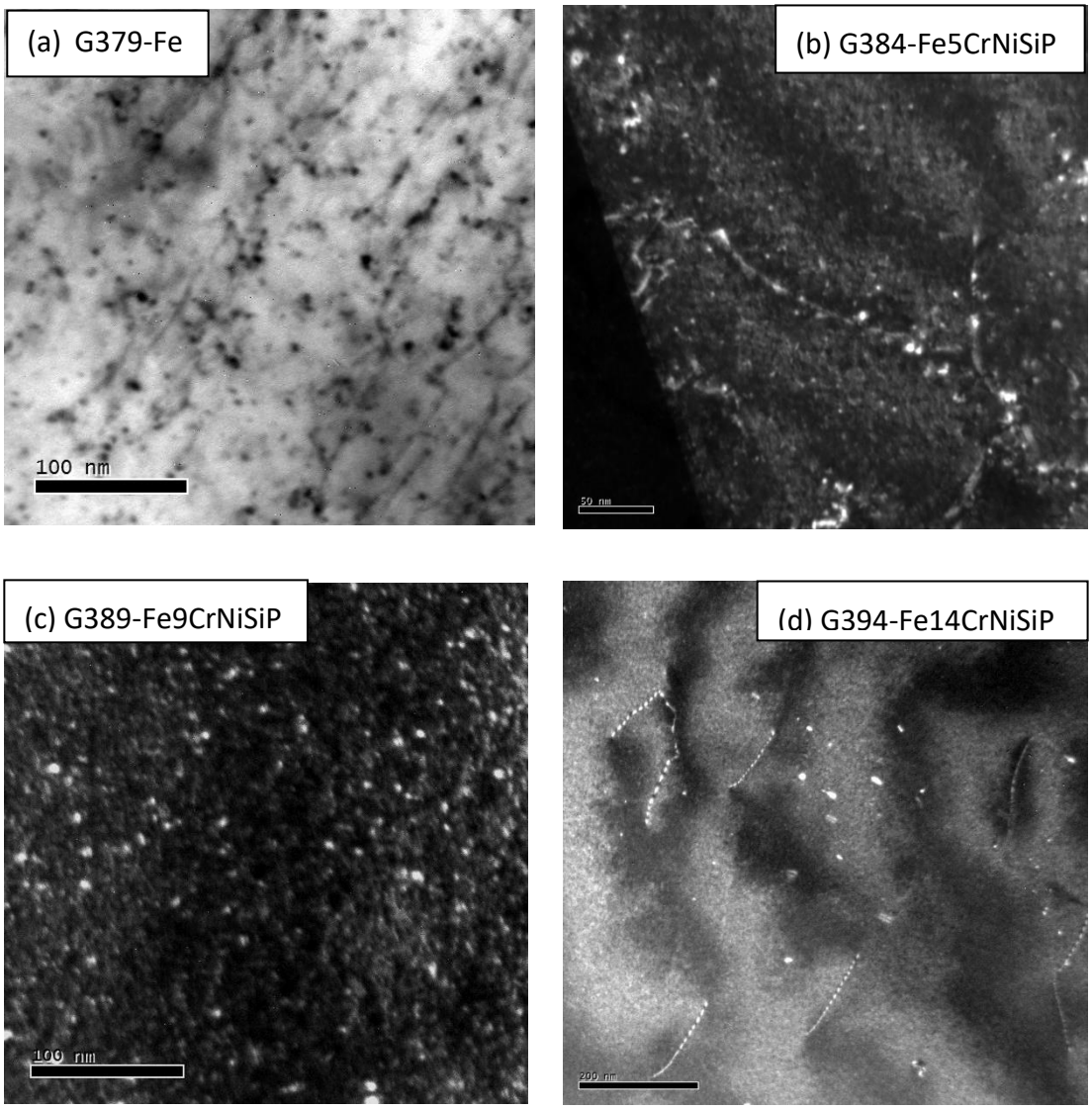

Figure 57: TEM images of ion irradiated materials at 300ºC up to the following estimated doses: (a) 0.9 dpa; (b) 0.6 dpa; (c) 0.5 dpa; and (d) 0.5 dpa. (Note the magnification of Fe14CrNiSiP image is more than twice the magnification of the other three images).

In general, TEM images reveal the presence of dislocation loops in all four materials. In the case of pure Fe, black dots are observed all over the examined region in between a relatively dense dislocation net. Dislocation lines or segments are observed to be aligned all over the region examined by TEM. As shown in Table 19, the region examined has received a higher dose than the other examined materials, however, the loops appear to be smaller than expected for pure Fe in similar irradiation conditions. Further investigations should follow, in order to obtain a specimen from a region at about 500 nm far from the irradiated surface, with estimated dose of 0.5 dpa, including the examination of FIB cross section specimens.

Regarding the Fe5CrNiSiP alloy, small loops are observed that seem to be larger when they appear decorating dislocation lines, but this has not been quantified yet. As explained above, when only Cr is present in the Fe based alloy (Fe9Cr (F)), the ion irradiation produces relatively large loops, while if impurities such as Ni, Si and P are present, the size of the loops is reduced. It is worth noting that the dose received in the examined region is 0.6 dpa.

Finally, the irradiated microstructure of Fe14CrNiSiP shows the presence of very large dislocation loops, reaching about 50 nm. The large loops appear aligned along a preferred direciton and are found in between dislocation segments. The dislocation density of the irradiated specimen is quite high compared to the one of the non irradiated material, it is possible, then, that the observed microstructure is not solely the result of irradiation, but of some level of deformation possibly occurred during specimen preparation. Further work is in progress to examine other specimens, including FIB cross section specimens.

6.1.4 APT

6.1.4.1 2 MeV Fe^{2+} irradiation of a High purity Fe14Cr-HP at 300°C [64]

The effect of the injected ions on α' precipitation has never been addressed up to now. The present work aims at studying this effect and to gain further insight into the mechanisms that could explain the difference in the precipitation kinetics under ion irradiation and the other forms of irradiation (e.g. neutron, proton and electron). Atom Probe Tomography was used to investigate the influence of both damage and injected Fe profiles on α/α' decomposition.

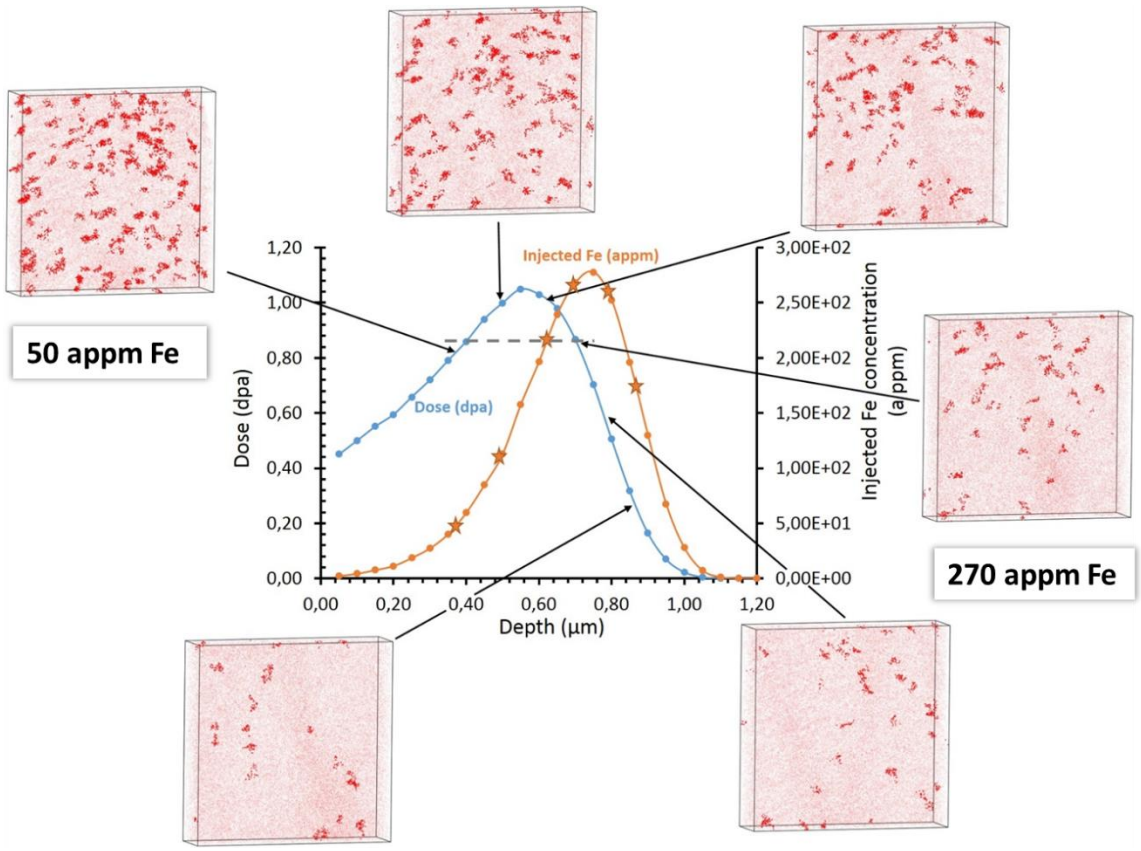

Figure 58 : Damage and implantation profiles calculated with SRIM 2013 [7,8] and the 3D distribution of Cr atoms observed using APT at different depths (i.e. doses). A concentration threshold of X_{Cr}>24at.% was used to highlight α' particles. APT volume V= 40 x 40 x 10 nm^3, α' radius r ≈ 1 nm.

Figure 58 plots both damage and injected Fe concentration profiles obtained under Fe^{2+} ion irradiation (see irradiation conditions in part 2.1.3.2). The 3D distributions of Cr atoms observed with APT from 300 nm to 900 nm in depth are also presented. The first noticeable point is that α' particles formed. To our knowledge, it is the first time that α' precipitation is observed under heavy ion irradiation. This clearly proves that α' particles can be observed under self-ion irradiation with a dose rate of ~10^{-5} dpa/s at 300°C. These results confirm that ballistic dissolution does not occur at this dose rate and irradiation temperature.

The evolution with depth of the particle radius, number density, volume fraction and Cr concentration both in the particles and in the matrix, is given in Figure 59. Figure 58 and Figure 59 together clearly reveal that the evolution of the α' precipitation is depth dependent. As under electron irradiation [47], C contamination during irradiation was measured with APT (between 0.02 and 0.08 at.% as under electron irradiation). C was homogenously distributed but most α' clusters do not include any C atoms. Clearly, the Cr rich particles observed are α' particles, not carbides.

Regarding the evolution of the different characteristics of the α/α' decomposition, the figures are roughly constant up to about 350 nm. From 350 nm on, moving deeper in the irradiated material, α' decomposition becomes less developed. Notably, the maximum decomposition is not observed at the peak damage region (550 nm). It is also worth noting that the two 3D distributions of Cr atoms observed at 400 nm and 700 nm (dashed line on Figure 58) are significantly different whereas they were obtained at the same dose (0.85dpa).

It is a clear evidence of the injected interstitial effect. Undoubtedly, the evolution of α' precipitation deviates significantly from that expected from the damage profile. Figure 59 clearly shows that the depth dependence of α/α' decomposition is correlated with the evolution of the injected Fe concentration rather than the damage profile. This behaviour is similar to that observed in the case of void formation [65–68]. When the contribution of injected Fe becomes more significant, the decomposition decreases.

The origin of this behaviour can be explained as follows. The excess of interstitials due to injected Fe has two major effects: the enhancement of recombination between vacancies and interstitials and the creation of a high density of point defect sinks (interstitial clusters, dislocation loops). Both effects lead to a significant decrease in the concentration of the single point defects which are required for the diffusion of Cr atoms to form α' clusters. Consequently, α' precipitation kinetics is reduced. Investigation and characterization of the influence of injected Fe on the evolution of the matrix damage is on-going.

This work shows that injected Fe reduces α' precipitation. This suggests that α' precipitation should be unlikely to occur if the concentration of injected Fe becomes high. This can explain why α' precipitation was not observed in [27]. In these experiments, a three-step irradiation with 0.5 MeV, 2 MeV and 5 MeV Fe ions was applied to Fe-9at.%Cr and Fe-12at.%Cr alloys in order to obtain a flat damage profile. Nevertheless, the multi-step irradiation does not only flatten the damage profile but also the injected Fe concentration profile. A non-negligible concentration of injected ions was thus introduced over the whole irradiation depth, probably preventing α' precipitation. In addition, a flux effect could also be involved. Indeed, the dose rate used in our work is low for heavy ions irradiation. Such low dose rate might be also necessary for the formation of α' particles. However, the damage rate difference between [27] and the present case is no larger than 5, which is quite small. Its influence is therefore probably not so important.

Also, quite often, microstructural investigations are conducted at peak damage in order to investigate irradiation effects at high doses. However, while the dose is higher in the peak region, so is the concentration of injected ions. Our results show that such investigation of α' precipitation at the damage peak is not appropriate.

In the depth range 90 nm - 350 nm, a plateau is observed whereas the dose rises from 0.5 dpa to 0.8 dpa. The absence of increase in α/α' decomposition in this range might be the signature of the beginning of the influence on the microstructure evolution of the injected Fe ions and their long range diffusion in the concentration gradient. Moreover, the fact that α' particles are observed at 90 nm is not enough to rule out some possible surface effect (efficient loss of point defects at the surface) on the microstructure. Consequently, α' precipitation characteristics observed in the plateau might be biased by surface effect on one hand and injected Fe on the other hand. It is not possible to know whether there exists a region where no artefact due to ion irradiation occurs. Experiments performed with higher ions energies, for instance 5 MeV or 10 MeV, should enable to characterise a region deep enough to avoid surface effects and far enough from the implantation peak to study α' precipitation.

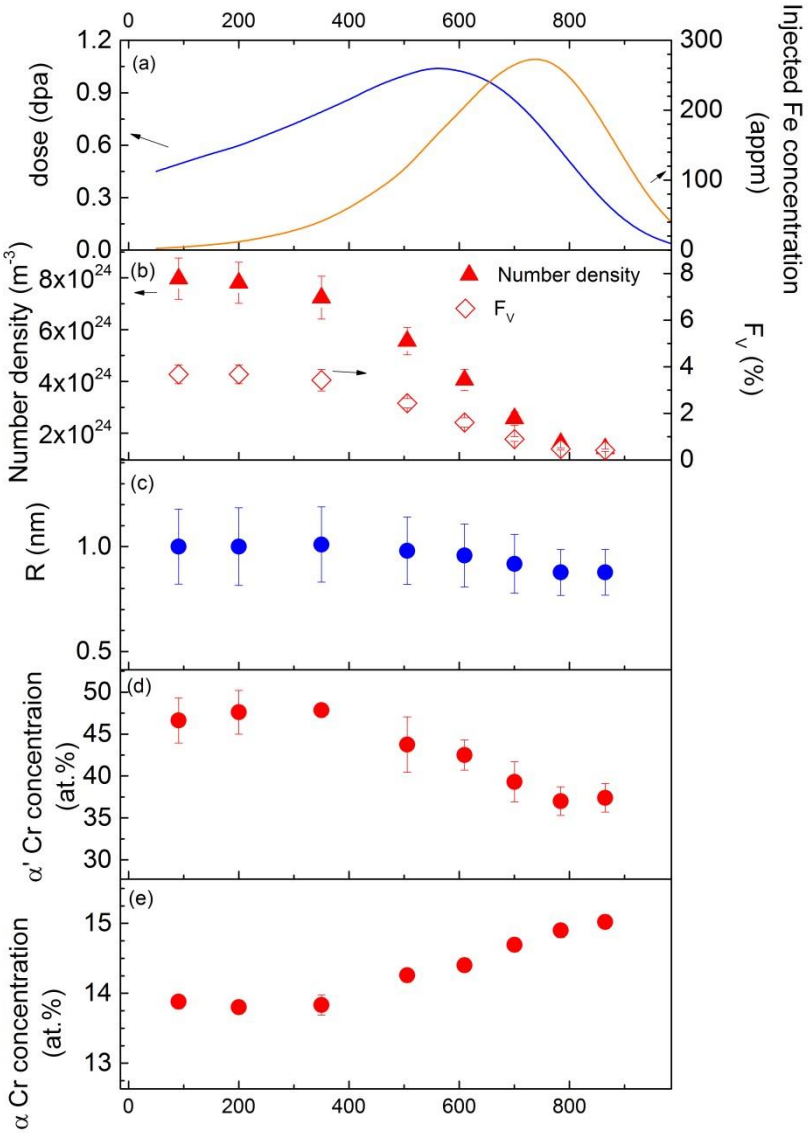

Figure 59 : Evolution with irradiation depth of (a) damage and injected Fe concentration, (b) the particle number density and volume fraction, (c) the mean particle radius, Cr concentration in (d) particles and (e) α matrix. The alloy investigated is a Fe-15at.%Cr alloy irradiated with 2MeV Fe^{2+} ions at 300°C.

Similar results were obtained on the Fe-18Cr_HR (Fe-19at.%Cr) alloy irradiated in the very same conditions. Figure 60 and Figure 61 show the results obtained for this alloy.

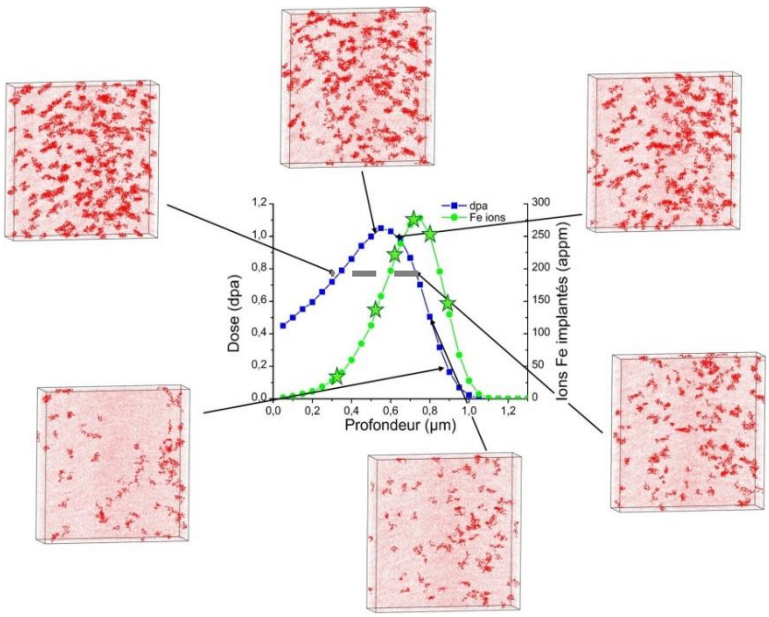

Figure 60: Damage and implantation profiles calculated with SRIM 2013 [7,8] and the 3D distribution of Cr atoms observed using APT at different depths (i.e. doses). A concentration threshold of X_{Cr}>24at.% was used to highlight α' particles. APT volume V= 40 x 40 x 10 nm^3, α' radius r ≈ 1 nm.

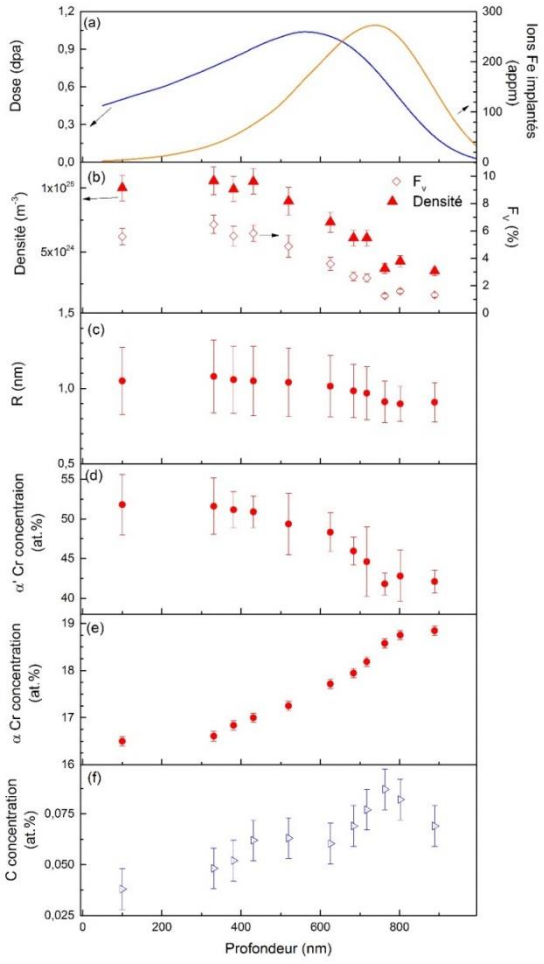

Figure 61: Evolution with irradiation depth of (a) damage and injected Fe concentration, (b) the particle number density and volume fraction, (c) the mean particle radius, Cr concentration in (d) particles and (e) α matrix. The alloy investigated is a Fe-19at.%Cr alloy irradiated with 2MeV Fe^{2+} ions at 300°C.

Finally, Figure 62 presents the comparison of the number density and volume fraction of the α' clusters as measured in both Fe-15at.%Cr and Fe-19at.%Cr. The evolution as a function of the depth is very similar. The injected interstitials have the same influence in both alloys. Whichever the alloy, from about 400 nm, a reduction of α' precipitation is observed. The volume fraction and the number density are higher in the Fe-19at.%Cr than in the Fe-15at.%Cr because of the larger driving force for precipitation in this alloy.

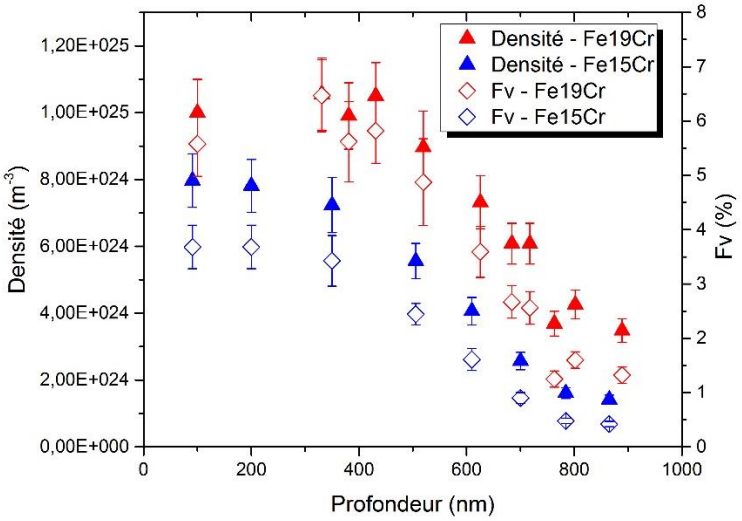

Figure 62: Comparison of the number density and volume fraction of the α' clusters measured in both Fe-15at.%Cr and Fe-19at.%Cr irradiated with 2MeV Fe^{2+} ions at 300°C.

6.1.4.2 5MeV Fe^{+}irradiation of FeCr(NiSiP) alloys

<u>NiSiP-rich clusters: Effect of impurities and alloying elements</u>

APT investigation has been made in the set of ion irradiated alloys at 2 different doses, 0.1 and 0.5 dpa at a depth of 500 nm and at a temperature of 300°C in both cases. The alloys considered here are: Fe5Cr-NiSiP, Fe9Cr-NiSiP, Fe12Cr-NiSiP and Fe9Cr (Mart.). The three former are ferritic, the latter is fully martensitic and the impurity content is less.

In the specimens irradiated at the higher dose, 0.5 dpa, solute-rich clusters (SRCs) have been found in all the analysed samples as in the case of neutron irradiations. In Figure 63, the cluster information is plotted as a function of the Cr content. The results indicate that the number density and radius of clusters are quite similar, with perhaps a slight decrease in radius with Cr content increase. Concerning the solute composition of the clusters, the enrichment in Ni, Si and P is larger in the 5Cr, mainly because of Si enrichment that is 3% more in the Fe5CrNiSiP than in the two others. A slight decrease in Ni content is also observed when Cr content of the alloy increases. The more Cr in the alloy, the more Cr in the clusters. Nevertheless, it must be emphasized that the enrichment (difference in concentration between the clusters and the nominal concentration in Cr) increases when the nominal concentration in Cr decreases : ΔC = 5at.% for the Fe5CrNiSiP, ΔC = 3.8at.% for the Fe9CrNiSiP, ΔC = 1at.% for the Fe14CrNiSiP. After ion irradiation, contamination in C has been measured (Figure 64). The C concentration measured in the clusters is of about 0.4-0.5 at% in the cases of Fe5Cr-NiSiP and Fe9Cr-NiSiP and 0.1 at% in the Fe14Cr-NiSiP alloy. In the case of Fe9Cr(Mart.) the C enrichment was found to be one order of magnitude smaller than in the case of Fe9Cr-NiSiP (0.07% vs 0.2%). It is worth noting that the C contamination is not identical from tip to tip made in the same material. One can find one order of magnitude in C concentration between to different tips made in different grains of the same material.

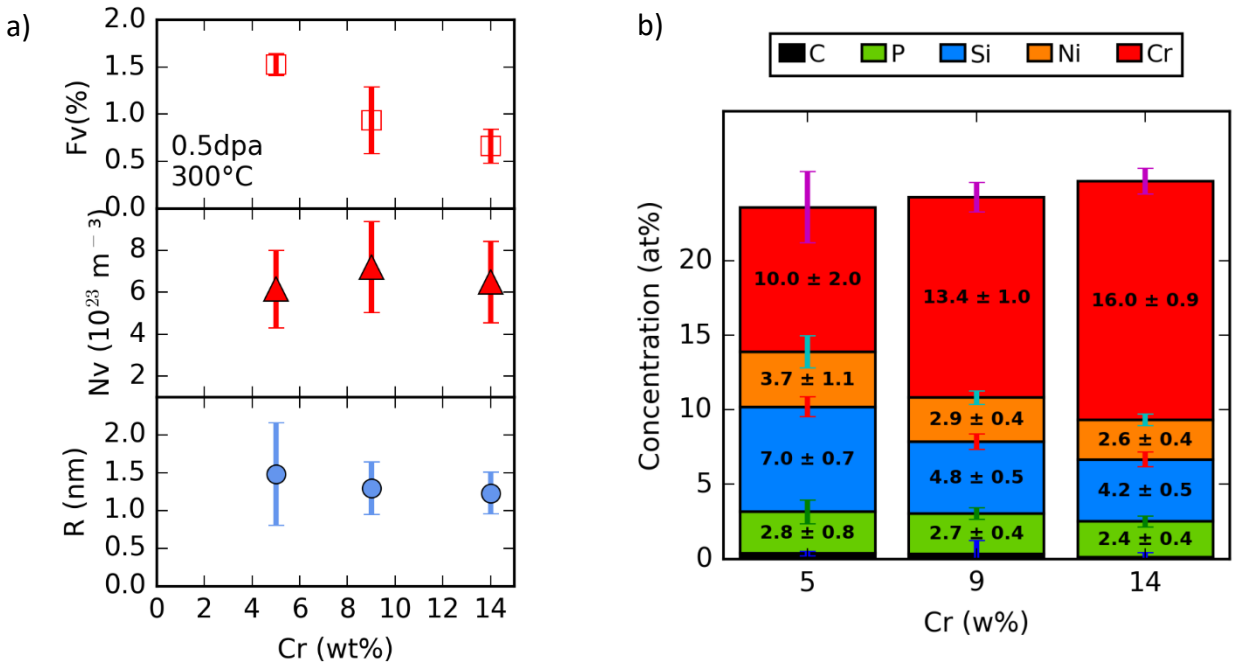

Figure 63: Cluster characteristics of ion-irradiated specimens at 0.5 dpa at 300 ℃ as a function of the %Cr. a) volume fraction, Number density (Nv) and R of the SRCs, b) Solute concentration of the clusters. Fe concentration makes the balance to 100%.

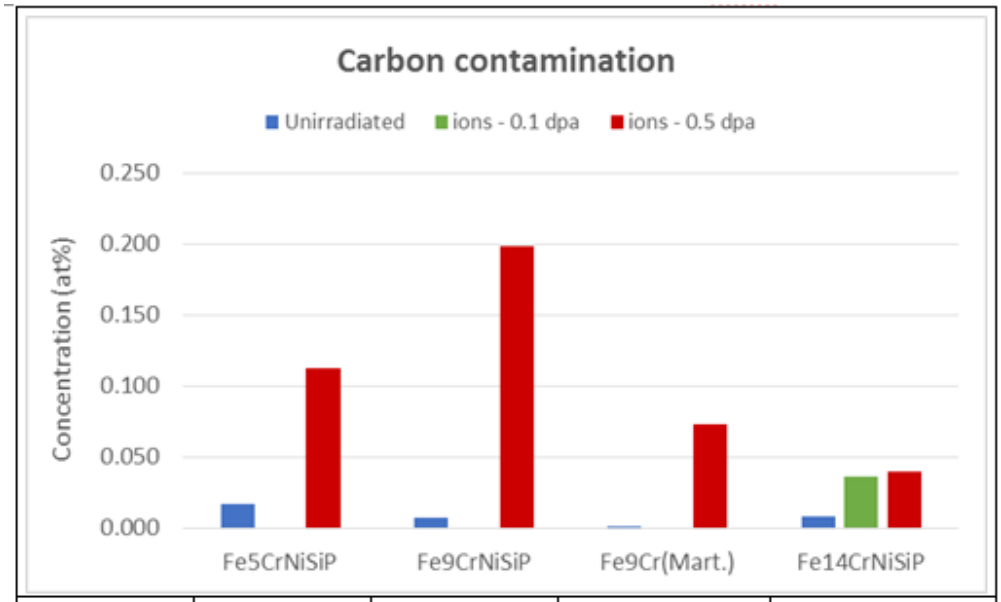

Unirradiated	0.017 ± 0.021	0.008 ± 0.008	0.002 ± 0.002	0.008 ± 0.018
Ions – 0.1 dpa	NA	NA	NA	0.036 ± 0.066
Ions – 0.5dpa	0.113 ± 0.052	0.198 ± 0.422*	0.073 ± 0.080	0.040 ± 0.243**

Figure 64 : C content as measured with APT in the different alloys and under the different conditions. .NA: no analysis.
*C varies between 0.2 and 0.05 at% depending on the tip (4 tips analysed)
**C varies between 0.28 and 0.007 at% depending on the tip (7 tips analysed)

In Figure 65 the cluster information is plotted against the total amount of impurities ($X_P+X_{Si}+X_{Ni}$) for the Fe9Cr alloys at 0.5 dpa. The alloy with 0.17wt.% of impurities is the Fe9Cr MIRE alloy with a martensitic structure. The alloy with 0.34 wt.% of impurities is the Fe9CrNiSiP with a ferritic structure. The number density of clusters is 3 times smaller for the smaller impurity content whereas the radius is larger. The volume fraction of clusters is larger as the concentration of NiSiP is increased. Enrichment in Si and P seems to be larger when the NiSiP content is larger.

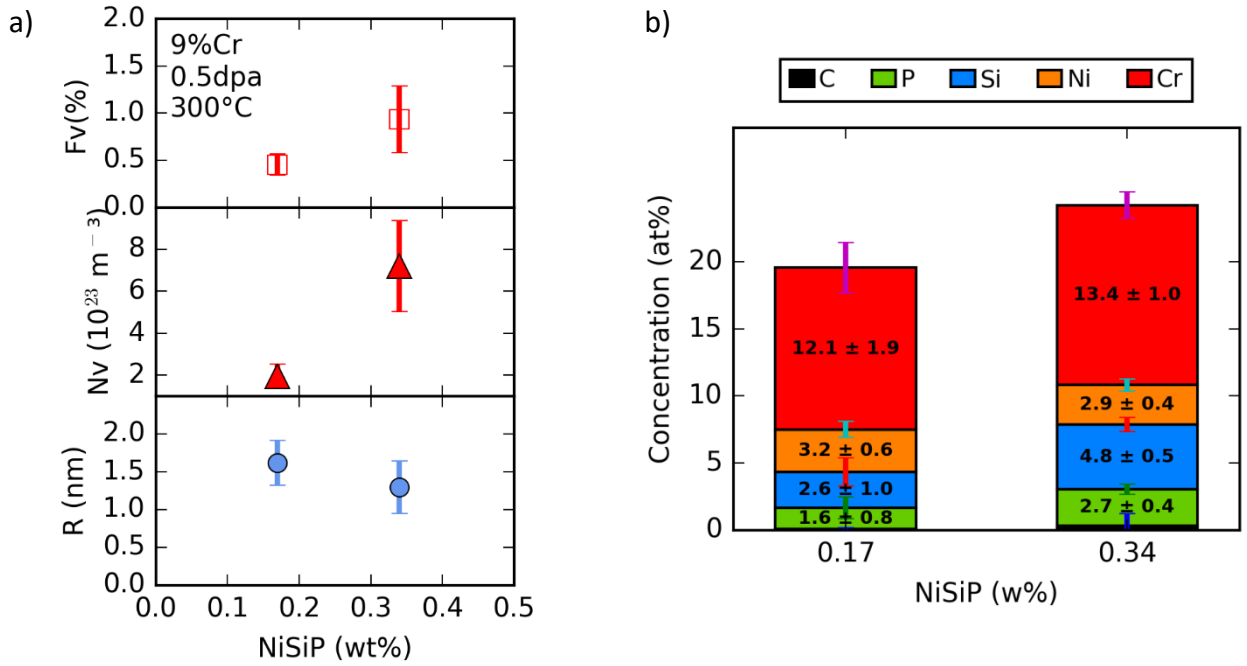

Figure 65: Cluster characteristics of ion-irradiated specimens at 0.5 dpa at 300^{0}C as a function of the %NiSiP, the materials Fe9Cr(Mart.) and Fe9CrNiSiP are compared. a) volume fraction, number density and radius of the NiSiP-rich clusters, b) Solute concentration of the clusters. Fe : balance up to 100%.

Further investigation on the role of every impurity in the cluster formation has been carried out by studying the materials Fe14CrNi, Fe14CrSi, Fe14CrP and Fe14CrNiSiP, both AR and ion-irradiated at 0.1 dpa at 300^{0}C. The solute distributions obtained on the APT volumes are shown in Figure 66. After visual investigation it is clear that the P atoms have grouped together after 0.1 dpa. However, the same conclusion cannot be extracted straightforwardly in the cases of Ni and Si impurities. Therefore the 1NN distances distributions have been calculated and the V-parameter has been extracted (see section 2.2.4). The V-parameters are plotted as a function of the impurity studied (P-P, Ni-Ni or Si-Si) and on the irradiation condition (AR or 0.1 dpa). The data on the four studied materials are represented in the Figure 67. Every dot corresponds to a different AP volume analysed, so the dispersion on the experimental results is illustrated. Clear tendencies are observed. The higher the V-parameter is, the more deviated from the random distribution are the Ni, Si or P populations. As expected, in AR state, no clustering is observed. At 0.1 dpa, the results suggest that the clustering is occurring for the 3 impurities but the intensity of this clustering is much higher in the case of P. Very interestingly, this does not depend on whether the impurities are alone or together in the alloy. Indeed, the same results for every impurity are obtained in the case of Fe14CrNiSiP and of Fe14CrNi for Ni, Fe14CrP for P and FeCrSi for Si. These results strongly suggest that no synergistic effects are occurring in the cluster formation due to the presence of the other impurities, i.e. that no thermodynamic force acts to take the solutes together.

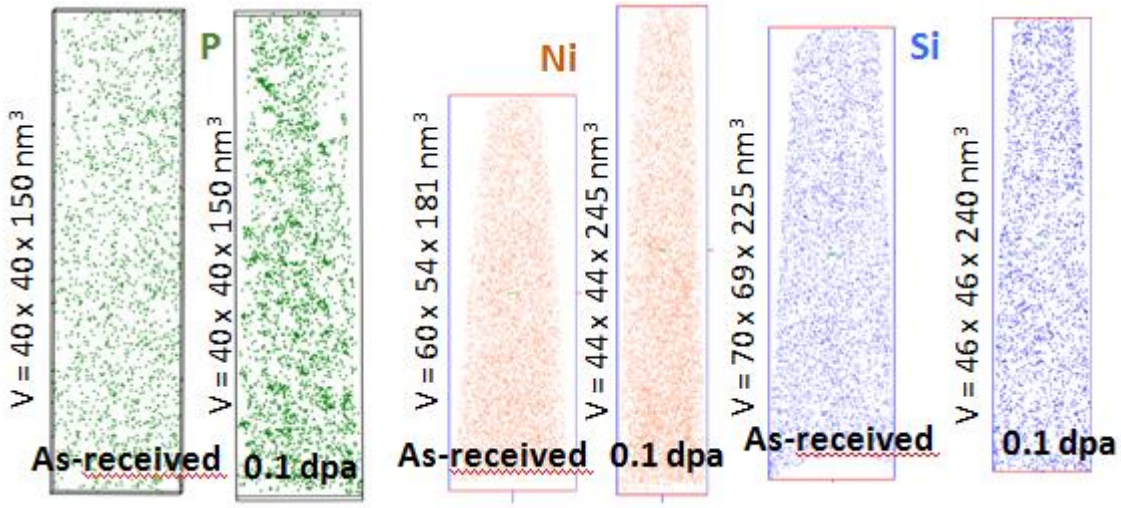

Figure 66: Spatial distribution maps of P (green dots), Ni (orange dots) and Si (blue dots) in Fe14CrP, Fe14CrNi and Fe14CrSi. Comparison between AR states and 0.1 dpa ion-irradiation at 300^{0}C is shown. All the sampleshave been analysed at a depth of 500±100 nm.

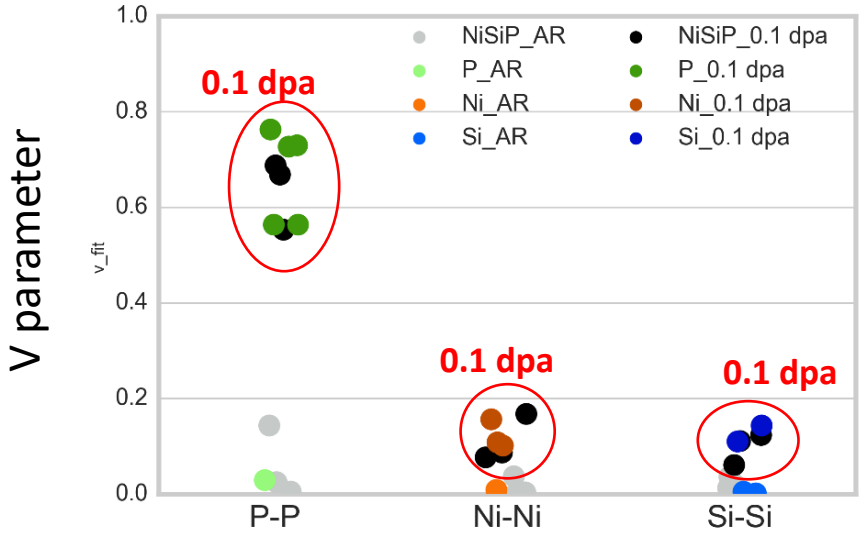

Figure 67: V-parameter obtained from 1NN distributions of X = (P, Ni, Si) impurities. AR results and 0.1dpa ion-irradiation condition are plotted. The studied samples are Fe14CrP, Fe14CrNi, Fe14CrSi and Fe14CrNiSiP. Dots of the same color represent different AP volumes analysed.

NiSiP-rich clusters: Effect of the dose

The dependence of the small solute clusters on the dose has been investigated in the Fe14Cr-NiSiP model alloy. Figure 68 shows the distribution maps of Ni, Si and P. Small clusters are already formed and visible on 3DAP images at 0.1 dpa. Even if very tiny and thus at the limit of the range of applicability of the "Iso-position" tool, the clusters have been characterised using the iso-position filter in order to compare with higher dose. Nevertheless, it must be kept in mind that the results at 0.1 dpa are here shown as a qualitative indicator of the behaviour of SRC with dose and that uncertainties are significant, even if impossible to quantify. The results are plotted in Figure 69 as a function of the dose. The volume fraction found at the low dose condition is extremely small. So as the number density, which is found to be one order of magnitude smaller (~10^{22} m^{-3}) than at 0.5 dpa, and the size, which is close to the detection limit. These results, even if qualitative, show that as the ion dose increases, the size, the number density and the volume fraction of the solute-rich clusters are increasing. Regarding the evolution of the concentration of the clusters with the dose, P is observed to enrich first the SRCs as it has been observed under neutron irradiation (section 4.1.5). A surprisingly high Cr enrichment with respect to 0.5 dpa is also observed. But given the very large uncertainties, this enrichment is probably not especially meaningful.

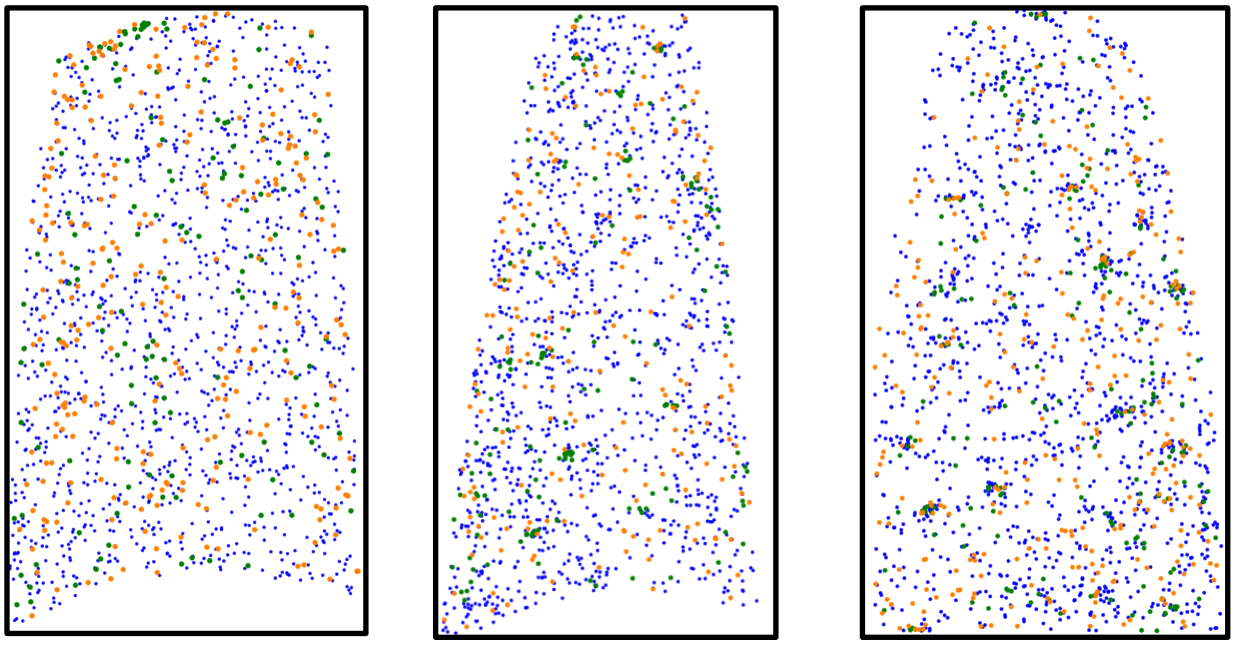

Vol. = 53 x 2 x 89 nm^3 | Vol. = 50 x 2 x 91 nm^3 | Vol. = 50 x 2 x 90 nm^3

a) b) c)

Figure 68: Impurity distribution maps in the Fe14CrNiSiP alloy. a) AR condition, b) ion-irradiation at 0.1 dpa, 300 ºC, c) ion-irradiation at 0.5 dpa, 300 ºC. Si is indicated by the blue dots, whereas Ni and P are in orange and green respectively.

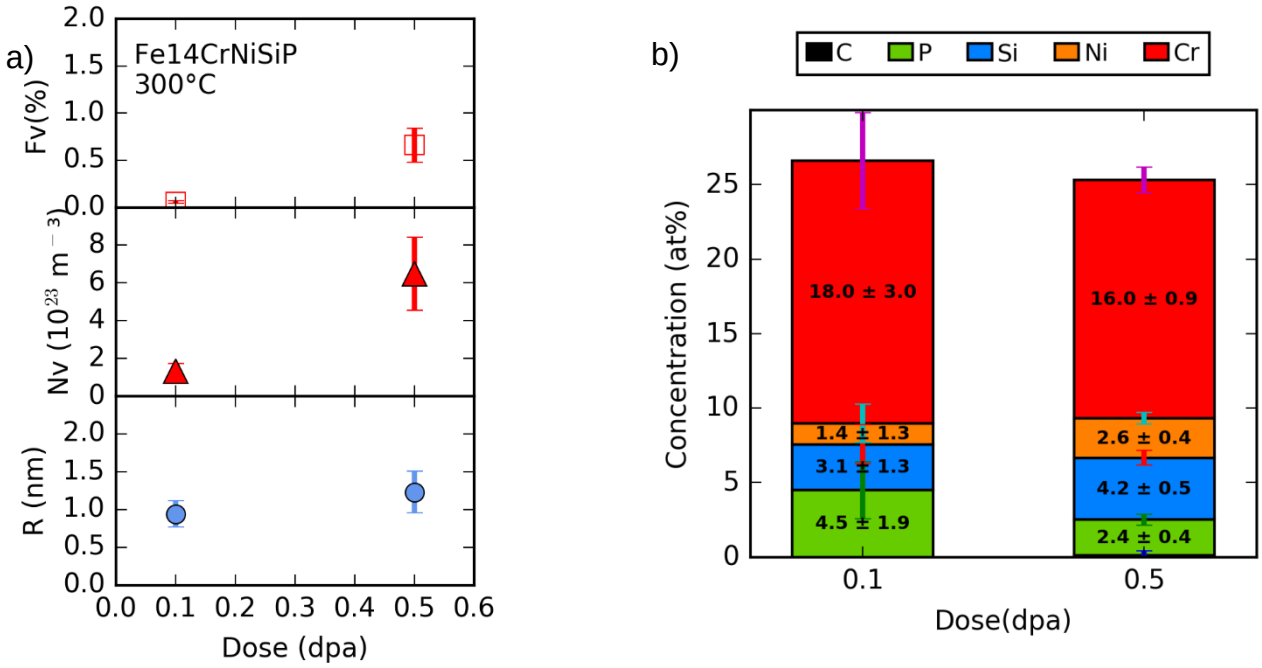

Figure 69: Cluster characteristics on Fe14CrNiSiP material ion-irradiated at 300 ºC as a function of the dose. a) volume fraction, number density and radius of the NiSiP-rich clusters, b) Solute concentration of the clusters. Fe : balance up to 100%.

SRCs are mainly observed to be homogeneously distributed in the APT volumes. Nevertheless, in some cases, they appear aligned, probably along a dislocation line (Figure 70). In some other cases, Ni, Si and P are seen to form circular objects, evidencing segregation of these species at dislocation loops (Figure 70, Figure 71). Also visible in Figure 71, continuous segregation of Ni, SI and P at dislocation lines.

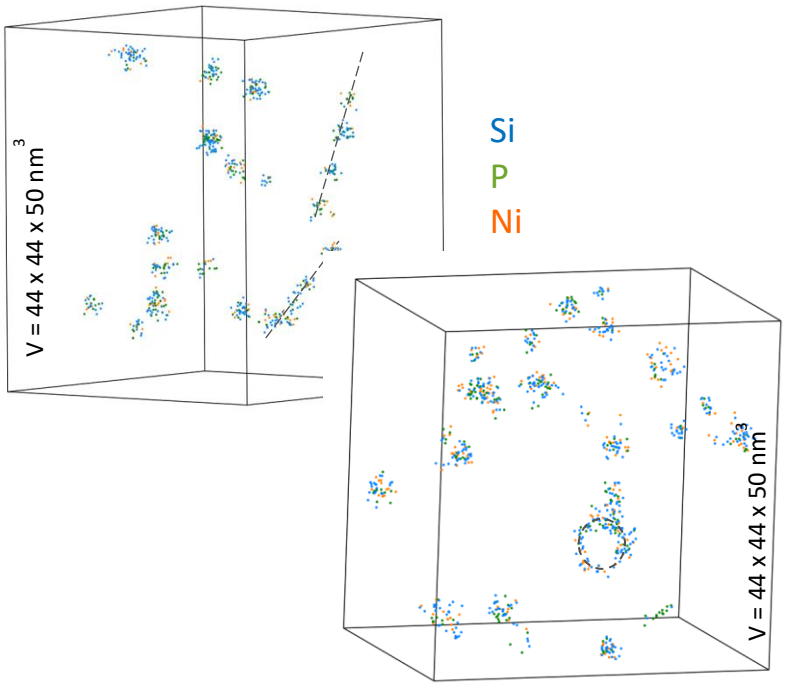

Figure 70: 3D atom map of Ni, Si and P atoms forming SRCs in Fe9Cr MIRE alloy irradiated at 0.5 dpa at 300°C. The threshold used to highligt clusters is XNi+Si+P > 2.1at.%.

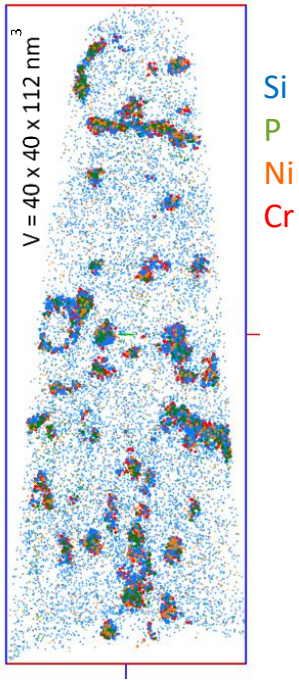

Figure 71: 3D atom map of Ni, Si and P atoms forming SRCs in Fe5CrNiSiP alloy irradiated at 0.5 dpa at 300°C. The threshold used to highligt clusters is XNi+Si+P > 2.9at.%.

Cr-rich clusters

The Cr distribution has been also investigated after ion irradiation in all the investigated materials (containing 5, 9 and 14 wt% of Cr) at every dose (AR, 0.1 and 0.5 dpa) at 300^{0}C.

The results for the Thuvander et al. test (cf. section 2.2.4) are shown in Figure 73, Figure 74 and Figure 75, for samples containing 14%, 9% and 5% of Cr respectively. Every curve is labelled with a 4 digit id number from a particular APT experiment, the irradiation condition (AR, 0.1 dpa or 0.5 dpa) and the type of impurity (P, Ni, Si or NiSiP). Cr distribution is quite close to the random distribution in the as-received (AR) specimens, for all Cr concentrations.

The results on the 14% of Cr concentration are shown in Figure 73. The sliding of the curves towards upper areas of the graph can be appreciated as the dose is increasing. This is a sign of the clustering of Cr in the case of Fe14CrX. It is also observed that the presence of impurities has no impact on Cr evolution. At the lowest dose, 0.1 dpa, early stages of Cr clustering are detected as the curves are higher than in the AR state. At 0.5 dpa the Cr clusters become visible (see Figure 72).

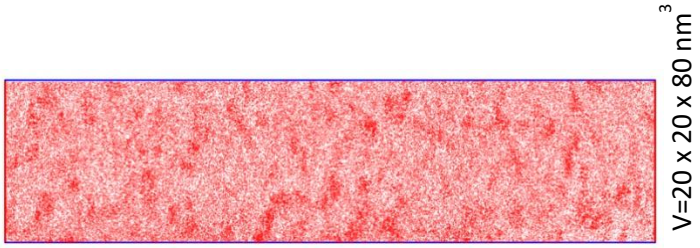

Figure 72: 3D distribution of Cr atoms in Fe14CrNiSiP irradiated at 0.5 dpa at 300°C. α' clusters are clearly visible.

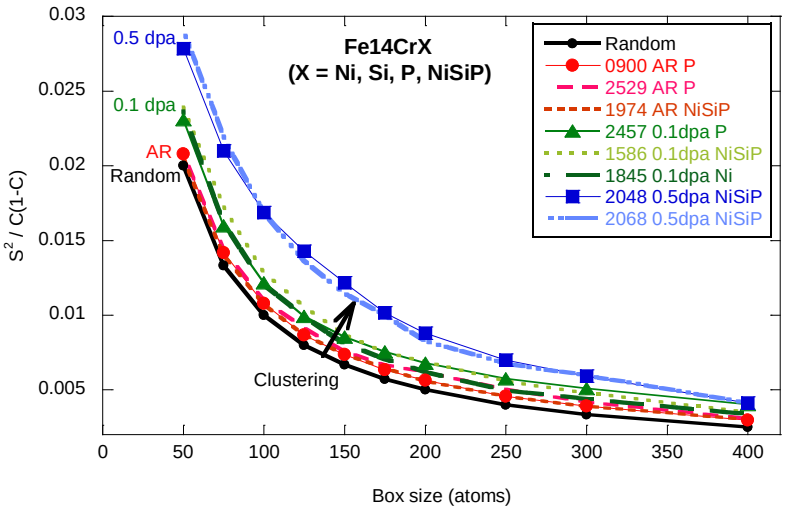

Figure 73: Results from the Thuvander et al. test on different MatISSE model alloys containing 14% of Cr and different impurity levels. The black line corresponds to the binomial distribution. The red lines (and red circles) correspond to samples at the AR state. The green lines (and green triangles) correspond to samples irradiated to 0.1 dpa. The blue lines (blue squares) correspond to 0.5 dpa irradiation condition.

The results on the 9% of Cr concentration are shown in Figure 74. Apparently no signs of Cr clustering are experimentally observed in the irradiated alloys. A similar behaviour is observed for the Fe5CrNiSiP (Figure 75). No signs of Cr clustering are identified.

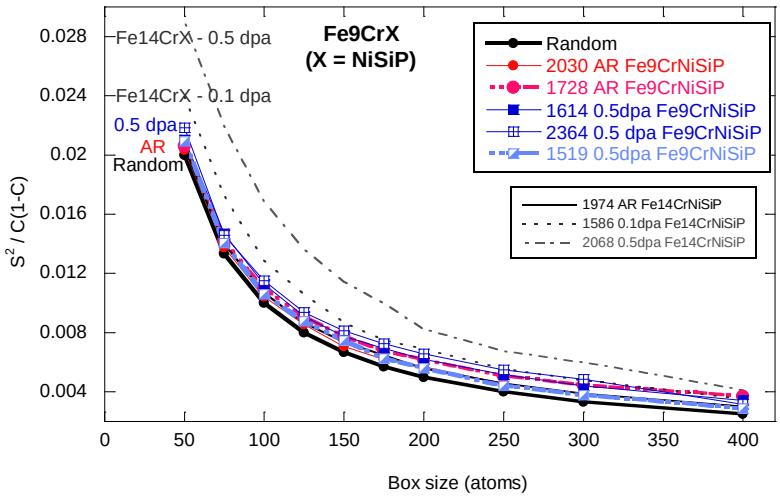

Figure 74: Results from the Thuvander et al. test on Fe9CrNiSiP. The black line (black spots) corresponds to the binomial distribution. The red lines (red spots) correspond to samples at the AR state. The blue lines (blue squares) correspond to 0.5 dpa irradiation condition. For comparison purposes, the data corresponding to 0.1 and 0.5 dpa conditions of Fe14CrX samples is also indicated in black dashed lines.

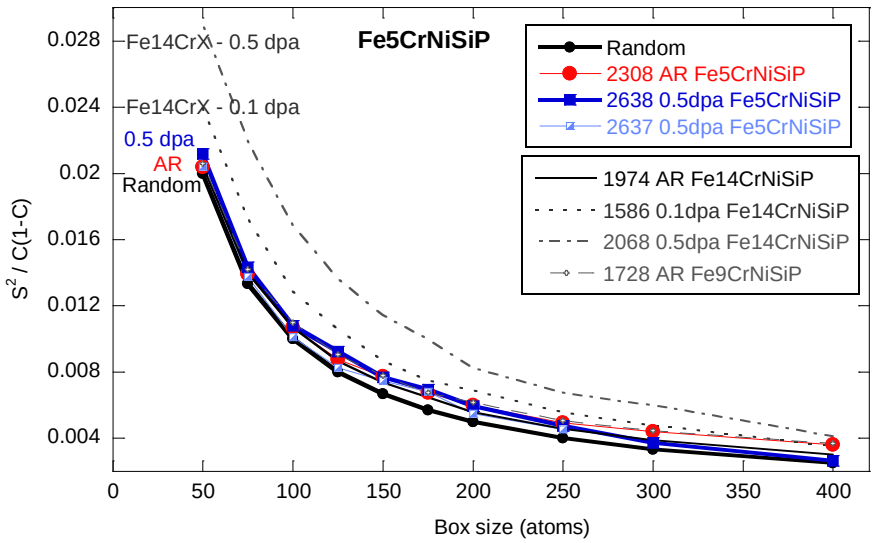

Figure 75: Results from the Thuvander et al. test on Fe5CrNiSiP. The black line (black spots) corresponds to the binomial distribution. The red lines (red spots) correspond to samples at the AR state. The blue lines (blue squares) correspond to 0.5 dpa irradiation condition. For comparison purposes, the data corresponding to 0.1 and 0.5 dpa conditions of Fe14CrX samples is also indicated in black dashed lines.

Characteristics of Cr-rich clusters found at 0.5 dpa in the Fe-14Cr-NiSiP and Fe14Cr_HP alloys are plotted in Figure 76 and compared to the results presented in section 6.1.4.1 where a ultra-high-purity alloy (Fe14Cr_HP) was irradiated at 2 MeV also at 0.5 dpa. Radiuses are similar but number density and volume fraction are larger in the high purity alloy. It is difficult to discuss these differences as the materials were irradiated with different ion energies and in different irradiation facilities. More work is needed to understand similarities and differences.

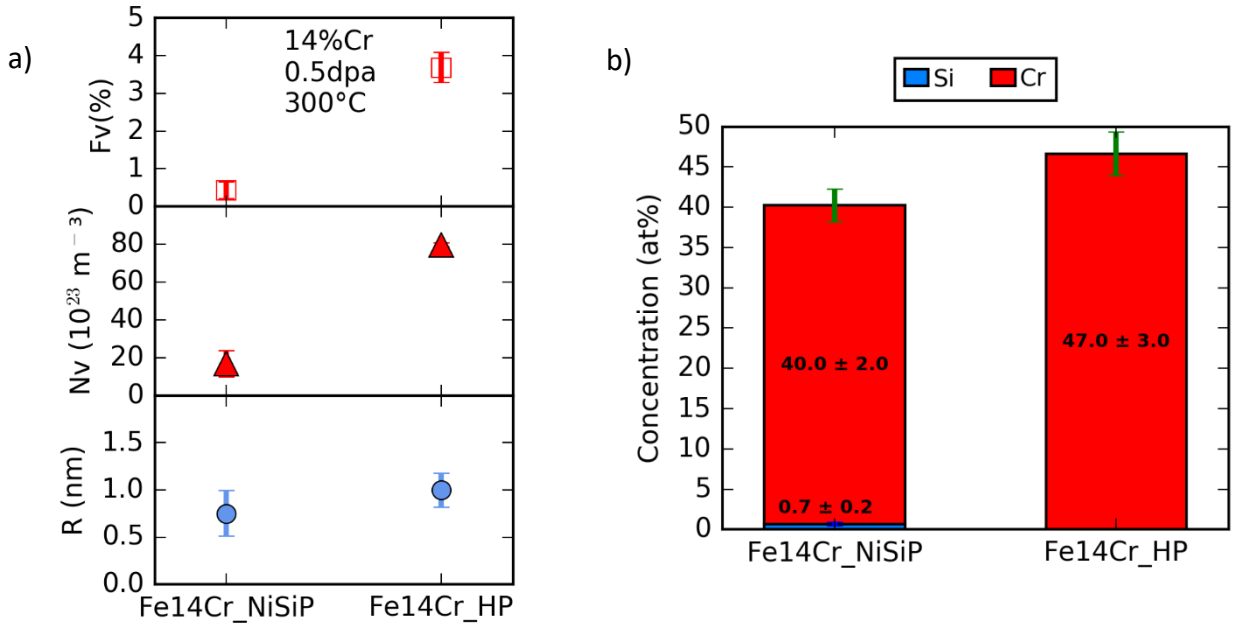

Figure 76: Characteristics of the Cr-rich clusters on ion-irradiated materials at 300^{0}C, Fe14CrNiSiP and Fe14Cr_HP. Both doses should be equivalent to 0.5 dpa a) Fv, Nv and R of the Cr-rich clusters, b) Solute concentration of the clusters.

7 Summary and discussion

High purity Fe-Cr alloys with 14wt% and 18wt%Cr and 16 alloys with different Cr, Ni, Si and P contents were selected for investigation after neutron, ion and electron irradiation. This deliverable presented the PIE results obtained by standard mechanical characterisation and with advanced characterisation techniques.

With the exception of the alloys inherited from the GETMAT project (Mire-Cr irradiation campaign) all alloys studied here have a ferritic structure. The size of the grains depends on the composition. The Fe-14CrX alloys have the larger grains (~230µm), the Fe-9CrX the smallest (~25 µm). The yield strength increases with Cr and impurity contents from 196 MPa for pure Fe up to 268 MPa for Fe-14Cr-NiSiP. A similar trend is observed for hardness (from 58 HV to 123 HV).

Internal friction measurements revealed the presence of C in solid solution in Fe and in Fe5Cr. In Fe-14Cr-NiSiP, C atoms were found to bind to open-volume defects (probably dislocations). C was also detected using APT in Fe-5Cr-NiSiP, Fe-9-CrNiSiP and Fe-14-CrNiSiP. APT analysis also confirmed the homogeneous distribution of Cr and impurities in the grains.

7.1 Neutron irradiations

Fe, Fe5CrNiSiP, Fe9Cr, Fe9CrNiSiP, Fe14CrNiSiP, Fe9Cr MIRE, E97 and T91 were neutron irradiated at 290°C and 450°C in the BR2 reactor at a dose of 0.11 dpa.

SANS results obtained on Fe-5Cr-NiSiP and Fe-14Cr-NiSiP show that nano-features are formed at both irradiation temperatures. The volume fraction of irradiation-induced clusters in Fe-14Cr-NiSiP is one order of magnitude higher than in Fe-5Cr-NiSiP.

It is assumed that there are two components in the size distribution of 14Cr-NiSiP irradiated at 290°C, i.e. the second component is also significant. The first component is dominant. The A ratio (2.15) indicates α'. The second component is two orders of magnitude weaker in terms of number density. From previous investigations it is reasonable to assume that these are NiSiP-containing clusters or NiSiP-decorated loops. APT is needed to substantiate this interpretation. For the irradiation temperature of 450°C, the SANS measurements indicate similar results. The sizes are slightly larger and the volume fraction is slightly smaller. The A-ratio for the first (dominant) component again indicates formation of alpha-prime. However, according to the Fe-Cr phase diagram [1] much less alpha prime than for 290°C should form if any. This needs further investigation.

For Fe5CrNiSiP, the higher A-ratio (3.5) reveals a difference in the nature of the nano-features formed, it is reasonable to assume that these are NiSiP-containing clusters or NiSiP-decorated loops. The constant A-ratio indicates that the nature of the nano-features does not change with irradiation temperature. There is a significant increase in their mean radius at 450°C with respect to 290°C. PALS measurements performed on the Fe14CrNiSiP revealed that vacancy clusters were only observed at 290°C. The size of these clusters remains small i.e. about four vacancies. Dominant trapping centre for positron are mono-vacancies.

TEM focussed on Fe, Fe9Cr and Fe9CrNiSiP irradiated at 450°C. The investigation of the neutron irradiated microstructures of these three materials may provide information about the effect of Cr content and the effect of the presence of impurities such as Ni, Si and P. The loops are homogeneously distributed in all the samples. Qualitative comparison of TEM images leads to deduce that the presence of Cr reduces size and increase number density of loops and the effect of Ni, Si and P addition is to further reduce loop size and increase loop number density.

FeCr model alloys show different behaviour under neutron irradiation depending on their chemical composition. For the samples which were neutron irradiated at 300°C, it is found that Fe9Cr does not harden if compared to the as-received while Fe5CrNiSiP, Fe9CrNiSiP and Fe14CrNiSiP show significant hardening. After neutron irradiation at 450°C, Fe9Cr does not harden whereas Fe9CrNiSiP and Fe14CrNiSiP show significant hardening. Concerning Fe5CrNiSiP, it shows similar hardening as the non-irradiated sample which is thermally aged at 450°C but shows hardening with respect to the sample thermally aged at 450°C.

Tensile tests show that the Fe5CrNiSi, Fe9CrNiSiP and Fe14CrNiSiP experience a significant hardening during irradiation at 290°C. It is similar at 450°C except for Fe5CrNiSiP which shows a much lower hardening. Surprisingly, hardening of Fe14CrNiSiP is not larger than that of Fe9CrNiSiP whereas one could expect a much higher density of α' particles in the 14Cr. Neither for the Fe9Cr nor for Fe hardening has been observed

whereas a high density of dislocation loop has been shown to form. But it is worth noting that YS were obtained on round samples for unirradaited alloys whereas they were obtained on flat samples for the irradiated ones. The direct comparison may thus be questionable.

APT analysis were performed on the Fe-9Cr MIRE and Fe-12Cr MIRE irradiated at 0.06 dpa at 300°C. Results showed that at this low dose, neither in the Fe-9Cr nor in the Fe-12Cr α' clusters form. Solute rich clusters (SRC) were observed to form in both alloys. They are very rich in P and present a very slight Cr enrichment if any. If compared to 0.6dpa, there is a slight increase in number density and in volume fraction with dose and a slight decrease in size. At low dose, the P concentration is very high (6–7at.%) whereas the nominal content is only 0.06at.%. At higher dose, it decreases to the level of 2at.% because of the important increase in Si, Ni and Cr content. This is coherent with the fact that these latter have much lower diffusion coefficient than P and more time is needed for them to enrich clusters.

7.2 Ion and electron irradiations

The alloys were irradiated at 0.1 and 0.5 dpa at 200°C, 350°C and 450°C. They were analysed using PAS, TEM, APT and NI. The results presented in parts 5 and 6 addressed the effects of: temperature, Cr content, impurities, irradiation dose, injected interstitials.

7.2.1 Effect of temperature and Cr content

PAS investigation of Fe5CrNiSiP, Fe9CrNiSiP and Fe14CrNiSiP irradiated to 0.5 dpa at 200°C, 350°C and 450°C showed that the vacancy-defects concentration and cluster size decrease between 200°C, 300°C and 450°C. At 450°C, the concentration of defects is too low to be detected in Fe9CrNiSi. The open-defect density is higher in the Fe14CrNiSiP than in the Fe5CrNiSiP at 200°C and at 300°C whereas there is no significant difference at 450°C.

Regarding hardening, it decreases as the irradiation temperature increases whatever the Cr concentration. The highest hardening is observed for Fe5Cr-NiSiP at both temperatures. The hardening of Fe9Cr-NiSiP and Fe14Cr-NiSiP is similar. There is no distinct minimum of hardening at 9%Cr. The results indicate that α'-phase mediated hardening is not the dominant hardening contribution. Indeed, as shown by APT, if α' clusters are formed in Fe14CrNiSi, their Cr concentration is quite low and they are quite diffuse. Consequently, they should be weakest obstacles than richer α' clusters. The hardening is rather dominated by NiSiP(Cr)-clusters and dislocation loops. SRCs are observed in all the alloys but the difference in number density and in size cannot explain the difference in hardening between the Fe-5CrNiSiP and the two other alloys. As the small size of the open-defects observed cannot also explain this difference, one could expect difference in dislocation loop densities and sizes.

7.2.2 Effect of Ni, Si and P impurities

All the experimental characterisations performed evidence the strong influence of impurities on the microstructural evolution of the materials and in turn on the radiation hardening.

Different impurity contents have been investigated for a given Cr content: the pure Fe-9Cr with 0.016wt% of impurities (Ni+Si+P), the Fe-9Cr MIRE with 0.17wt% and the Fe9CrNiSiP with 0.34wt%. It has been evidenced that the higher the impurity content:

- the higher the concentration of vacancy defects
- the lower the size of the dislocation loops (DL)
- the higher the proportion of <111> DL (for the highest content, the majority of loops is <111> whereas it is the inverse for pure Fe, Fe9Cr and Fe9Cr MIRE)
- the highest the number density (3 times higher for 0.34wt% than for 0.17wt%) of SRCs and the lower their size.
- the richer the SRCs in impurity and Cr
- the harder the material, whatever the irradiation temperature.

The presence of Ni, Si and P has a strong impact on the irradiation response in terms of enhancing irradiation-induced hardening. Moreover, it must be emphasised that there is no obvious effect of the initial microstructure (Fe9Cr MIRE is F/M whereas the others are ferritic). Composition seems to be predominant over the effect of initial microstructure.

It is interesting to note that the SRC size evolves as DL size: it decreases when impurity content increases. The same behaviour is not observed for the number density of the DL: the same value is obtained whatever the impurity content. Nevertheless, it cannot be ruled out that, because of the small size of DL, a part of these are no more visible with TEM. If it is the case, this means that the number density of the DL increases as the SRC number density. Moreover, Ni, Si and P have been observed to segregate at dislocation loops and to form clusters at dislocation lines. This confirms the affinity of these species with point defect sinks and thus validate the SCMF calculations that predict solute dragging towards sinks for P, Ni and Si by vacancies and by interstitials for P [69–71]. According to these results, it appears that association of SRCs to TEM invisible loops is very likely. This agrees with the results obtained by OKMC simulations [72] that found a number density of invisible TEM DL similar to the one of the SRCs observed with APT.

TEM results obtained on the pure Fe-9Cr and on Fe14Cr_HP pose an important question that deserves further investigation: very surprisingly, <100> loops were found in majority in pure Fe-9Cr (93%) after ion irradiation and in Fe-15Cr_HP (100%) after electron irradiation. These proportions are similar to those measured in pure Fe or low Cr. Up to now, it was accepted that Cr increases the proportion of <111> loops. In the light of these new results, it seems that what is determinant is not so Cr content but rather the impurity content. If this is the case, experiments and DFT calculations could converge as according to DFT, Cr is not found to favour <111> DL. However, it is accepted both on the basis of simulation and experiment that Cr does slow down interstitial clusters. If the origin of the observation of ⟨111⟩ loops is to be ascribed to reduced mobility and therefore reduced absorption at sinks, then Cr should have an effect on increasing the proportion of ⟨111⟩ lops. Yet it is possible that impurities such as Ni, Si and especially P have even stronger effect in reducing the mobility of otherwise fast gliding ⟨111⟩ loops [73]. Further investigations are needed to understand these new results. An intensive study of the bibliography is part of the work to be provided.

The comparison of samples containing different alloying elements has shown that P plays an important role in the early formation of vacancy type defects compared to Ni and Si elements. When P is present, alone or together with Ni and Si, the concentration in open-defects is significantly increased. Among the three impurities, P is the one that stabilizes more vacancy defects and importantly, P increases the proportion of mono-vacancy defects, probably reducing their mobility, thus preventing or retarding the formation of larger vacancy clusters. Addition of both Ni and Si to FeXCr-P does not result in an increase in concentration of open defects. Concerning impurity clustering, the very same conclusion was drawn: P has the strongest tendency for clustering. No synergetic effect has been evidenced as the clustering does not dependent on the fact that the impurities are alone or together in the alloy. This is in agreement with the calculation of Messina et al. [69–71]. P has the strongest tendency to enrich sinks because of its very strong positive coupling with point defects.

Among Ni, Si and P, Phosphorus has thus been shown to have the strongest effect on the stabilization of vacancies (mainly mono-vacancies) and on the formation of clusters.

7.2.3 Effect of irradiation dose

The vacancy-type defect density is higher at 0.1 dpa than in 0.5 dpa in both Fe9CrNiSiP and Fe14CrNiSiP. In Fe-9Cr samples, the irradiation at 300°C and 0.1 dpa mainly mono-vacancies and vacancy clusters are detected. At 0.5 dpa, the distribution of the vacancy-type defects has changed. Most probably the reason for this is not really a decrease in the density of vacancy type clusters, but the fact that the dislocation density has increased (formation and growth of dislocation loops), leading to a decrease of the S values and an increase of the W values.

The number density of the SRCs is one order of magnitude lower at 0.1 dpa than at 0.5 dpa at 300°C. The size and the number density increase with the dose. Regarding the evolution of the concentration of the clusters with the dose, P is observed to enrich in a higher proportion the SRCs at low dose than at higher dose as it has been observed under neutron irradiation. This is the consequence of the fact that P is the most easily and fast deposited solute of all.

7.2.4 Effect of injected interstials

Fe-14Cr_HP alloy irradiated with 2 MeV Fe^{2+} ions at 300°C was investigated with APT. The 3D distribution of Cr atoms revealed the presence of α' particles. It was the first time that α' precipitation was observed under

heavy ion irradiation. Such observation has been confirmed later in the Fe14CrNiSiP irradiated at 0.5 dpa at 300°C. Characterisation of α/α' decomposition with depth and comparison with both the damage and injected Fe concentration profiles show that:

- Evolution of α' precipitation deviates significantly from that is expected from the damage profile.
- Injected Fe strongly reduce α' precipitation.

The origin of this behaviour can be explained as follows. The excess of interstitials due to injected Fe has two major effects: the enhancement of recombination between vacancies and interstitials and the creation of a high density of point defect sinks (interstitial clusters, dislocation loops). Both effects lead to a significant decrease in concentration of point defects, which are required for the diffusion of Cr atoms to form α' precipitates. Consequently, α' precipitation kinetics is reduced.

According to these results, absence of α' precipitates in previous ion irradiation experiments is very likely due to the presence of a high concentration of injected interstitials because of the use of multi-step irradiations, very high dose rates or investigation at the damage peak. Multi-step ion irradiations or characterisation at the damage peak in order to reach high irradiation doses are thus not recommended.

8 References

[1] C. Fazio, D. Gomez Briceno, M. Rieth, A. Gessi, J. Henry, L. Malerba, Innovative materials for Gen IV systems and transmutation facilities: The cross-cutting research project GETMAT, Nucl. Eng. Des. 241 (2011) 3514–3520. doi:10.1016/j.nucengdes.2011.03.009.

[2] M. Hernandez-Mayoral, L. Malerba, M. Lambrecht, V. Kuksenko, C. Pareige, P. Pareige, F. Bergner, C. Heintze, A. Ulbricht, T. Toyama, M. Ramesh, B. Minov, M. Konstantinović, GETMAT delivrable Neutrons, GETMAT FP7-212175 Deliv. D49. (2013).

[3] M. Hernandez-Mayoral, V. Kuksenko, C. Pareige, P. Pareige, P. Desgardin, B. Décamps, M.-F. Barthe, A. Nordlund, P. Cartemo, A. Idhil, C. Borca, C. Heintze, GETMAT delivrable Ions, GETMAT FP7-212175 Deliv. D47. (2013).

[4] J. Coze, Final Rep. Model Alloy Prep. Armines Ecole Natl. Supér. Mines St. Etienne-CNRS UMR5146. (2007).

[5] Y. Serruys, P. Trocellier, S. Miro, E. Bordas, M.O. Ruault, O. Kaïtasov, S. Henry, O. Leseigneur, T. Bonnaillie, S. Pellegrino, S. Vaubaillon, D. Uriot, JANNUS: A multi-irradiation platform for experimental validation at the scale of the atomistic modelling, J. Nucl. Mater. 386–388 (2009) 967–970. doi:10.1016/j.jnucmat.2008.12.262.

[6] L. Beck, Y. Serruys, S. Miro, P. Trocellier, E. Bordas, F. Leprêtre, D. Brimbal, T. Loussouarn, H. Martin, S. Vaubaillon, S. Pellegrino, D. Bachiller-Perea, Ion irradiation and radiation effect characterization at the JANNUS-Saclay triple beam facility, J. Mater. Res. 30 (2015) 1183–1194. doi:10.1557/jmr.2014.414.

[7] J.F. Ziegler, M.D. Ziegler, J.P. Biersack, SRIM – The stopping and range of ions in matter (2010), Nucl. Instrum. Methods Phys. Res. Sect. B Beam Interact. Mater. At. 268 (2010) 1818–1823. doi:10.1016/j.nimb.2010.02.091.

[8] J.F. Ziegler, J.P. Biersack, U. Littmark, The Stopping and Range of Ions in Matter, Pergamon Press, 1985.

[9] R.E. Stoller, M.B. Toloczko, G.S. Was, A.G. Certain, S. Dwaraknath, F.A. Garner, On the use of SRIM for computing radiation damage exposure, Nucl. Instrum. Methods Phys. Res. Sect. B Beam Interact. Mater. At. 310 (2013) 75–80. doi:10.1016/j.nimb.2013.05.008.

[10] K. Nordlund, J. Wallenius, L. Malerba, Molecular dynamics simulations of threshold displacement energies in Fe, Nucl. Instrum. Methods Phys. Res. Sect. B Beam Interact. Mater. At. 246 (2006) 322–332. doi:10.1016/j.nimb.2006.01.003.

[11] R.E. Stoller, M.B. Toloczko, G.S. Was, A.G. Certain, S. Dwaraknath, F.A. Garner, On the use of SRIM for computing radiation damage exposure, Nucl. Instrum. Methods Phys. Res. Sect. B Beam Interact. Mater. At. 310 (2013) 75–80. doi:10.1016/j.nimb.2013.05.008.

[12] A. Wagner, W. Anwand, M. Butterling, T.E. Cowan, F. Fiedler, F. Fritz, M. Kempe, R. Krause-Rehberg, Positron-Annihilation Lifetime Spectroscopy using Electron Bremsstrahlung, J. Phys. Conf. Ser. 618 (2015) 012042. doi:10.1088/1742-6596/618/1/012042.

[13] P. Kirkegaard, J.V. Olsen, M.M. Eldrup, N.J. Pedersen, PALSfit: A computer program for analysing positron lifetime spectra, Risoe National Laboratory, Roskilde, 2009.

[14] P. Desgardin, L. Liszkay, M.F. Barthe, L. Henry, J. Briaud, M. Saillard, L. Lepolotec, C. Corbel, G. Blondiaux, A. Colder, P. Marie, M. Levalois, Slow positron beam facility in Orleans, in: W. Triftshauser, G. Kogel, P. Sperr (Eds.), Positron Annihil. - Icpa-12, Trans Tech Publications Ltd, Zurich-Uetikon, 2001: pp. 523–525.

[15] S. Mühlbauer, A. Heinemann, A. Wilhelm, L. Karge, A. Ostermann, I. Defendi, A. Schreyer, W. Petry, R. Gilles, The new small-angle neutron scattering instrument SANS-1 at MLZ—characterization and first results, Nucl. Instrum. Methods Phys. Res. Sect. Accel. Spectrometers Detect. Assoc. Equip. 832 (2016) 297–305. doi:10.1016/j.nima.2016.06.105.

[16] U. Keiderling, The new `BerSANS-PC' software for reduction and treatment of small angle neutron scattering data, Appl. Phys. Mater. Sci. Process. 74 (2002) 1455–1457. doi:10.1007/s003390201561.

[17] O. Glatter, Determination of particle-size distribution functions from small-angle scattering data by means of the indirect transformation method, J. Appl. Crystallogr. 13 (1980) 7–11. doi:10.1107/S0021889880011429.

[18] A. Wagner, Long-term irradiation effects on reactor pressure vessel steels, Martin-Luther-Universität Halle-Wittenberg, 2017.

[19] P.A. Beaven, F. Frisius, R. Kampmann, R. Wagner, Analysis of Defect Microstructures in Irradiated Ferritic Alloys, in: At. Transp. Defects Met. Neutron Scatt., Springer, Berlin, Heidelberg, 1986: pp. 228–233. doi:10.1007/978-3-642-71007-0_38.

[20] D.J. Larson, T.J. Prosa, R.M. Ulfig, B.P. Geiser, T.F. Kelly, Local Electrode Atom Probe Tomography, Springer New York, New York, NY, 2013. http://link.springer.com/10.1007/978-1-4614-8721-0 (accessed April 26, 2016).

[21] M.P. Moody, J.M. Cairney, B. Gault, S.P. Ringer, Atom Probe Microscopy, Springer Series in Materials Science, vol. 160, 2012. http://www.springer.com/materials/characterization+%26+evaluation/book/978-1-4614-3435-1 (accessed October 24, 2012).

[22] M. Miller, A. Cerezo, M. Hetherington, G. Smith, Atom Probe Field Ion Microscopy, Clarendon, Oxford, 1996.

[23] M. Miller, Atom Probe Tomography, Kluwer Academic / Plenium Publishers, New York., 2000.

[24] Lefebvre, W, Vurpillot, F, Sauvage, X, Atom Probe Tomography - Put Theory into practice, San Diego : Elsevier Science, 2016.

[25] G. Da Costa, F. Vurpillot, A. Bostel, M. Bouet, B. Deconihout, Design of a delay-line position-sensitive detector with improved performance, Rev. Sci. Instrum. 76 (2005) 013304–013304.

[26] E. Meslin, B. Radiguet, M. Loyer-Prost, Radiation-induced precipitation in a ferritic model alloy: An experimental and theoretical study, Acta Mater. 61 (2013) 6246–6254. doi:10.1016/j.actamat.2013.07.008.

[27] C. Pareige, V. Kuksenko, P. Pareige, Behaviour of P, Si, Ni impurities and Cr in self ion irradiated Fe–Cr alloys – Comparison to neutron irradiation, J. Nucl. Mater. 456 (2015) 471–476. doi:10.1016/j.jnucmat.2014.10.024.

[28] M. Thuvander, H.-O. Andr?n, K. Stiller, Q.-H. Hu, A statistical method to detect ordering and phase separation by APFIM, Ultramicroscopy. 73 (1998) 279–285. doi:10.1016/S0304-3991(97)00168-X.

[29] P. Auger, A. Menand, D. Blavette, STATISTICAL ANALYSIS OF ATOM-PROBE DATA (II) : THEORETICAL FREQUENCY DISTRIBUTIONS FOR PERIODIC FLUCTUATIONS AND SOME APPLICATIONS, J Phys C6. 49 (1988) 439.

[30] D. Blavette, G. Grancher, A. Bostel, J Phys C6. 49 (1988) 433.

[31] W.C. Oliver, G.M. Pharr, An improved technique for determining hardness and elastic modulus using load and displacement sensing indentation experiments, J. Mater. Res. 7 (1992) 1564–1583.

[32] Final report PERFECT project, (2008).

[33] A. Vehanen, P. Hautojärvi, J. Johansson, J. Yli-Kauppila, P. Moser, Vacancies and carbon impurities in alpha-iiron: Electron irradiation, Phys. Rev. B. 25 (1982) 762–780. doi:10.1103/PhysRevB.25.762.

[34] V. Slugeň, H. Hein, S. Sojak, J.S. Veterníková, M. Petriska, V. Sabelová, M. Pavúk, R. Hinca, M. Stacho, Evaluation of the reactor pressure vessel steels by positron annihilation, J. Nucl. Mater. 442 (2013) 499–506.

[35] E. Materna-Morris, M. Rieth, K. Ehrlich, Mechanical properties and microstructure of HFR-irradiated ferritic/martensitic low-activation alloys, in: Eff. Radiat. Mater. 19th Int. Symp. ASTM STP 1366 M Hamilt. Kumar T Rosinski M Grossbeck, Eds., ASTM, West Conshohocken, 1999.

[36] R. Coppola, R. Lindau, M. Magnani, R.P. May, A. Möslang, M. Valli, Polarised Small Angle Neutron Scattering study of microstructural radiation damage in steels for nuclear applications, Phys. B Condens. Matter. 385 (2006) 647–649. doi:10.1016/j.physb.2006.06.092.

[37] R. Coppola, R. Lindau, M. Magnani, R.P. May, A. Möslang, M. Valli, Microstructural investigation, using small-angle neutron scattering (SANS), of Optifer steel after low dose neutron irradiation and subsequent high temperature tempering, J. Nucl. Mater. 367 (2007) 377–381. doi:10.1016/j.jnucmat.2007.03.125.

[38] R. Coppola, R. Lindau, R.P. May, A. Möslang, M. Valli, Microstructural investigation of low-dose neutron irradiation effects in martensitic steels for nuclear application by means of small-angle neutron scattering, J. Appl. Crystallogr. 40 (2007) s142–s146. doi:10.1107/S0021889807005110.

[39] R. Coppola, M. Klimiankou, R. Lindau, R.P. May, M. Valli, SANS and TEM study of Y2O3 particle distributions in oxide-dispersion strengthened EUROFER martensitic steel for fusion reactors, Phys. B Condens. Matter. 350 (2004) E545–E548. doi:10.1016/j.physb.2004.03.148.

[40] M. Matijasevic, A. Almazouzi, Effect of Cr on the mechanical properties and microstructure of Fe-Cr model alloys after n-irradiation, J. Nucl. Mater. 377 (2008) 147–154. doi:10.1016/j.jnucmat.2008.02.061.

[41] F. Bergner, A. Ulbricht, C. Heintze, Estimation of the solubility limit of Cr in Fe at 300 °C from small-angle neutron scattering in neutron-irradiated Fe–Cr alloys, Scr. Mater. 61 (2009) 1060–1063. doi:10.1016/j.scriptamat.2009.08.028.

[42] F. Bergner, C. Pareige, V. Kuksenko, L. Malerba, P. Pareige, A. Ulbricht, A. Wagner, Critical assessment of Cr-rich precipitates in neutron-irradiated Fe-12at%Cr: comparison of SANS and APT, J. Nucl. Mater. 442 (2013) 463–469. doi:10.1016/j.jnucmat.2013.05.023.

[43] F. Bergner, C. Pareige, M. Hernández-Mayoral, L. Malerba, C. Heintze, Application of a three-feature dispersed-barrier hardening model to neutron-irradiated Fe–Cr model alloys, J. Nucl. Mater. 448 (2014) 96–102. doi:10.1016/j.jnucmat.2014.01.024.

[44] V. Kuksenko, C. Pareige, P. Pareige, Cr precipitation in neutron irradiated industrial purity Fe–Cr model alloys, J. Nucl. Mater. 432 (2013) 160–165. doi:10.1016/j.jnucmat.2012.07.021.

[45] V. Kuksenko, C. Pareige, C. Genevois, P. Pareige, Characterisation of Cr, Si and P distribution at dislocations and grain-boundaries in neutron irradiated Fe–Cr model alloys of low purity, J. Nucl. Mater. 434 (2013) 49–55. doi:10.1016/j.jnucmat.2012.11.027.

[46] V. Kuksenko, C. Pareige, C. Génevois, F. Cuvilly, M. Roussel, P. Pareige, Effect of neutron-irradiation on the microstructure of a Fe–12at.%Cr alloy, J Nucl Mater. 415 (2011) 61–66.

[47] O. Tissot, C. Pareige, E. Meslin, B. Decamps, J. Henry, Kinetics of α′ precipitation in an electron-irradiated Fe15Cr alloy, Scr. Mater. 122 (2016) 31–35. doi:10.1016/j.scriptamat.2016.05.021.

[48] I.M. Lifshitz, V.V. Slyozov, The kinetics of precipitation from supersaturated solid solutions, J. Phys. Chem. Solids. 19 (1961) 35–50. doi:10.1016/0022-3697(61)90054-3.

[49] C. Wagner, Theorie der Alterung von Niederschlägen durch Umlösen (Ostwald-Reifung), Z. Für Elektrochem. Berichte Bunsenges. Für Phys. Chem. 65 (1961) 581–591. doi:10.1002/bbpc.19610650704.

[50] W. Xiong, M. Selleby, Q. Chen, J. Odqvist, Y. Du, Phase Equilibria and Thermodynamic Properties in the Fe-Cr System, Crit. Rev. Solid State Mater. Sci. 35 (2010) 125–152. doi:10.1080/10408431003788472.

[51] G. Bonny, D. Terentyev, L. Malerba, On the α–α′ miscibility gap of Fe–Cr alloys, Scr. Mater. 59 (2008) 1193–1196. doi:10.1016/j.scriptamat.2008.08.008.

[52] V. Kuksenko, C. Pareige, P. Pareige, Cr precipitation in neutron irradiated industrial purity Fe–Cr model alloys, J. Nucl. Mater. 432 (2013) 160–165. doi:10.1016/j.jnucmat.2012.07.021.

[53] M. Bachhav, G. Robert Odette, E.A. Marquis, α′ precipitation in neutron-irradiated Fe–Cr alloys, Scr. Mater. 74 (2014) 48–51. doi:10.1016/j.scriptamat.2013.10.001.

[54] F. Soisson, T. Jourdan, Radiation-accelerated precipitation in Fe–Cr alloys, Acta Mater. 103 (2016) 870–881. doi:10.1016/j.actamat.2015.11.001.

[55] F. Vurpillot, A. Bostel, D. Blavette, Trajectory overlaps and local magnification in three-dimensional atom probe, Appl. Phys. Lett. 76 (2000) 3127–3129. doi:10.1063/1.126545.

[56] M.K. Miller, R.G. Forbes, Atom-Probe Tomography, Springer US, Boston, MA, 2014. http://link.springer.com/10.1007/978-1-4899-7430-3 (accessed December 8, 2015).

[57] S. Novy, P. Pareige, C. Pareige, Atomic scale analysis and phase separation understanding in a thermally aged Fe–20at.%Cr alloy, J. Nucl. Mater. 384 (2009) 96–102. doi:10.1016/j.jnucmat.2008.10.008.

[58] G.S. Was, S.M. Bruemmer, Effects of irradiation on intergranular stress corrosion cracking, J. Nucl. Mater. 216 (1994) 326–347. doi:10.1016/0022-3115(94)90019-1.

[59] G.S. Was, R.S. Averback, 1.07 - Radiation Damage Using Ion Beams, in: R.J.M. Konings (Ed.), Compr. Nucl. Mater., Elsevier, Oxford, 2012: pp. 195–221. http://www.sciencedirect.com/science/article/pii/B9780080560335000070 (accessed October 29, 2014).

[60] K. Dawi, C.-W. He, M.-F. Barthe, P. Desgardin, A. Volgin, Vacancy defects study in Fe based alloys induced by irradiation under various conditions, in: C. Hugenschmidt, C. Piochacz (Eds.), 13th Int. Workshop Slow Positron Beam Tech. Appl. Slopos13, Iop Publishing Ltd, Bristol, 2014: p. 012007.

[61] C.W. He, K. Dawi, C. Platteau, M.F. Barthe, P. Desgardin, S. Akhmadaliev, Vacancy type defect formation in irradiated alpha-iron investigated by positron beam Doppler broadening technique, in: C. Hugenschmidt, C. Piochacz (Eds.), 13th Int. Workshop Slow Positron Beam Tech. Appl. Slopos13, Iop Publishing Ltd, Bristol, 2014: p. UNSP 012018.

[62] A. Prokhodtseva, B. Décamps, A. Ramar, R. Schäublin, Impact of He and Cr on defect accumulation in ion-irradiated ultrahigh-purity Fe(Cr) alloys, Acta Mater. 61 (2013) 6958–6971. doi:10.1016/j.actamat.2013.08.007.

[63] M. Hernández-Mayoral, C. Heintze, E. Oñorbe, Transmission electron microscopy investigation of the microstructure of Fe–Cr alloys induced by neutron and ion irradiation at 300 °C, J. Nucl. Mater. 474 (2016) 88–98. doi:10.1016/j.jnucmat.2016.03.002.

[64] O. Tissot, C. Pareige, E. Meslin, B. Décamps, J. Henry, Influence of injected interstitials on α′ precipitation in Fe–Cr alloys under self-ion irradiation, Mater. Res. Lett. 5 (2017) 117–123. doi:10.1080/21663831.2016.1230896.

[65] L. Shao, C.-C. Wei, J. Gigax, A. Aitkaliyeva, D. Chen, B.H. Sencer, F.A. Garner, Effect of defect imbalance on void swelling distributions produced in pure iron irradiated with 3.5 MeV self-ions, J. Nucl. Mater. 453 (2014) 176–181. doi:10.1016/j.jnucmat.2014.06.002.

[66] E.H. Lee, L.K. Mansur, M.H. Yoo, Spatial variation in void volume during charged particle bombardment — the effects of injected interstitials, J. Nucl. Mater. 85 (1979) 577–581. doi:10.1016/0022-3115(79)90548-8.

[67] D.L. Plumton, W.G. Wolfer, Suppression of void nucleation by injected interstitials during heavy ion bombardment, J. Nucl. Mater. 120 (1984) 245–253. doi:10.1016/0022-3115(84)90062-X.

[68] A. Bhattacharya, E. Meslin, J. Henry, S. Poissonnet, B. Décamps, B., Acta Mater. (2016) submitted.

[69] L. Messina, Z. Chang, P. Olsson, Ab initio modelling of vacancy–solute dragging in dilute irradiated iron-based alloys, Nucl. Instrum. Methods Phys. Res. Sect. B Beam Interact. Mater. At. 303 (2013) 28–32. doi:10.1016/j.nimb.2013.01.049.

[70] L. Messina, L. Malerba, P. Olsson, Stability and mobility of small vacancy–solute complexes in Fe–MnNi and dilute Fe–X alloys: A kinetic Monte Carlo study, Nucl. Instrum. Methods Phys. Res. Sect. B Beam Interact. Mater. At. 352 (2015) 61–66. doi:10.1016/j.nimb.2014.12.032.

[71] L. Messina, M. Nastar, T. Garnier, C. Domain, P. Olsson, Exact ab initio transport coefficients in bcc Fe-X (X=Cr,Cu,Mn,Ni,P,Si) dilute alloys, Phys. Rev. B. 90 (2014) 104203. doi:10.1103/PhysRevB.90.104203.

[72] M. Chiapetto, L. Malerba, C.S. Becquart, Effect of Cr content on the nanostructural evolution of irradiated ferritic/martensitic alloys: an object kinetic Monte Carlo model, J. Nucl. Mater. 465 (2015) 326–336. doi:10.1016/j.jnucmat.2015.06.012.

[73] Deliverable 2.1.1